NTNU

Norwegian University of
Science and Technology

Behaviour and failure of aluminium extrusions under bending and stretching

Tobias Lund

Master of Science in Mechanical Engineering
Submission date: June 2018
Supervisor: David Morin, KT
Co-supervisor: Miguel Costas, KT
Magnus Langseth, KT

Norwegian University of Science and Technology
Department of Structural Engineering

Department of Structural Engineering
Faculty of Engineering
NTNU- Norwegian University of Science and Technology

ACCESSIBILITY

OPEN

MASTER THESIS 2018

SUBJECT AREA:	DATE:	NO. OF PAGES:
Computational Mechanics	22.06.2018	24 + 87+ 19

TITLE:

Behaviour and failure of AA6005A-T6 extrusions under bending and stretching

Oppførsel og brudd av AA6005A-T6 ekstruderinger under bøying og strekking

BY:

Tobias Lund

SUMMARY:
Current and future strategic challenges in the construction industry require safe and lightweight structures to achieve a good strength to weight ratio. Authentic material combinations together with numerical simulations are urgently needed to reduce development time and to remain competitive. Aluminium provides favourable strength to weight ratio, low density and high resistance to corrosion. In addition, it is recyclable and flexible as it can be processed in different ways, e.g. casting, extrusion and rolling. Aluminium extrusions supplied by Hydro Aluminium were used as an example to investigate failure behaviour. Fibrous- and recrystallised microstructure were investigated for an AA6005A-T6 alloy under combined bending and stretching loads and axial crushing simulations. The material model for the aluminium alloy were established using a damage regularisation scheme for shell elements. This model assesses the elements deformation mode based on the thinning strain rate of the through-thickness gradient. Input data for the finite element models and stretch bending and crash simulation were generated through quasi-static material tests. From the quasi-static uni-axial tensile tests, the materials strain data was accumulated using a digital image correlation analysis with the software eCorr. This data was processed, and the material characteristics were described using Hooke's law, Hershey-Hosford yield criterion, an associated flow, extended Voce law and Cockroft-Latham failure criterion. From these procedures material cards for both the alloy with fibrous- and the recrystallised microstructure were implemented for use in Abaqus/Explicit.
Experimental- and numerical results for the quasi-static stretch bending and axial crushing were separately discussed and compared. The validity of the numerical model and its ability to replicate the physical experiments were reviewed and how different features affected the results considered. Components yielded high reproducibility within each test setup and only minor deviations in the material behaviour and failure characteristics were observed. Consequently the constitutive model ability to replicate the test results were examined.
The combined bending and stretching loads, and axial loads for both test setups were reproduced in the simulation models with high accuracy. The models ability to replicate a more complex deformations with complex stress states and severe bending were decisive to conclude that the constitutive numerical models were able to predict failure accurately. A parameter sensitivity study was performed on the numerical models, evaluating mesh dependency, boundary conditions and fillet contribution.
In this Thesis it was proven that aluminium extrusions could be sufficiently simulated by means of finite element methods under bending and stretching loads as well as in axial crushing situations utilising the damage regularisation scheme. However, some discrepancies were found between the numerical- and experimental result, particularly for the fibrous material model. Further work should include an introduction of an anisotropic yield criterion as the material exhibited anistropic behaviour.

RESPONSIBLE TEACHER: David Morin

SUPERVISOR(S): David Morin, Miguel Costas and Magnus Langseth

CARRIED OUT AT: Norwegian University of Science and Technology (NTNU)

Institutt for konstruksjonsteknikk
Fakultet for ingeniørvitenskap
NTNU- Norges teknisk- naturvitenskapelige universitet

TILGJENGELIGHET

ÅPEN

MASTEROPPGAVE 2018

FAGOMRÅDE:	DATO:	ANTALL SIDER:
Beregningsmekanikk	22.06.2018	24 + 87 + 19

TITTEL:

Oppførsel og brudd av AA6005A-T6 ekstruderinger under bøying og strekking

Behaviour and failure of AA6005A-T6 extrusions under bending and stretching

UTFØRT AV:

Tobias Lund

SAMMENDRAG:
Nåværende og fremtidige strategiske utfordringer innen konstruksjonsindustri avhenger av robuste og enkle strukturer for å oppnå en god styrke til vekt ratio. Autentiske materialkombinasjoner og numeriske beregninger er nødvendig for å redusere produksjonstiden og for å være konkurransedyktig i dagens marked. Aluminium er et material som gir store fordeler med en høy styrke til vekt ratio, lav tetthet og høy motstandsdyktighet mot korrosjon. Samtidig er det resirkulerbart, og kan i tillegg bli prosessert ved støping, ekstrudering eller pressing. Blir aluminium riktig anvendt, er det et konkurransedyktig material sammenlignet med andre struktur-orienterte materialer.
Aluminiumekstrusjonene ble levert av Hydro Aluminium, og ble videre brukt til å undersøke bruddoppførsel. Både fibrøs og rekrystallisert mikrostruktur ble analysert for en AA6005A-T6 aluminiumslegering under en kombinasjon av strekk- og bøye-last, samt aksiell stuking. Plastisk teori for materialmodellen ble etablert ved hjelp av en skade-regulariseringsmodell for skallelementer. Denne modellen undersøkte elementenes deformeringsmodus ved hjelp av tykkelsesgradienten til tynningstøyningsraten. Materialmodellene som ble brukt i elementmetodesimuleringene var basert på kvasi-statiske strekkprøver. Modellen ble validert og reprodusert ved god korrelasjon i Abaqus/Explicit. Tøyningen til materialet ble så akkumulert ved hjelp av en DIC analyse i softwaret eCorr. Den innsamlede dataen ble prosessert, og materialets karakteristikk ble beskrevet ved hjelp av Hooks lov, Hershey-Hosfords flytespenningskriterie, forbedret Voce lov og Cockroft-Latham bruddkriterie. Materialkort for både legeringen med fibrøs- og rekrystallisert mikrostruktur ble implementert for senere bruk i Abaqus/Explicit.
Ekspremintelle- og numeriske resultater for kvasi-statiske strekk-bøying og aksiell stuking ble drøftet og sammenlignet separat. Den numeriske modellens gyldighet og evne til å gjenskape de fysiske eksperimentene ble undersøkt sammen med innflytelsen til de ulike parametere. Resultatene hadde liten spredning i de fysiske testene, og det ble kun observert minimale forskjeller i brudd og materialoppførsel. De eksperimentelle testene til både strekk-bøying og aksiell stuking ble reprodusert i en numerisk simulering med god nøyaktighet. Modellens evne til å reprodusere den komplekse deformasjonen med avansert spenningstilstand og store tøyninger forårsaket av aksiell stuking var viktig i valideringsprosessen. En parameterstudie ble utført, og energihistorien til den numeriske modellen ble analysert.
Denne masteroppgaven har validert at materialmodellen kan brukes til å simulere brudd i kombinert strekk-bøye kraft, og med den komplekse deformasjonen påført av aksiell stuking. Noen uoverensstemmelser og forbedringspotensialer ble oppdaget, og brudd til materialet med fibrøs mikrostruktur kan bli bedre gjenskapt. Videre arbeid burde inkludere anistoropt flytekritere, da materialtestene viste tegn til anisotrop oppførsel.

FAGLÆRER: David Morin

VEILEDER(E): David Morin, Miguel Costas og Magnus Langseth

UTFØRT VED: Norges Teknisk Naturvitenskapelige Universitet (NTNU)

NORGES TEKNISK-NATURVITENSKAPELIGE UNIVERSITET
INSTITUTT FOR KONSTRUKSJONSTEKNIKK

MASTER THESIS 2018

Tobias Lund

Behaviour and failure of aluminium extrusions under bending and stretching

Design of safe and lightweight structures often involves the use of aluminium alloys due to their good strength to weigth ratios. Modern applications of aluminium alloys in the automotive industry rely on numerical simulations in order to reduce the development time and thus the design cost. To enable trustworthy numerical analyses, robust constitutive models, applicable in the automotive industry, are required. The research centre CASA at NTNU has recently proposed a simplified approach to model the behaviour and failure of aluminium extrusions under crash relevant deformation modes. The main task of this thesis is to evaluate the capacity of the novel modelling approach to describe the behaviour and failure of an aluminium extrusion under combined bending and stretching loadings.

The thesis work will involve a typical aluminium extrusion supplied by Hydro Aluminium. The tension tests required for the calibration of the material model in the non-linear FE program ABAQUS are to be performed in the laboratory at NTNU. The stretch-bending rig available at the Department of Structural Engineering will be a central tool for the development and execution of the component tests.

Possible keywords for activities in this master thesis research work may include:

- Literature review: Aluminium alloys, material and failure models, structural testing
- Experimental work: Quasi-static material and component tests under different loading conditions
- Numerical work: Calibration of material and failure model. Modelling and simulation of experimental tests.
- Validation: Comparison of experimental and numerical results. Evaluation of the model.

The candidates may agree with the supervisors to pay particular attention to specific parts of the investigation, or include other aspects than those already mentioned.

The thesis is to be organized as a research report, recognising the guidelines provided by Department of Structural Engineering.

Supervisors at NTNU: David Morin, Miguel Costas and Magnus Langseth

The report is to be handed in not later than 22 June 2018.

NTNU, 15 January 2018

David Morin

Preface

This Thesis was conducted at the Structural Impact Laboratory (SIMLab) at the Norwegian University of Science and Technology (NTNU) in the spring of 2018, to achieve the degree of Master of Science in Mechanical Engineering. The duration of the Thesis were 21 weeks between January and June 2018.

Acknowledgements

During this Thesis, my supervisors have been Associate Professor David Morin, Professor Magnus Langseth and Postdoc. Miguel Costas at the Structural Impact Laboratory (SIMLab), Department of Structural Engineering, Norwegian University of Science and Technology (NTNU). I wish to sincerely thank them for encouraging advise, assist and input.

I would like to express my gratitude to Miguel Costas for all the valuable guidance and support through meetings and e-mails. Your knowledge, interest and enthusiasm have been highly inspirational. Thanks for the immediate response to questions and always keeping your office door open. I never hesitated to ask you if something came up, and I am very grateful for having you as my co-supervisor.

Research Engineer Björn Olsson at Hydro Aluminium are acknowledged for his contribution in regards of delivering the aluminium extrusions and for valuable input.

Last, but not least I would like to thank Senior Engineer Tore Wisth for his contribution to the design of the test rig and Senior Engineer Trond Auestad for his aid in carrying out the experiments.

Trondheim

June 22, 2018

Abstract

Current and future strategic challenges in the construction industry require safe and lightweight structures to achieve a good strength to weight ratio. Authentic material combinations together with numerical simulations are urgently needed to reduce development time and to remain competitive. Aluminium provides favourable strength to weight ratio, low density and high resistance to corrosion. In addition, it is recyclable and flexible as it can be processed in different ways, e.g. casting, extrusion and rolling. Properly applied, aluminium alloys are competitive to other structural materials such as steel.

Aluminium extrusions supplied by Hydro Aluminium were used as an example to investigate failure behaviour. Fibrous- and recrystallised microstructure were investigated for an AA6005A-T6 alloy under combined bending and stretching loads and axial crushing simulations. The material model for the aluminium alloy were established using a damage regularisation scheme for shell elements. This model assesses the elements deformation mode based on the thinning strain rate of the through-thickness gradient. Input data for the finite element models and stretch bending and crash simulation were generated through quasi-static material tests. For an initial validation of the material models, the quasi-static tests were simulated with very good correlation of the results. From the quasi-static uni-axial tensile tests, the materials strain data was accumulated using a digital image correlation analysis with the software eCorr. This data was processed, and the material characteristics were described using Hooke's law, Hershey-Hosford yield criterion, an associated flow, extended Voce law and Cockroft-Latham failure criterion. From these procedures material cards for both the alloy with fibrous- and the recrystallised microstructure were implemented for use in Abaqus/Explicit.

Experimental- and numerical results for the quasi-static stretch bending and axial crushing were separately discussed and compared. The validity of the numerical model and its ability to replicate the physical experiments were reviewed and how different features affected the results considered. Components yielded high reproducibility within each test setup and only minor deviations in the material behaviour and failure characteristics were observed. Consequently the constitutive model ability to replicate the test results were examined.

The combined bending and stretching loads, and axial loads for both test setups were reproduced in the simulation models with high accuracy. The models ability to replicate a more complex deformations with complex stress states and severe bending were decisive to conclude that the constitutive numerical models were able to predict

failure accurately. A parameter sensitivity study was performed on the numerical models, evaluating mesh dependency, boundary conditions and fillet contribution. The increased bearing capacity added by the fillets had small effect on the result, and only a minor variation were caused by use of symmetry planes. With a coarser mesh, the accuracy of the numerical model decreased.

In this Thesis it was proven that aluminium extrusions could be sufficiently simulated by means of finite element methods under bending and stretching loads as well as in axial crushing situations utilising the damage regularisation scheme. However, some discrepancies were found between the numerical- and experimental result, particularly for the fibrous material model. Further work should include an introduction of an anisotropic yield criterion as the material exhibited anisotropic behaviour.

Contents

Nomenclature

Abbreviations

ASTM	American Standards for Testing Materials
BCC	Body-Centred Cubic
CASA	Centre for Advanced Structural Analysis
CPU	Central Processing Unit
DIC	Digital Image Correlation
FCC	Face-Centred Cubic
FE	Finite Element
HD	High Definition
MPC	Multi-Point Constraint
NTNU	Norwegian University of Science and Technology
PTFE	Polytetrafluoreten
SIMLab	Structural Impact Laboratory

Variables

δ_{ij}	Kronecker delta
$\dot{R}$	Rate of work hardening
$\dot{\epsilon}^p_w$, $\dot{\epsilon}^p_t$	Strain rate regards to width and thickness
$\dot{\epsilon}^T_{33}$, $\dot{\epsilon}^B_{33}$	Thinning strain rate at the top and bottom integration point
$\dot{\gamma}$	Plastic parameter
$\dot{\lambda}$	Non-negative scalar
$\dot{\varepsilon}^p_{ij}$	plastic strain rate
ϵ^p_w, ϵ^p_t	Strain regards to width and thickness
ϵ^E, ϵ^p	Elastic and plastic strain
$\epsilon_1, \epsilon_2, \epsilon_3$	Strain direction
ϵ_e	Engineering strain
ϵ_l	True strain
γ_{M_2}	Safety factor
$\boldsymbol{\sigma'}$	Stress deviator
$\boldsymbol{\sigma}$, σ_{ij}	Stress tensor
$\mathfrak{D}$	Plastic dissipation
ν	Poissons ratio
Ω	Deformation indication factor
σ^*	Stress triaxiality
σ_H	Hydrostatic part of the stress tensor

σ_I, σ_{II}, σ_{III}	Principal stress components
σ_0	Yield stress
σ_{eq}	Equivalent von Mises stress
σ_e	Engineering stress
σ_{kk}	Diagonal of the stress matrix
σ_t	True stress
θ_i	Initial hardening moduli
A	Deformed cross section area
A_0	Initial cross section area
c	Cockroft-Latham fracture parameter variable
D	Damage variable
D_C	Critical damage factor
E	Young's modulus
E_A	Artificial strain energy
E_I	Internal energy
E_K	Kinetic energy
F	Applied force
f	Yield function
$F_{b,Rd}$	Bearing resistance
$F_{t,Rd}$	Tension resistance
$F_{v,Rd}$	Shear resistance
G	Shear modulus
g	Plastic potential function
h_R	Hardening modulus
I_σ	Principle invariant
K_{ii}	Transverse stiffness
L	Deformed gauge length
L_0	Initial gauge length
l_e, l_t	Element length and thickness
m	Yield surface shape
p	Equivlalent plastic strain
Q_i	Saturated stress
R	Isotropic hardening
R_α	R-value
s_1, s_2, s_3	Principal deviatoric stress direction
t	thickness
u_L	Measured displacement
W_C	Cockroft-Latham fracture parameter
W_C^b	Cockroft-Latham fracture parameter regards to bending

W_C^l	Cockroft-Latham fracture parameter regards to large elements
W_C^m	Cockroft-Latham fracture parameter regards to membrane loading
W_C^s	Cockroft-Latham fracture parameter regards to small elements
W_E	External work
L	Lode parameter
R	Radius

List of Figures

List of Tables

1 Introduction

Evaluating and describing the behaviour and failure of an aluminium extrusion under combined bending and stretching loads have been identified as an important step towards establishing numerical models for structural problems, Figure 1.1a. A simplified material model proposed by the research centre CASA at NTNU was utilised. This model considered ductile fracture phenomenons that were hard to replicate in numerical analysis using a damage regularisation model for shell elements. The models ability to replicate complex stress states in form of crash relevant deformation modes, was completed to obtain further insight on failure behaviour, Figure 1.1b. The knowledge and experience gained from the experiments and analysis conducted in this Thesis innovates the way fracture phenomenons in structural problems are described in numerical analysis.

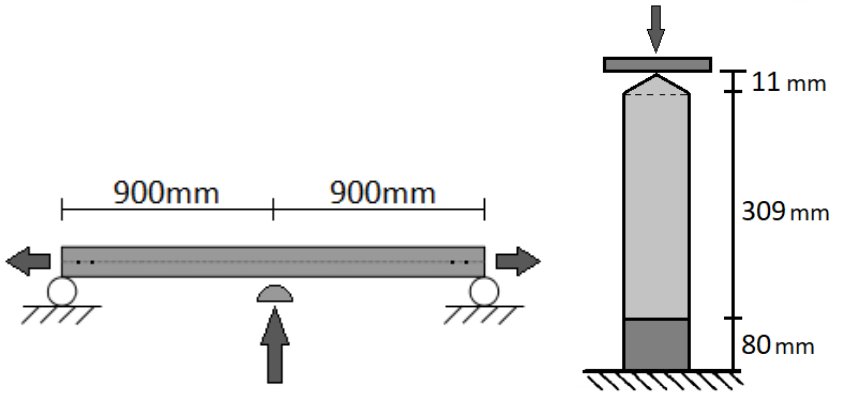

(a) Stretch bending test (b) Axial crushing test

Figure 1.1: Introductory experimental models

1.1 Background

Improving the strength and safety of structures are of great interest, and the ability to recreate and understand the structural behaviour and failure under different loads sets were crucial to achieve this. Design of safe and lightweight structures often involves the use of aluminium alloys due to their good strength to weight ratio. Industries have to rely on numerical simulations to reduce development time, and thus design cost to remain competitive. Durable constitutive models are required to enable trustworthy numerical analyses. For mid- to large scale structural problems, shell elements are the industry go to choice. Using shell elements, engineers can efficiently create representational models for problems were two dimensions are

greater than the third. The element type is versatile, which makes it suitable for a comprehensive range of structural applications in thin-walled structures.

Shell elements can safely be utilised in problems involving elastic-plastic loading and unloading. The issues arises when damage and failure needs to be precisely predicted. This is caused by two phenomenons. Firstly, element size is normally larger than the neck, implying that finite element (FE) solution are mesh dependent. Secondly, the development of the neck cannot be simulated with shell elements as long as strain localisation turns into a triaxiality driven problem. This creates a problem where the six stress- and strain tensors plays a considerable role, and plane stress condition is no longer applicable.

1.2 Objective

The main objective of this Thesis was to investigate and describe failure of aluminium extrusions supplied by Hydro Aluminium and compare behaviour of a fibrous- and recrystallised microstructure under combined bending and stretching loads. The objective has been met by a combination of numerical simulation in Abaqus/Explicit and laboratory tests using the stretch bending rig at SIMLab, NTNU. Axial crushing tests was conducted to validate the model with regards to complex stress states induced by a crash relevant deformations.

The objective has been completed by assessing the following technical subjects:

- Literature study related to aluminium alloys, material and failure models, and structural testing.
- Design of aluminium extrusion to capture fracture in the stretch-bending rig in the SIMLab laboratory. This included an assessment of the design of supports and loading conditions. The proposed design was based on numerical simulations and simplified analytical calculations.
- Executing quasi-static component tests with both the stretch-bending rig and the axial crushing machine.
- Comparison of the experimental and numerical model.
- Evaluation of the numerical model.
- Comparison of fibrous and recrystallised microstructure.

The Thesis has been limited by the following:

- The material studied was aluminium alloy AA6005A-T6 with both fibrous- and recrystallised microstructure.
- The extruded profiles were double-chambered with an outer wall thickness of 2.6 mm and a middle wall thickness of 1.7 mm.
- The extruded profile lengths were 1.8 m for the tests conducted in the stretch-bending rig, and 0.4 m for the axial crushing tests.
- The tests were conducted with quasi-static loading and under isothermal conditions.
- The numerical model was created with Hershey-Hosford yield criterion and Cockroft-Latham failure criterion.

1.3 Previous Work

A literature study was conducted to gain insight and to reveal different relevant points on the topic. The study included recrystallisation of aluminium alloys, stretch-bending behaviour, fracture criteria and numerical applicability in similar problems. This section summarises the most important discoveries.

Hansen and Bay (1980) studied the initial stages of recrystallisation in aluminium containing both small and large particles. In their study they found that recrystallisation nuclei formed preferably at the initial grain boundaries and deformation bands. This effect was enhanced by the intermetallic second phase impurity $FeAl_3$. However, $FeAl_3$ did not lead to significant grain refinement [8]. This behaviour was supported by Rayat K. Roy (2014) in his study on recrystallisation behaviour of commercial purity aluminium alloys. His study also showed that the effect of recrystallisation is influences by both heat, strain levels and the precipitates size, strength and spacing [9].

S. Li, O. Engler and P. Van Houtte (2005) investigated the plastic anisotropy and texture evolution subjected to tensile forces on two variants of an extruded AlZnMg alloy, one with a fibrous structure, and one with a recrystallised structure. Testing showed great differences in anisotropy and characteristics. Tensile tests taken at 0°, 45° and 90° relative to extrusion direction showed that the variation in anisotropy was mainly caused by texture evolution [10].

Literature on stretch bending of aluminium extrusions are limited, despite the industrial importance. This is most likely due to competition motivated secrecy from

main actors in the market. However, some studies can be found on the subject, although the relevancy of these studies were minimal as they do not focus on failure. Ueno and Ueda (1985) and Paulsen and Welo (1996) have published studies on stretch bending, where Ueno and Ueda studied the buckling behaviour in stretch bending of T-beams made of steel, while Paulsen and Welo were able to recreate stretch bending behaviour of aluminium extrusions using finite element analysis [11] [12].

More recently, Clausen, Hopperstad and Langseth (2000) studied the effect of geometry and alloy in stretch bending of aluminium extrusions. They performed 24 tests with a two meter long rectangular hollow anisotropic AA7108- and AA6082 extrusions on a specially designed stretch bending rig. The local deformation was primarily controlled by geometry and applied tensile force, while the alloy had a great influence on die force and springback. These findings were also recreated with a numerical model in LS-DYNA [13].

Additionally, Clausen, Hopperstad and Langseth (2001) tried to determine the effect of the tensile sequence in stretch bending of aluminium extrusions. A stretch bending rig was used to execute 29 tests on a two meter long aluminium extrusions. The same rectangular hollow cross-section and alloys were used when geometry effects were studied. From these tests, the sagging effect was very sensitive to the tensile sequence and a correlation between sagging development and strain resolution were discovered [14].

Several empirical relationships have proposed to obtain fracture strain as a function of element dimensions using shell elements to ensure that the material experiments are replicate in numerical simulations. Most of these empirical relationships come from marine engineering, were ship collisions into large metallic structures are of high importance. The common limitation of early proposed models were the regularization schemes. These regularization schemes only depended on membrane loading, which was the circumstance for both Germanischer Lloyd criterion [15] and Barba's law [16]. Also more recent studies, e.g., Körgesaar et al. (2014) who investigated the effect of element size for different stress states were limited to membrane loads. They averaged the values for stress and strains in a representative volume, which then was extrapolated to larger elements in combination with an instability criteria [17]. Andrade et al. (2016) proposed a regularization of the fracture criterion derived on the element size and stress state. The damage variable was however dependent on the incremental plastic strain, which accounted for non-linear strain paths. Andrade et al. study was also limited to membrane loads [18].

In reality, materials experience a much higher ductility when subjected to bending

than membrane loads. This is caused by strain localisation triggered by the bending loads and only a few studies have addressed this issue. Stroughton and Yoon (2011) proposed a method which combined a necking criterion, a fracture predictor and a shear criterion. This model relied on the through-thickness stress distribution in the elements and by identifying the failure mode [19]. Similarly, Pack and Mohr (2017) introduced a "domain of shell-to-solid equivalence" concept. The domain was based on Marciniak-Kuczynski analysis, and the delay of fracture caused by bending loads was accounted for with a through-thickness evaluation of a implemented necking criterion [20].

2 Material Mechanics

The use of shell-elements for mid- to large structural problems by investigating failure of an aluminium extrusion and comparing behaviour of a fibrous- and recrystallised microstructure has been challenged in this Thesis. Relevant material theory has been introduced and described to attain a fundamental understanding. An introduction to aluminium, including various attributes and use, together with the characteristics and material behaviour of aluminium alloy AA6005A-T6, has been assessed. Material characteristics for use in numerical models, relevant fracture phenomenons and how to reproduce this numerical has been discussed.

2.1 Aluminium

In design of safe and lightweight structures aluminium is often used due to the good strength to weight ratio. It is a soft material when compared to other materials with similar attributes, such as steel. The density of aluminium is approximately 2.7 kg/m^3, which is significantly lower than steel at 7.8 kg/m^3. The difference in density makes aluminium lighter, but it still maintains great strength characteristics. An other remarkable feature aluminium possesses which is desired in several industries, is resistance to corrosion. Aluminium resists corrosion through passivation, as a thin outside layer of aluminium oxide forms when the metal is exposed to oxygen in the air, preventing further corrosion.

Unfortunately, production of aluminium is very energy consuming and therefore costly. This is the main reason for the late introduction as a regular industrial metal. When producing aluminium, approximately 35 % of the costs are correlated to electric power, which means that a slight increase in energy price greatly affects the the total cost. However, aluminium has the favourable quality that it is nearly 100 % recyclable, and can be recycled repeatably. The recycling needs only 5 % of the energy compared to making new aluminium from bauxite. The recycling does not alter the material properties as the atomic structure is not being altered during melting.

Aluminium products can be processed in different ways, such as casting, extrusion and rolling. Casting can produce complex shapes, and is often used when producing a larger series of components. Extrusion utilises the properties of aluminium optimally, and allows for many different shapes and profiles. In this Thesis a double-chambered aluminium extrusion was inspected under bending and stretching. Aluminium can be rolled into sheets, plates and foils. This is done by rolling thick aluminium sections between rolls, reducing the thickness. Aluminium has

great weldability, and the two most common methods are metal inert gas welding and friction stir welding.

Aluminium is a polycrystalline material. The individual grain has a random crystallographic orientation which differ from the neighbouring grains. The region between the two grains are called grain boundary. Aluminium has a face-centred cubic (FCC) crystal lattice, Figure 2.1, and it is this crystal lattice that keeps aluminium ductile at very low temperatures, but it is also the cause of the low melting temperature at 930 K. Alloying elements are added to alter the characteristics of aluminium. Principal alloying elements include copper (Cu), magnesium (Mg), silicon (Si), manganese (Mn) and zinc (Zn).

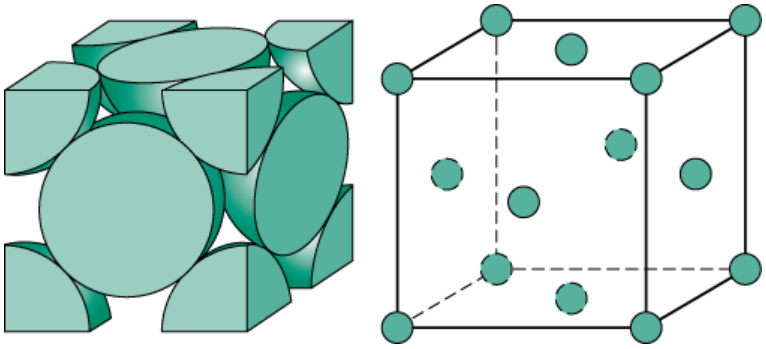

Figure 2.1: FCC crystal lattice [1]

2.1.1 AA6005A-T6

The aluminium alloy AA6005A-T6 has been utilised and evaluated in this Thesis, as this version of the alloy has an intermediate strength when compared to other aluminium alloys. AA6005A-T6 is an alloy in the 6xxx series, which are found widely in welding fabrication industry. It is extensively used as extrusions and often integrated in structural components. Both the threshold and the deformation energy was altered in the creation of the extrusion to obtain different grain sizes, enabling the possibility to study the effect of a fibrous- and recrystallised microstructure. The recrystallisation has been discussed in more detail in section 3.2.2. Some common applications for the 6xxx alloy are automotive frame sections, stiffeners and bracers on trucks and boats, handrails and drive shafts.

The main alloying elements for 6xxx alloys are magnesium and silicon, these alloying elements are added to obtain better strength characteristics. This combination, called magnesium silicide (Mg_2Si) gives the alloy its ability to be heat treated which increases the strength and hardness, as well as it gives better resistance to corrosion and better weldability [7]. In AA6005A-T6, additional alloying elements are added. Iron (Fe) is added to increase strength, while chromium (Cr) is added to control

the grain structure and prevent recrystallising during heat treatment. Manganese (Mn) increases strength through solution strengthening. It also retains strength at elevated temperatures. Zink (Zn) in addition to magnesium (Mg) and copper (Cu) generates heat-treatable aluminium alloys of very high strength. Titanium (Ti) is added as a grain refiner, in conjunction with better weldability [21]. These particles acts as an effective barrier to dislocation movement, increasing the yield strength of the material.

The thermal history of the aluminium is very important for the material strength. The T6 in AA6005A-T6 informs that the alloy has been heat treated and artificially aged, where T6 is the peak hardness condition. This condition is achieved by a combination of solution heat treating, quenching and artificially ageing. During solution heat treatment, temperature is kept at a level where the one-phase condition is reached in the equilibrium diagram. This condition is reached between 500°C and 550°C, which is between the melting temperature and the eutectic point. At this elevated temperature, the Mg_2Si precipitates are dissolved and a homogeneous solid state is reached. In this state the maximum of hardening solutes are reached in the solid solution of the aluminium matrix. The alloy is then cooled rapidly by press quenching, and thus preserving the solid solution [22]. The full chemical composition of AA6005A-T6 can be seen in Table 2.1.

Table 2.1: Detailed chemical composition of AA6005A-T6 [7]

	Si	*Mg*	*Mn*	*Cr*	*Zn*	*Ti*	*Fe*	*Cu*	*Mn + Cr*
Min.	0.50	0.40	-	-	-	-	-	-	0.12
Max.	0.90	0.70	0.50	0.30	0.20	0.10	0.35	0.30	0.50

2.2 Tensile Test

A tensile tests can be conducted to get the stress-strain relationship and the material characteristics such as the yield strength and ultimate strength. The tensile test should be performed following American Standards for Testing Materials (ASTM), with quasi-static conditions to avoid dynamic effects. The output from the testing machine are the force-displacement curve. The specimen is pulled until fracture and the engineering stress is determined from equation 2.1

$$\sigma_e = \frac{F}{A_0} \tag{2.1}$$

where σ_e is the engineering stress, F is the applied force and A_0 describes the initial cross section area of the specimen. Further, the engineering strain is calculated

using time-dependant measured displacement, $u_L(t)$, and the initial gauge length, l_0. The engineering strain, ϵ_e, is given by equation 2.2 and the engineering strain increment, $d\epsilon_e$, is given by equation 2.3.

$$\epsilon_e(t) = \frac{u_L(t)}{L_0} \tag{2.2}$$

$$d\epsilon_e(t) = \frac{du_L(t)}{L_0} \tag{2.3}$$

The straining is depending on the initial configuration. When allowing for large deformations, the geometrical changes of the specimen must be accounted for to describe the behaviour of the material. Setting $L = L_0 + u_L$ and $dL = du_L$, the strain increment can be defined with respect to the current gauge region length. This strain is called the true strain, ϵ_l, and the relationship with engineering strain can be obtained from equation 2.4 and equation 2.5.

$$d\epsilon_l(t) = \frac{du_L(t)}{L} \tag{2.4}$$

$$\epsilon_l(t) = \int_0^{u_L} \frac{du_L}{L} = \int_{L_0}^{L} \frac{dL}{L} = ln\Big(\frac{L}{L_0}\Big) = ln(1+\epsilon_e) \tag{2.5}$$

True stress is found by utilising the changing cross-section of the specimen, seen in equation 2.6, where σ_t is the true stress, F is applied force and A is the cross section of the specimen.

$$\sigma_t = \frac{F}{A} \tag{2.6}$$

For AA6005A-T6, the elastic strains remains small, and the plastic deformation is volume preserving due to the plastic strains that occur by plastic slipping. Assuming a constant volume, $A_0L_0 = AL$, the relationship between true stress and engineering stress can be derived by equation 2.7 and equation 2.8.

$$A = A_0 e^{(-\epsilon_l)} \tag{2.7}$$

$$\sigma_t = \frac{F}{A} = \frac{F}{A_0}\frac{A_0}{A} = \sigma_e e^{(\epsilon_l)} = \sigma_e(1+\epsilon_e) \tag{2.8}$$

In Abaqus, and other finite element codes, the stress-strain data is given in terms of true stress and true strain [1]. This is due to true stress being a direct measure of the traction carried out per unit area by an internal surface. This makes it the only stress output interesting from an engineering viewpoint [23].

The strain can be separated into two terms, elastic, ϵ^e, and plastic, ϵ^p. The elastic behaviour of the material is assumed to be described by Hooke's law, which states that stress and strain are linearly correlated and can be seen in equation 2.9, where E is Young's modulus. The plastic behaviour take effect after the yield stress. This is established by the stress for which the material experiences 0.2% plastic strain.

$$\epsilon^E = \frac{\sigma}{E} \tag{2.9}$$

Assuming isothermal conditions the total strain can be calculated using equation 2.10. From this relation, the true plastic strain curve can be calculated using equation 2.11, and it is easily seen that the true plastic strain varies with the true strain.

$$\epsilon = \frac{\sigma}{E} + \epsilon^p \tag{2.10}$$

$$\epsilon^p = \epsilon_l - \frac{\sigma}{E} \tag{2.11}$$

Prior to necking, the equivalent von Mises stress corresponds to true stress, $\sigma_{eq} = \sigma_t$, and the equivalent plastic strain corresponds to true plastic strain, $p = \epsilon^p$.

2.2.1 Necking

In the stress-strain derivations in section 2.2, it has been assumed that the deformation is uniform over the specimens length. This is not the case after necking. When the force reaches the maximum value, the deformation localises and the specimen experiences necking. The cross-section area where the localisation occurs decreases rapidly with increasing strain, and this plastic instability is called diffuse necking. After defuse necking the straining in the specimen is no longer uniform and other equations are needed to describe the behaviour of the material. Using equation 2.5 and equation 2.8, the engineering stress can be expressed as equation 2.12. Applying the product rule, the incremental change of the engineering stress can be defined by equation 2.13.

$$\sigma_e = \sigma_t e^{(-\epsilon_l)} \tag{2.12}$$

$$d\sigma_e = d\sigma_t e^{(-\epsilon_l)} - \sigma_t e^{(-\epsilon_l)} d\epsilon_l = (d\sigma_t - \sigma_t d\epsilon_l) e^{(-\epsilon_l)} \tag{2.13}$$

A typical stress-strain curve, with yield point, diffuse necking and fracture can be seen in Figure 2.2.

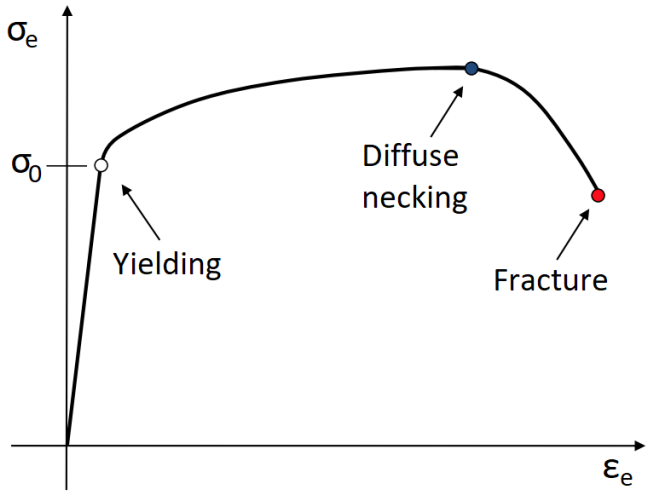

Figure 2.2: Engineering stress-strain curve showing yielding, diffuse necking and fracture [1]

The maximum value of the engineering stress is reached when $d\sigma_e = 0$, thus the diffuse necking occurs when equation 2.14 is satisfied. This criterion is known as the Considère criterion [1], graphically shown in Figure 2.3, where the diffuse necking occurs when the slope of the true stress - true strain curve equals the true stress. Hence, under normal conditions, the point of diffuse necking marks the end of where the data from a tensile test is applicable. The derivations in this section are only valid if the deformation is uniform.

$$\frac{d\sigma_t}{d\epsilon_l} = \sigma_t \tag{2.14}$$

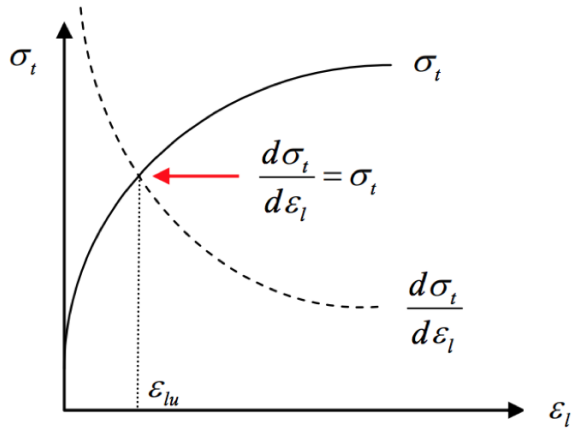

Figure 2.3: Graphic illustration of the necking criterion [1]

2.2.2 R-value

The behaviour of extruded AA6xxx alloys have been studied at a wide range of strain rates [24]. The plastic anisotropy of the alloy can be described by the R-value, also known as the Lankford coefficient, which can be determined by tensile test in three different directions relative to the extrusion direction, equation 2.15. $\dot{\varepsilon}_w^p$ and $\dot{\varepsilon}_t^p$ are the plastic strain rates in the width and thickness direction of the tensile test specimen.

$$R_\alpha = \frac{\dot{\varepsilon}_w^p}{\dot{\varepsilon}_t^p} \tag{2.15}$$

The material is said to experience isotropic flow properties if $R_\alpha = 1$ in all directions. Studies have shown that the ratio of strain versus the strain rate [25] are unity, and therefore the R-value can be defined as

$$R_\alpha = \frac{\varepsilon_w^p}{\varepsilon_t^p} \tag{2.16}$$

2.3 Fracture

This section describes the microscopic fracture mechanisms as well as the criterion used to predict this fracture. It is assumed that the yielding is independent of hydrostatic pressure. During fracture, void nucleation and growth results in an increasing volume and when studying the materials toughness, it is important to understand the microstructional events which can lead to fracture [3]. The behaviour of fracture can be approached using solid mechanics theory, modelling the material as a continuous mass. In other cases, it is necessary to use a microscopic fracture mechanism, modelling the behaviour as discrete particles.

Further, the three most common micromechanismsm of fracture in metal and alloys are discussed, Figure 2.4. Ductile fracture is generally a result of microvoid nucleation, growth and coalescence which then initiate inclusions and second-phase particles, Figure 2.4a. These microvoids are to some degree present in the material as a result from the manufacturing process. Cleavage fracture is the phenomenon where the fracture intersect individual crysallographic planes, creating a smooth fracture across the grains, Figure 2.4b. This is also called brittle fracture. Intergranular fracture is when the fracture path develops within the grain boundaries, Figure 2.4c [2].

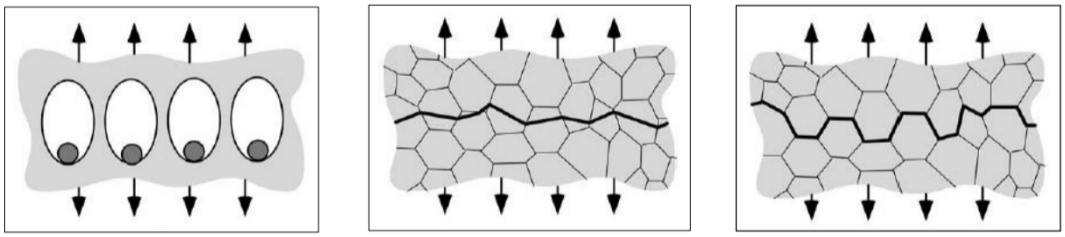

(a) Ductile fracture (b) Cleavage fracture (c) Intergranular fracture

Figure 2.4: The three most common micromechanisms of fracture in metals [2]

2.3.1 Ductile Fracture

The AA6005A-T6 alloy is presumed to experience ductile fracture, Figure 2.5. Under an increasing tensile force, the material will reach an instability point, and as described in section 2.2, this is due to the strain hardening not being able to keep pace with the loss of cross-sectional area, thus creating a neck. A main contributor to ductile fracture are impurities, and more impurities result in failure at lower strains.

This procedure starts with a ductile matrix which consists of inclusions, or impurities, Figure 2.5a. Interfacial bonds between the impurity and the matrix is broken and a void around the impurity is nucleated when adequate stress is applied, Figure 2.5b. With further applied strain or hydrostatic stress, the voids will grow independently, Figure 2.5c. Figure 2.5d and Figure 2.5e illustrates how the strain localise along a region of voids, creating local necking instabilities between the voids. Lastly the ductile matrix fails, and a fracture path is created.

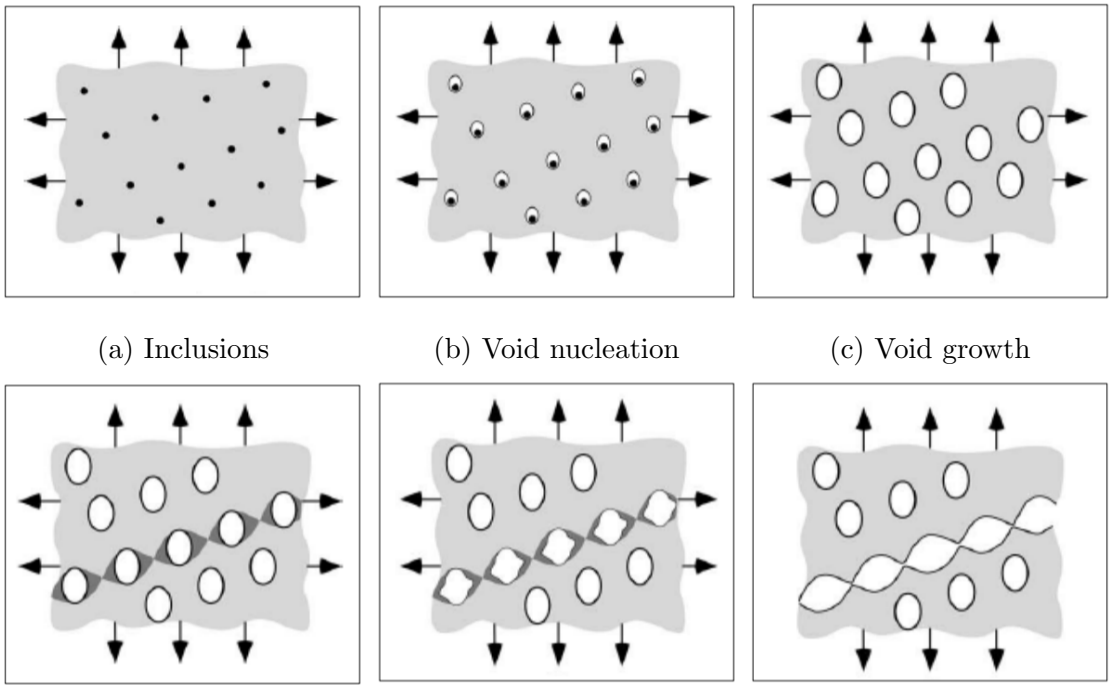

(a) Inclusions (b) Void nucleation (c) Void growth

(d) Strain localisation (e) Necking (f) Void coalescence

Figure 2.5: Void nucleation, growth and failure in a ductile matrix [2]

The precipitation hardened alloy used in this Thesis may have a bimodal distribution of the added elements. If this is the case large intermetallic particles could be formed and a thin dispersion of submicron second-phase precipitates. The bimodal distribution could lead to shear fracture surfaces [2].

An other typical fracture is the "cup and cone" fracture formation. This formation is often observed in uniaxial tests of circular specimens. The fracture is illustrated in Figure 2.6, where Figure 2.6a shows how the void nucleation and growth is created in the particles in the middle of the specimen. This leads to a crack with corresponding deformation bands at 45° offset to the direction of the applied tensile force, Figure 2.6b. The deformation bands has a higher concentration of strain, leading to nucleation of voids in finer precipitates. These precipitates are spaced more closely, Figure 2.6c. Lastly the specimen fails. This creates the recognisable "cup and cone" structure, Figure 2.6d. The central region of the fracture has a fibrous texture, while the region from the deformation bands, called shear surface due to its direction, is smooth.

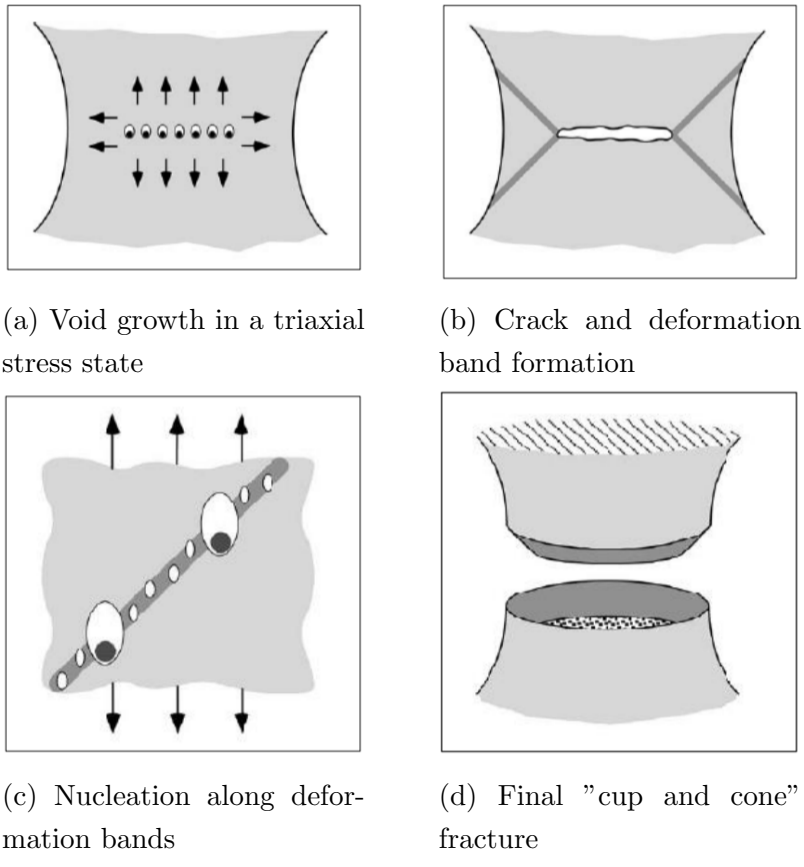

(a) Void growth in a triaxial stress state

(b) Crack and deformation band formation

(c) Nucleation along deformation bands

(d) Final "cup and cone" fracture

Figure 2.6: Development of "cup and cone" fracture surface in uniaxial tension [2]

The alloy can also experience shear fracture, called void-sheeting. If different sizes of particles are present, voids may nucleate in slip bands. Further shear then leads to void growth and finally shear fracture. This type of fracture is less pressure dependent due to the smaller extent of void growth needed before failure. This mechanism is illustrated in Figure 2.7.

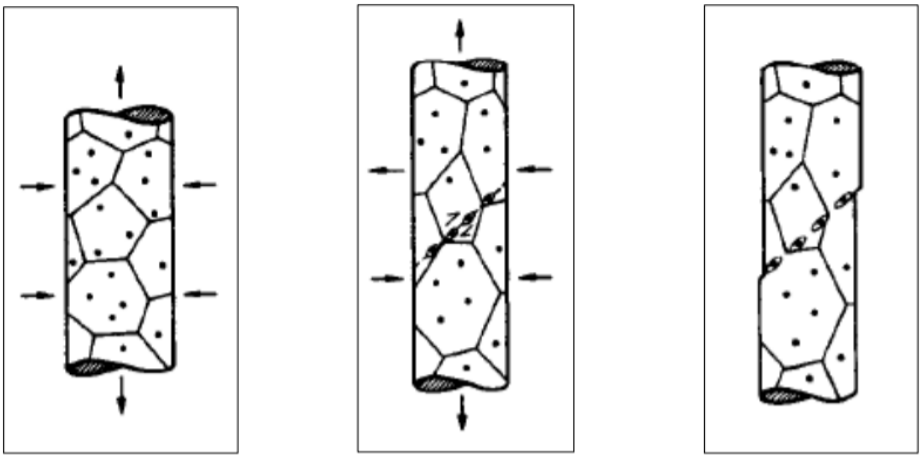

(a) Yielding (b) Void nucleation (c) Shear fracture

Figure 2.7: Shear fracture mechanism [3]

2.3.2 Failure Criterion

In this Thesis the uncoupled ductile Cockcroft-Latham failure criterion was adopted to describe the material behaviour during failure. This criterion is defined as

$$D = \frac{1}{W_C} \int_0^p max(\sigma_I, 0) dp \in [0, 1] \tag{2.17}$$

where D is the damage variable, W_C is the Cockcroft-Latham fracture parameter, σ_I is the first principal stress where $\langle \sigma_I \rangle = max\{\sigma_I, 0\}$, and p is the equivalent plastic strain. The main advantage of using an uncoupled failure criterion where the damage evolves as a function of the stress state and equivalent plastic strain, but has no coupling to the plastic behaviour is the identification of the damage parameters. In the Cockroft - Latham criterion failure occurs when an integration point reaches a value of unity. This take place when the integral of the first principal stress over the equvialent plastic strain equals the Cockcroft-Latham fracture parameter, W_C. σ_I can be expressed in terms of invariants, giving

$$D = \frac{1}{W_C} \int_0^p max\Big(\sigma^* + \frac{3 - L}{3\sqrt{3 + L^2}}, 0\Big) \sigma_{eq} dp \in [0, 1] \tag{2.18}$$

making it clear that the Cockcroft-Latham failure criterion is dependant on both stress triaxiality, σ^*, and the Lode parameter, L. From this expression it is obvious that the damage variable develop faster at high levels of stress triaxiality, thus lowering the failure strain. The Lode paramater develops the damage variable faster for general tension ($L = -1$), than general compression ($L = +1$) [26].

2.3.3 Damage Regularisation Model

The Cockckroft-Latham fracture parameter is defined as a weighed sum of two different parameters, W_C^b and W_C^m, which corresponds to the materials ductility during pure bending and pure membrane loading, respectively. Pure membrane loading produces strain localisation, and elements under this loading condition will have a lower W_C than elements under bending load. The weighted sum of the Cockcroft-Latham can be seen in equation 2.19.

$$W_C = \Omega W_C^b + (1 - \Omega) W_C^m \tag{2.19}$$

The deformation indication factor Ω is introduced to determine the amount of bending and membrane loading an element is subjected too. From equation 2.19 Ω takes a value of 1 under pure bending loading and 0 under pure membrane loading. The deformation indication factor is defined in terms of each elements through-thickness thinning strain rate, equation 2.20,

$$\Omega = \frac{1}{2} \frac{|\dot{\varepsilon}_{33}^T - \dot{\varepsilon}_{33}^B|}{|max\{\dot{\varepsilon}_{33}^T, \dot{\varepsilon}_{33}^B\}|} \tag{2.20}$$

where $\dot{\varepsilon}_{33}^T$ is the thinning strain rate at the top integration point of the element and $\dot{\varepsilon}_{33}^B$ is the thinning strain rate at the bottom integration point. Thinning is purely driven by membrane loads, which is in agreement with the definition of the deformation indication factor Ω. It should be mentioned that the measure of element bending-to-membrane loading is independent of the Cockcroft-Latham criterion, thus the determination of the damage variables gives no loss in generalisation.

W_C^b is assumed to be constant and essential to the material, while the materials ductility under pure membrane loading, W_C^m is a mesh-dependant problem. Larger elements develops lower strains, and will have a lower W_C than smaller elements. This problem was solved by adopting the exponential expression, equation 2.21. This expression defines W_C^m as a function of the element length-to-thickness ratio, $\frac{l_e}{t_e}$.

$$W_C^m = W_C^l + \left(W_C^s - W_C^l\right) e^{\left(-c\left(\frac{l_e}{t_e}-1\right)\right)} \tag{2.21}$$

The parameters W_C^l, W_C^s and c are obtained using a combination of tensile tests, digital image correlation (DIC) and numerical modelling.

3 Material Modelling

3.1 Literature review

This chapter introduces the theory of plasticity and the theory behind the material model used. AA6005A-T6, as other aluminium alloys, will behave linearly elastic at small strains. These strain deformations are reversible, and the relationship between stress and strain is linear and defined by Hooke's Law, equation 2.9. At a larger stress level, the material behaviour becomes nonlinear and irreversible plastic deformations occurs. The transition from elastic domain to elastic-plastic domain can be both gradual or abrupt, but most 6xxx aluminium alloys show a gradual transition [1]. The theory of plasticity include yield criterion, flow rule and the work-hardening rule. It is assumed that the process is quasi-static and the conditions are isothermal.

3.1.1 Yield Criterion

The yield limit can be described by the yield criterion, which is presented in equation 3.1

$$f(\boldsymbol{\sigma}) = 0 \tag{3.1}$$

where f is a continuous yield function of the stress tensor $\boldsymbol{\sigma}$. The yield criterion defines a surface in the stress space, called yield surface. The stress tensor $\boldsymbol{\sigma}$ takes in negative values in the elastic domain, and accordingly the elastic domain is defined by the inequality

$$f(\boldsymbol{\sigma}) < 0. \tag{3.2}$$

In this domain the material experiences only elastic deformations, Figure 3.1. At the plastic domain, which is the yield surface enclosed by the elastic domain, plastic deformations can take place. The yield function is assumed to not have any values outside the yield surface, thus every value $f(\boldsymbol{\sigma}) > 0$ is inadmissible [1].

A hypo-elastic plastic constitutive model was adopted to represent the materials behaviour. The yield function can be written on the form

$$f(\boldsymbol{\sigma}) = \sigma_{eq} - (\sigma_0 + R) \leqslant 0. \tag{3.3}$$

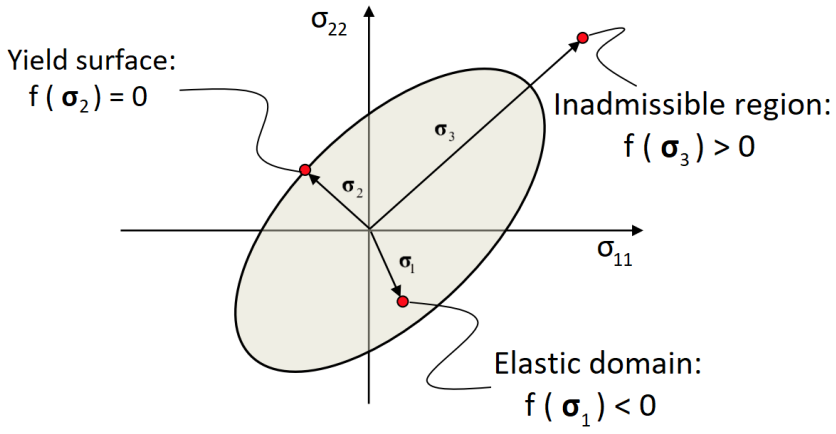

Figure 3.1: Elastic domain, yield surface and inadmissible region [1]

where $\sigma_{eq} = \varphi(\sigma)$ is the equivalent stress, which measures the magnitude of the stress-state the material is subjected to, and σ_0 is the initial yield stress, which is determined by tensile tests. R is the isotropic hardening of the material [1].

For most metals and alloys, the yield criterion is assumed to only depend on the deviatoric stress state due to pressure insensitivity. Plastic deformations mostly occur from plastic slipping, which is a shear driven deformation mode. Yielding starts in slip systems when the shear stress reaches a critical value on a certain slip plane in the slip direction, called Schmid's Law. The slip planes are the planes with the highest planar density, while the slip direction is the direction with the highest linear density. The major slip system in aluminium and other materials with a FFC crystal structure are slip plane $\{111\}$ and slip direction $\langle 110 \rangle$, Figure 3.2. This gives a total number of 12 slip systems. The number of slip systems are directly related to the materials ductility.

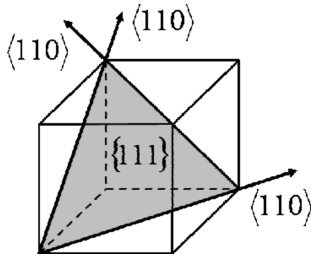

Figure 3.2: Predominant family of slip systems for FCC crystals [1]

As a simplification, the material was assumed to behave in compliance with the theory of plastic incompressibility, meaning that the overall volume of the material remains the same after plastic deformation. In reality there is a small change in

volume, e.g. dislocations moving to the edge of the material matrix, but this contribution was neglected. This gives equation 3.4, were the plastic incompressibility is described in terms of true strain.

$$\varepsilon_1 + \varepsilon_2 + \varepsilon_3 = 0 \tag{3.4}$$

The yielding is independent of the axial tension stress and other stresses that works normal to the lattice plane, hence the plastic deformations is initiated by shear stress component in the slip system, not applied axial stress [27]. Due to the pressure insensitivity, the yield criterion was expressed on the form

$$f(\boldsymbol{\sigma'}) = 0. \tag{3.5}$$

where $\boldsymbol{\sigma'}$ is the stress deviator. The stress deviator, $\boldsymbol{\sigma'}$, is defined by $\sigma'_{ij} = \sigma_{ij} - \sigma_H \delta_{ij}$, where σ_H is the hydrostatic stress, i.e the isotropic stress or mean normal stress and δ_{ij} is the Kronecker delta. The hydrostatic stress equation is given in equation 3.6, where σ_{kk} represent the diagonal of the stress matrix, σ_{11}, σ_{22} and σ_{33} and I_σ is the principal invariant. The hydrostatic stress is equal in magnitude to the pressure, but works in the opposite direction.

$$\sigma_H = \frac{1}{3}\sigma_{kk} = \frac{1}{3}I_\sigma \tag{3.6}$$

Equation 3.6 is useful due to the fact that isotropic stress controls volumetric change in the elastic region while the deviatoric stress controls the distortion. The hydrostatic stress can never cause plastic flow due to all the active planes are principal planes and no shear stresses arises. The deviatoric stresses however, produces shear stress and can therefore create plastic flow if the plastic domain is reached.

The material was assumed to be isotropic, but this is not the case for extruded aluminium profiles. However, a simplified yield criterion could be applied if the degree of anisotropy was low. An isotropic yield criterion implies that the yield function is independent of the direction of the loading within the material. This infer that the grain in the polycrystalline material have arbitrary orientation in space. The yield function is most conveniently written in terms of pressure invariants of the stress deviator, equation 3.7,

$$f(J_2, J_3) = 0 \tag{3.7}$$

where $J_2 = \frac{1}{2}\sigma'_{ij}\sigma'_{ij}$ and $J_3 = \det(\sigma'_{ij})$ [1].

3.1.2 Plastic Flow Rule

The plastic flow rule is generally defined as

$$\dot{\varepsilon}_{ij}^{p} = \dot{\lambda}\frac{\partial g}{\partial \sigma_{ij}} \tag{3.8}$$

where $\dot{\varepsilon}_{ij}^{p}$ is the plastic strain rate, $\dot{\lambda}$ is a non-negative scalar, $g = g(\boldsymbol{\sigma}) \geqslant 0$ is the plastic potential function assumed to be a positive homogeneous function and σ_{ij} is the true stress. This definition ensures that the plastic strain rate gives non-negative dissipation, where plastic dissipation is given by $\mathfrak{D} = \sigma_{ij}\dot{\varepsilon}_{ij}^{p} \geqslant 0$.

The plastic potential function could be defined by the yield function f, equation 3.9.

$$\dot{\varepsilon}_{ij}^{p} = \dot{\lambda}\frac{\partial f}{\partial \sigma_{ij}} \tag{3.9}$$

This is called associated flow rule, since the plastic potential is associated with the yield function. This rule implies that the plastic strain increment vector is parallel to the gradient of the yield surface at $\boldsymbol{\sigma}$, and that it is directed normally at the yield surface, $d\varepsilon^{p} = \dot{\varepsilon}^{p}dt$. Hence, the associated flow rule is also called the normality rule, and a geometric representation can be seen in Figure 3.3.

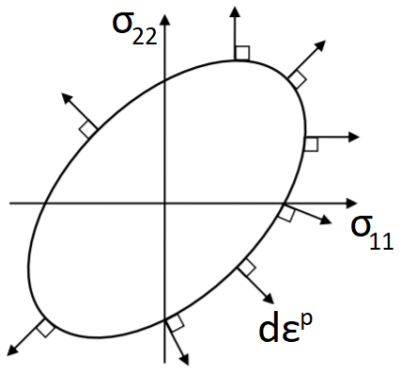

Figure 3.3: Geometric representation of the associated flow rule [1]

3.1.3 Hershey–Hosford Yield Criterion

Due to the material presumably being pressure-independent, elastic-plastic and isotropic, the high-exponent Hershey-Hosford yield criterion was employed. The main advantage of this yield criterion is the few independant anistropy coefficients. The yield function can be defined by equation

$$f(\sigma, R) = \varphi(\sigma) - \sigma_Y(R) \leqslant 0 \tag{3.10}$$

where the Hershey-Hosford yield criterion defines the equivalent stress as

$$\varphi(\sigma) = \sigma_{eq} = \left(\frac{1}{2}\left(\mid s_1 - s_2 \mid^m + \mid s_2 - s_3 \mid^m + \mid s_3 - s_1 \mid^m\right)\right)^{\frac{1}{m}} \tag{3.11}$$

where s_1, s_2 and s_3 are principal deviatoric stresses, and m defines the shape of the yield surface. $\sigma_Y(R)$ is the flow stress, defined by the yield stress and the isotropic hardening. For materials with FCC structure, m is set to 8, and for materials with BCC structure, m is set to 6. This is recommended from literature based on calculations using polycrystalline plasticity [28]. For a $m = 2$, the yield criterion is equal to von Mises criterion, while a higher m becomes similar to the Tresca criterion. It should be noted that a high m may lead to numerical errors, and has thus been avoided.

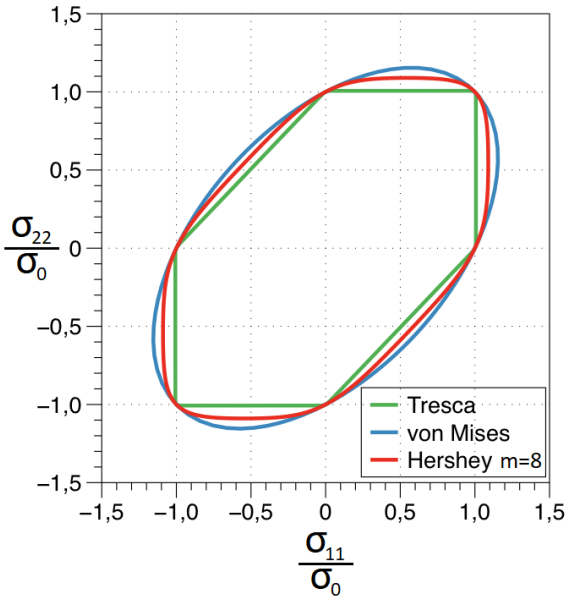

Figure 3.4: Geometric representation and comparison of Hershey-Hosford ($m = 8$), Tresca and von Mises yield criterion for plane stress conditions [1]

3.1.4 Work Hardening

Work hardening occurs when the material is strained plastically, making the material stronger up to the point of necking. This is easily spotted from the definition of the yield function. The elastic domain evolves during work hardening, hence expanding the yield surface. This plastic deformation leads to both movement of dislocations

and generation of new dislocations. When dislocations interacts, the material gets stronger, but the ductility decreases [29]. The flow stress from equation 3.10 is defined by

$$\sigma_Y(R) = \sigma_0 + R \tag{3.12}$$

where σ_0 is the yield stress and R is the isotropic hardening variable. During plastic deformation, R increases, thus increasing the flow stress in the material. The general isotropic hardening rule, equation 3.13, describes the rate of which the material is work hardened,

$$\dot{R} = h_R \dot{\gamma} \tag{3.13}$$

where $\dot{R}$ is the rate of work hardening, h_R is the hardening modulus and $\dot{\lambda}$ is a plastic parameter. It is assumed that h_R depends on the state of the material. In this Thesis, R is determined by an extended Voce law with three terms; equation 3.14,

$$R = \sum_{i=1}^{3} Q_i \Big(1 - e^{\left(-\frac{\theta_i}{Q_i} p\right)}\Big) \tag{3.14}$$

where Q_i are the saturation stresses, i.e., the maximum value R can take, θ_i are the initial hardening moduli and p is the equivalent plastic strain. Still assuming an associated flow rule, $\dot{\lambda} = \dot{p}$, the hardening modulus becomes

$$h_R = C_R(Q_R - R) \quad [1]. \tag{3.15}$$

3.2 Test Rig and Setup

Tensile tests were conducted in terms to investigate the material properties of both the AA6005A-T6 alloy with fibrous- and recrystallised microstructure, ensuring an accurate material behaviour in the numerical simulations. The tensile tests was executed and evaluated in cooperation with co-supervisor Miguel Costas and done according to ASTM.

3.2.1 Geometry and Methodology

Several tensile tests from different sections of the profile were performed in order to obtain the material properties of both the fibrous- and the recrystallised version of the AA6005A-T6 alloy. The dimensions of the extruded profile can be seen in Figure 3.5a, and the dimensions of the extracted tensile tests can be seen in Figure 3.5b. The tensile tests was extracted in an equal manner for both AA6005A-T6 alloys.

All uniaxial quasi-static tensile tests were carried out in room temperature using an Instron hydraulic testing machine at a speed of 0.67 mm/min, which corresponds to a strain rate of 0.058 min^{-1}. The duration of each test was approximately 4 min, and during the test, the force acting on the specimen never exceeded 10 kN. The testing machine measured time, force and displacement of the specimen throughout the test.

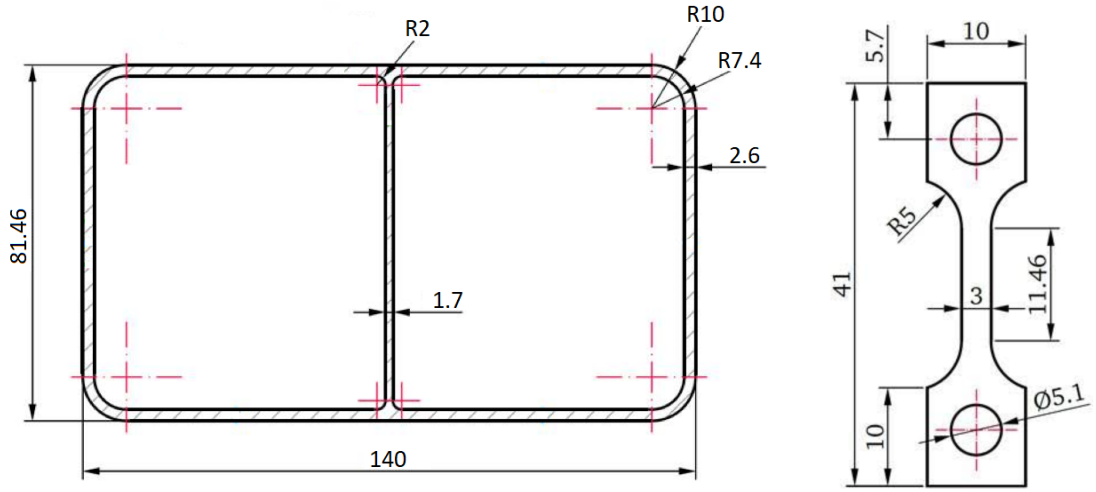

(a) Cross-section of extruded profile (b) Tensile test

Figure 3.5: Dimensions of cross-section and tensile tests and location of extraction

3.2.2 Recrystallization

When the profiles used in this Thesis were extruded, care was taken to attain wanted material properties and special attention was focused on the recrystallisation. Recrystallization occur when a certain threshold in deformation energy is passed. At this threshold new grains can form and the material do so to lower its internal energy. The deformation energy depends on temperature, strain and strain rate, while the threshold depends on the amount of alloying elements that forms dispersoids, which is typically Mn and Cr for aluminium alloys. Both the threshold and the deformation energy was altered to acquire the fibrous- and recrystallised qualities for the AA6005A-T6 alloy.

The alloy was extruded at a slower speed than usual, approximately 15 m/min, with a high billet temperature of 500°C, creating a fibrous microstructure. The higher the temperature, the more deformation energy will be annulled. A variant of the alloy with higher threshold was used giving an improved resistance towards recrystallisation in the material. The profile was aged to get T6 temper, which is equal to T5 for nearly all 6xxx extruded profiles. The ageing was carried out at 185°C for 220 min. In similar fashion a version of the alloy with low threshold was extruded to attain the recrystallised microstructure at approximately 30 m/min, resulting in a high strain rate. The billet temperature was low, and measured to approximately 450°C.

3.3 Results

The result of this treatment can be seen in Figure 3.6a and Figure 3.6b, where the difference of the recrystallised- and the fibrous microstructure of the AA6005A-T6 alloy are illustrated.

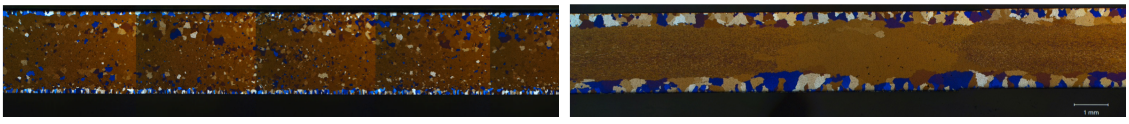

(a) Recrystallised microstructure (b) Fibrous microstructure

Figure 3.6: Microstructure of the extruded profiles

3.3.1 Recrystallised Microstructure

First, the recrystallised AA6005-T6 alloy was analysed carefully, and both the base and sections near the centre of the top-, middle- and side wall were investigated methodically. The tensile tests extruded from the base tested the extrusion welds influence, and the extraction area of the tensile tests are marked with red and blue circles, Figure 3.7. Three specimens were extracted at 0°, 45° and 90° relative to the extrusion direction for the tests near the centre to determine any anisotropy in the material. The test near the centre are marked with blue circles, while the base material, marked with red circles, were only extruded at 0° and 90° relative to the extrusion direction. In Figure 3.8, the extraction procedure of the tensile tests near the centre of the specimen is illustrated for both the top wall, Figure 3.8a, and middle wall, Figure 3.8b. The blue lines corresponds to the weld lines in the profile.

To account for any inaccuracies in the geometry, each specimen was measured using a micrometer. The micrometers zero were calibrated before each specimen, securing an accurate measurements. Both the thickness and the width was measured at five separate points along the gauge length. The gauge length, L_0, seen in Figure 3.5b, corresponded to a length of 11.46 mm and was very important when obtaining the stress-strain relationship. The accurate measurements of the gauge width and thickness for each test of the recrystallised alloy can be found in Appendix A in Table A.2, while the description of the abbreviations used in the engineering stress - strain curves can be found in Appendix A in Table A.1.

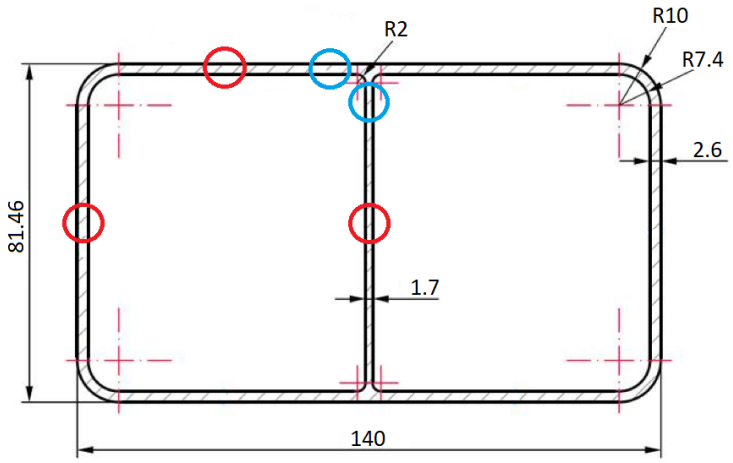

Figure 3.7: Extraction area of tensile tests

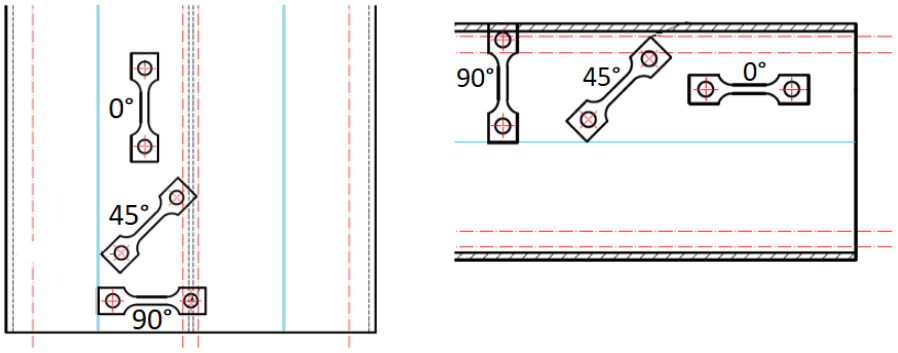

(a) Extraction view of top wall tests

(b) Extraction view of middle wall tests

Figure 3.8: Extraction view of top- and middle wall

3.3.1.1 Experimental Result

Three tensile tests were extruded from the middle- and top wall near the centre at 0°, 45° and 90°, together with three tests of the base of the middle-, side- and top wall at 0° and 90° relative to the extrusion direction, resulting in a total of 36 tensile tests. All the engineering stress-strain curves were computed using DIC and can be found in Appendix B in Figure B.1. Representative engineering stress-strain curves of each tests is presented in Figure 3.9.

Small deviation in the representative engineering stress-strain curves were noticed, Figure 3.9. The Young's Modulus was determined to be approximately 65 GPa for all tests, while the yield stress altered from 270 MPa to 290 MPa depending on location and direction relative to the extrusion. A low degree of hardening was observed, which is expected for a T6-tempered AA6005A-T6 alloy. For the tests extracted from the base, some difference in ductility were noticed regarding angle relative to extrusion direction. The top- and side wall possessed the most ductile behaviour, and the middle wall the least, easily seen in the level of strain at failure. For the tests taken close to the centre, the difference in ductility was not as significant, and the middle- and top material had very similar behaviour. The material behaviour of tests extracted at the base and at the centre did not experience any relevant difference, and it was assumed that this was the case for the fibrous microstructure as well.

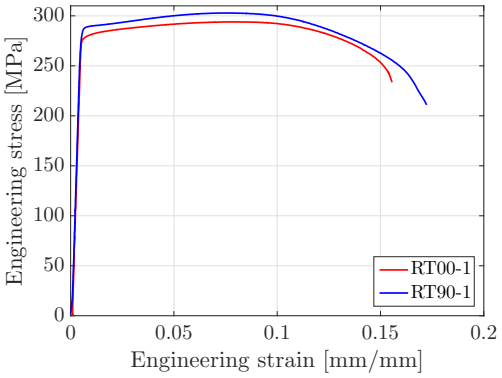

(a) Comparison of representative samples of top wall, base

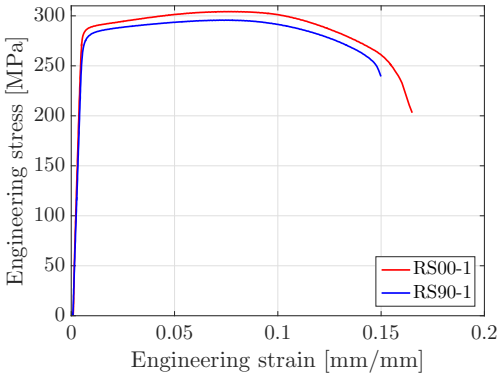

(b) Comparison of representative samples of side wall, base

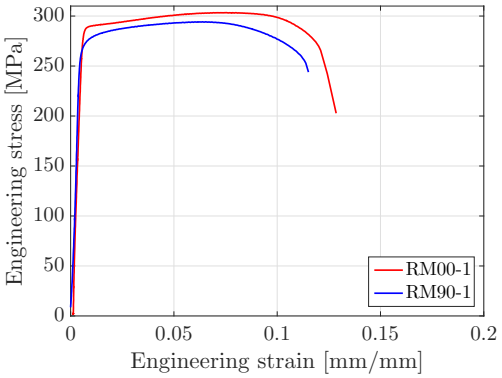

(c) Comparison of representative samples of middle wall, base

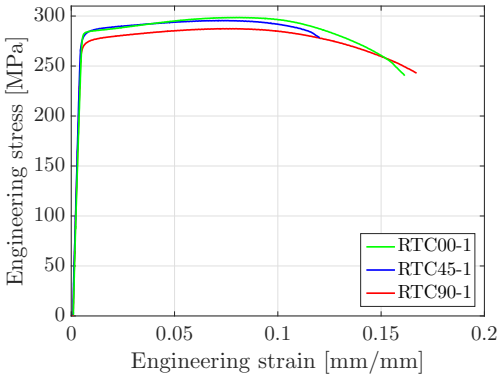

(d) Comparison of representative samples of top wall, near centre

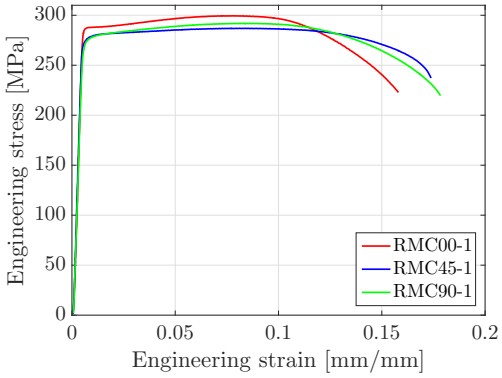

(e) Comparison of representative samples of middle wall, near centre

Figure 3.9: Engineering stress-strain curves for top- ,side- and middle wall specimens (0°, 45° and 90°)

3.3.2 Fibrous Microstructure

For the alloy with fibrous microstructure, three separate tests were extruded from the base of the middle- and top wall at 0°, 45° and 90° relative to the extrusion direction, resulting in a total of 18 tests. The gauge length and width of the specimens were measured in similar fashion as the recrystallised alloy. The accurate measurements can be found in Appendix A in Table A.5. The description of the abbreviations used in the engineering stress - strain curves for the fibrous microstructure can be found in Appendix A, Table A.4.

3.3.2.1 Experimental Result

The tensile tests were conducted in identical fashion to the recrystallised alloy, giving the best possible basis for comparison, Figure 3.10. All the engineering stress-strain curves for the alloy with fibrous microstructure can be seen in Appendix B.2. The largest deviations were noticed in samples taken at 0° relative to the extrusion direction, but a overall good compliance was observed. The results for test three of the top wall at 45°, (FTC45-3), was disturbed by an excavator, thus caution should be taken when analysing this stress-strain curve due to unwanted data noise. All the stress-strain curves presented were found using DIC.

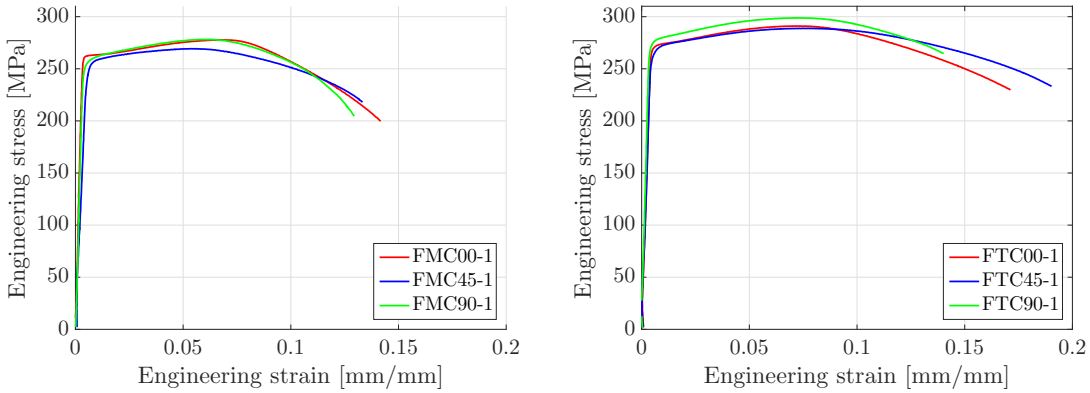

(a) Comparison of representative samples of middle wall

(b) Comparison of representative samples of outer wall

Figure 3.10: Engineering stress-strain curves for middle- and top wall specimens (0°, 45° and 90°)

The Young's Modulus was roughly equal in all directions relative to the extrusions with a value of 77 GPa, Figure 3.10. The yield stress in the middle wall is approximately 256 MPa, with small directionional variations, while the yield stress for the top wall is slightly higher at 273 MPa. A low degree of hardening was observed,

similar to the recrystallised alloy. The ductility of the middle wall is close to equal, while the top wall experienced a wider variation of ductility with regard to the extrusion direction. Samples from the top wall taken at 45°, (FTC45), behaved most ductile. This was easily seen in the strain value at failure. Overall, there is only a small deviation in the stress-strain curves for the different samples, except for the tensile tests at the middle wall were the results are more disperse.

3.3.3 Digital Image Correlation

The engineering strains were found conducting a 2D Digital Image Correlation (DIC) analysis of the tensile tests with the software eCorr. Prior to the test, the surface of the test specimens were spray painted with a speckle pattern. Further, a single camera was placed with the optical axis normal to the test specimen capturing the deformation at a frequency of 2 frames per second, or 4 Hz throughout the test.

In eCorr, a sufficiently long vector was fixed to the meshed gauge area of an undeformed test. The vector was created to be more than three times the gauge width. The mesh consist of structural bilinear rectangular elements (Q4), and during deformation, the elongation of the vector was extracted, enabling eCorr to calculate engineering strains. Strain resolution in this kind of analysis is typically 10^{-4}, depending on the camera used [30]. There are also uncertainties due to grayscale noise in the recorded images, and it should be noted that only in-plane strain could be measured in the DIC due to using only one camera. This makes the non-uniform strains recorded after necking invalid. The engineering stress is obtained by dividing the force measured from the testing machine by the average area of the specimen. Figure 3.11 shows the strain fields created in eCorr of a tensile test at start and at failure.

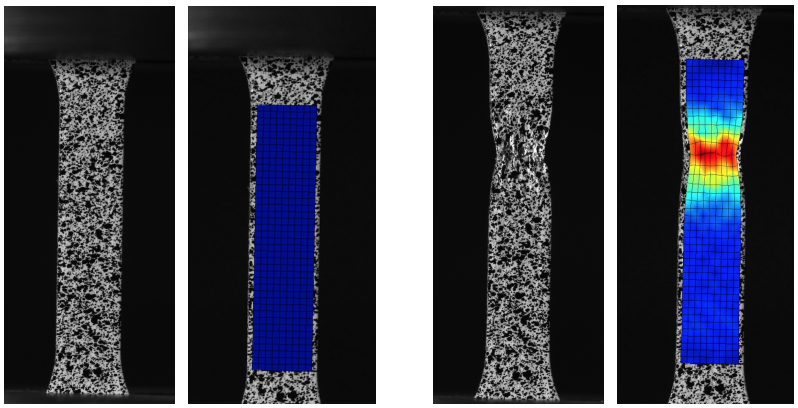

Figure 3.11: Undeformed and deformed tensile test with and without strain fields from eCorr

3.3.4 R-value

The R-value for both the middle- and top wall was calculated to attain a better understanding of the materials plastic anisotropy. The tensile tests specimens gauge width and thickness were measured post-mortem, only using the areas not influenced by the neck. From this, the width strain, ϵ_w^p and thickness strain, ϵ_t^p where calculated. As mentioned in section 2.2.2, the material experiences isotropic flow properties when $R_\alpha = 1$. A improved visualisation was obtained by plotting R-values for the different directions relative to the extrusions. The data attained from the tensile tests have been fitted to curve, Figure 3.12.

$$R_\alpha = \frac{\varepsilon_w^p}{\varepsilon_t^p} \tag{3.16}$$

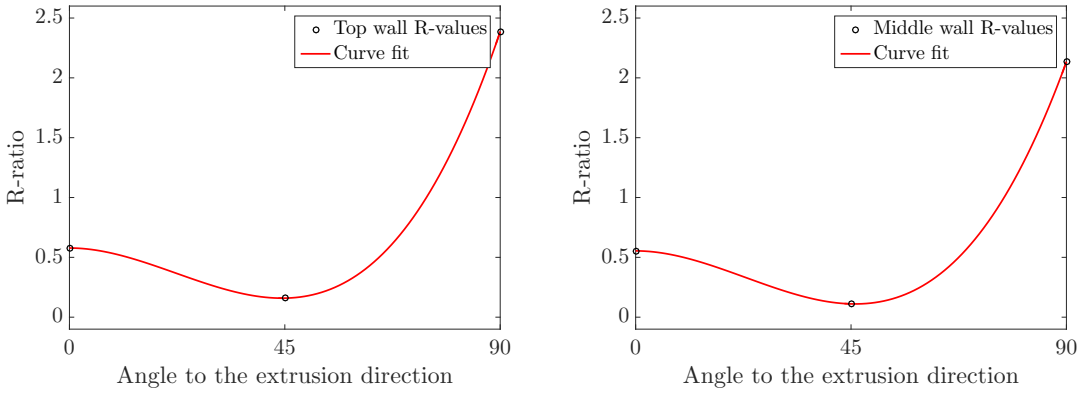

(a) Top wall (recrystallised)

(b) Middle wall (recrystallised)

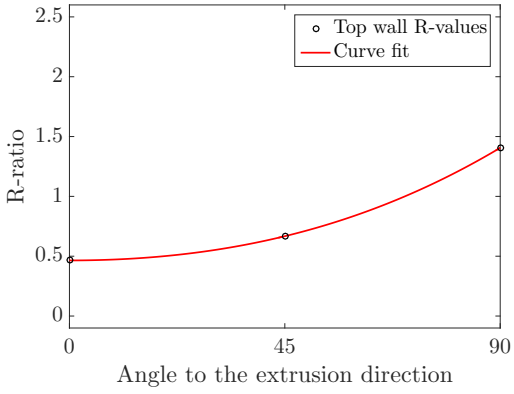

(c) Top wall (fibrous)

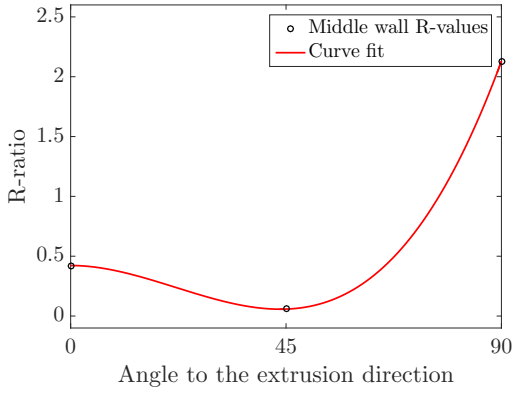

(d) Middle wall (fibrous)

Figure 3.12: Graphical representation of the R-value of both microstructures

The results implies that the material exhibit some degree of anistropy. For the recrystallised AA6005A-T6 alloy, the middle- and top wall reveal the same expected straining behaviour, while the top wall for the fibrous AA6005-T6 alloy has a higher R-value at 45° than 0°, which is unusual and unexpected. The calculated values can be found in Appendix B.3.

3.3.5 Material Characterization

Even though a moderate degree of anisotropy was discovered, the material was modelled isotropic. This significantly reduced the complexity and saved computational time in comparing to employing an anisotropic material model. The hypo-elastic constitutive model described was adopted to display the materials behaviour in numerical simulations. For the recrystallised AA6005A-T6 alloy, the first test in the extrusion direction of the top wall tests near the centre (RTC00-1) was used as a representative test, and an elastic modulus of 64.88 GPa was found. For the fibrous AA6005A-T6 alloy, the third test in the extrusion direction of the outer wall (FTC00-3) was used as a representative test with an elastic modulus of 77.87 GPa. For both material models, Poisson's ratio was assumed to be 0.33, and the linear elastic behaviour were described using Hooke's law, while the Hershey-Hosford yield criterion was utilised when capturing the transition from elastic to plastic deformation in the material, equation 3.3 and equation 3.11. A customary value of $m = 8$ was employed due to the FCC crystal lattice in the aluminium alloys. Further, an associated flow rule and an extended Voce law was adapted as the work-hardening rule and then calibrated, equation 3.14. The parameters of the extended Voce hardening law for the fibrous- and recrystallised microstructure were established, Table 3.1.

Table 3.1: Parameters of the extended Voce hardening law

	σ_0 [MPa]	θ_1	Q_1 [MPa]	θ_2	Q_2 [MPa]	θ_3	Q_3 [MPa]
Fibrous	272.3	5824.9	2.20	596.4	34.22	281.7	30.67
Recrystallised	275.7	7095.1	8.61	702.3	48.47	166.2	12.16

The material parameters were fitted to the experimental hardening curves using an inverse modelling run in Abaqus Standard under a LS-OPT framework, a graphical optimisation tool. This enabled the possibility to capture information regarding the post-necking behaviour. Only 1/8 of the tensile test was modelled, utilising three symmetry planes, thus reducing the computational time. The element size was set to 0.26 mm, using 10 elements through the thickness of the specimen. The bolt was modelled as a discrete rigid part, and then given an initial velocity to generate

stress and strains in the specimen. A virtual extensometer was created using two nodes representing half the gauge length to capture the engineering strain. The engineering stress was found by extracting the force from a reference point located in the discrete rigid bolt. The engineering strain and engineering stress were multiplied with respectively two and four, due to the use of the symmetry planes. The finite element model, with symmetry planes and bolt is presented in Figure 3.13a. A comparison of the representative engineering stress-strain curve and the numerical result for the fibrous microstructure are presented in Figure 3.13b.

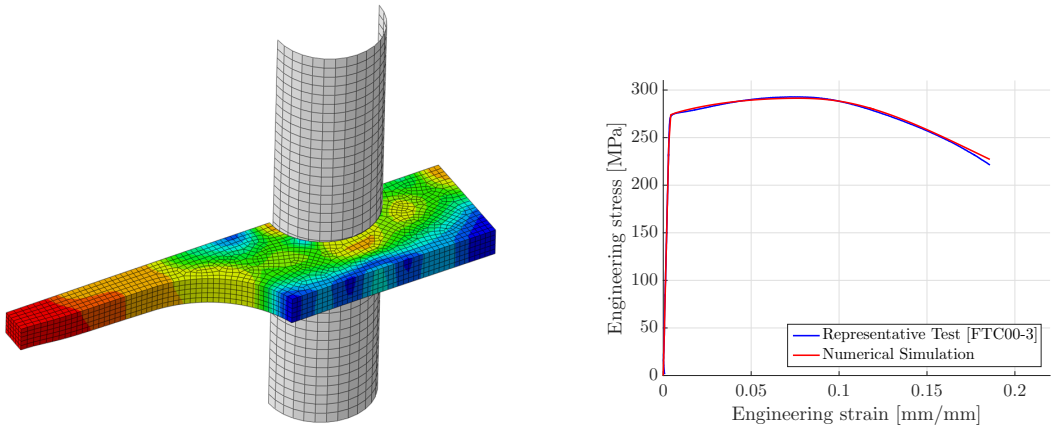

(a) Finite element model

(b) Engineering stress-strain curve

Figure 3.13: Finite element model of the tensile test and the engineering stress-strain curve of the experimental representative test of the fibrous microstructure and the corresponding numerical simulation

3.3.6 Damage Modelling

The model describing the behaviour at failure was based on the regularisation scheme proposed in section 2.3.2 and section 2.3.3. The parameters were obtained from the tensile tests. It was not possible to determinate when fracture initiates inside the specimen from first-hand observation of the tensile test. Using the point of failure observed on the surface could overestimate the Cockroft-Latham parameter, W_C. Hence, fracture was estimated using an iterative strategy on an explicit version of the tensile test, with a LS-OPT framework to determine fracture orientation and capture the inner failure of the specimen. Even though localisation occurs during the simulation, the discretisations of the elements is much smaller than the neck size making it reasonable to neglect this behaviour. From the iterative approach, with regard of the crack propagating from the centre of the specimen, the value of the Cockroft-Latham bending load parameter, W_C^b was found to be 168.67 MPa.

The pure membrane loading Cockroft-Latham parameters, W_C^m are mesh dependant.

Recalling equation 3.17, the shell elements length to thickness ratio was found, and the point of failure was satisfactory captured.

$$W_C^m = W_C^l + \left(W_C^s - W_C^l\right) e^{\left(-c\left(\frac{l_e}{t_e}-1\right)\right)} \tag{3.17}$$

The parameters, W_C^l, W_C^s and c were fitted similarly to Högström [31] and Morin [32], and vectors of length 3, 5 and 7 mm were placed in the necking region of the tensile tests. Their elongations were tracked and applied as boundary conditions with DIC. The mesh size was chosen as a divisor of the vectors length, and set to 1 mm. The vectors elongation was computed to the point of fracture. A FE model in Abaqus/Explicit consisting of three shell elements with corresponding thickness and size as the vectors length from the DIC analysis was created. These elements have been loaded in uniaxial tension applying the length increments obtained from the DIC. The Cockroft-Latham parameters for the different element sizes were numerically integrated, considering the damage at the final step. The Cockroft-Latham parameters for both the fibrous- and the recrystallised alloy were established, Table 3.2. These values are then fitted to equation 3.17 resulting in Figure 3.14.

Table 3.2: Cockroft-Latham parameters

	W_C^b [MPa]	W_C^s [MPa]	W_C^l [MPa]	c
Fibrous	168.67	121.124	44.7038	0.8599
Recrystallised	170.50	69.1112	3.6388	0.2188

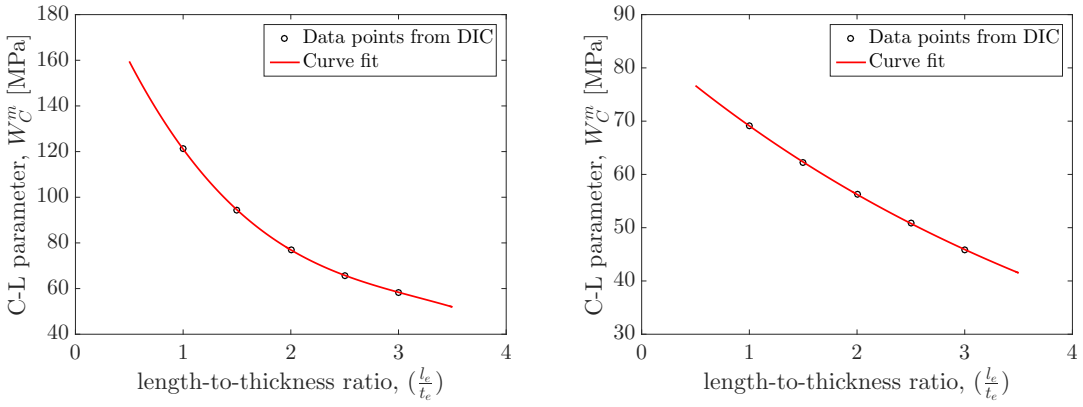

(a) Fibrous microstructure

(b) Recrystallised microstructure

Figure 3.14: Mesh dependency of the Cockroft-Latham parameter under pure uniaxial membrane loading

3.4 Discussion of the Material Model

From the quasi-static uniaxial tensile tests, the materials strain data using DIC analysis with the software eCorr were accumulated. This data were processed and the material characteristics were described using Hooke's law, Hershey-Hosford yield criterion, an associated flow, extended Voce law and Cockroft-Latham failure criterion. From these procedures material cards for both the alloy with fibrous- and the recrystallized microstructure were implemented for use in Abaqus/Explicit to be runned with SIMLabs Metal Model. The full material cards for both the alloy with fibrous- and recrystallised microstructure can be found in Appendix B. The thickness of the middle wall has a smaller thickness of 1.746 mm compared to the outer wall thickness of 2.565 mm.

The recrystallised tensile tests did exhibit clear ductile dissimilarity for samples taken at 45° relative to the extrusion direction. However, tests taken from the base at 90° relative to the extrusion direction of both the middle-, side-, and top wall experienced a higher yield strength, ultimate strength and had increased ductile behaviour. This behaviour was backed by studies done by Chen et. al. (2009) on stress-strain behaviour of aluminium alloys at wide range of strain rates [24]. The behaviour for tests extruded near the centre of the profile where more or less similar. The difference in results obtained from tests taken at the base of the walls, did not exhibit any abnormalities compared to tests taken near the centre.

For the fibrous tensile tests, the ductility of the samples taken at 45° relative from the extrusion direction were found to be greater than 0° and 90°. This could be caused by the fracture mode. The 0°- and the 90° tests experienced clear shear fracture surfaces, while the 45° tests showed tendencies of a "cup and cone" fracture. This behaviour was also found in a study conducted by Formeau et. al. (2013) on anistropic failure modes of high-strength aluminium under varius stress states [33]. The outer- and the middle wall experienced a lower yield stress at 45° relative to the extrusion direction.

The middle wall have approximately 17 MPa lower yield stress than the outer wall, were the biggest disagreement was at 90° relative to the extrusion direction at 21.1 MPa. The ultimate yield stress were found to be 6% higher for the outer wall, and additionally the samples from the outer wall were notably more ductile than the samples from the middle wall.

Deviation noticed in the tensile test was most likely caused by difference in the crystal structure. The degree of recrystallization could differ from the middle- and top wall due to the thickness, where the middle wall have a more fibrous structure. This

structural dissimilarity was caused by the fact that it is harder to cool the middle wall directly with water spray in the extrusion process. Deviations could also be caused by microstructural weaknesses in the different specimens. The anisotropy measured was higher than anticipated, and the use of the isotropic Hershey-Hosford yield criterion could produce numerical results which deviates from the experimental results. Further, the whole profile were assumed to experience the same material properties. This assumption may be inaccurate affecting the accuracy of the numerical simulations.

4 Stretch Bending

The failure of the extruded aluminium profile for different combinations of nominal tension and bending forces were inspected utilising a stretch-bending rig. The test design was established to create the desired failure behaviour. The results were evaluated by simulations of an introductory model together with simplified analytical calculations. A laboratory setup was introduced, describing the dimensions of the test rig together with support mechanisms and loading cells. In addition experimental tests were conducted. The component utilised in the stretch bending rig were double chambered AA6005A-T6 profiles with a length of 1.8 m and the cross-sectional thickness in the middle wall and outer walls were respectively 1.74 mm and 2.56 mm.

4.1 Numerical Model

Preliminary studies were conducted and an introductory numerical model was created in Abaqus/Explicit to gain a deeper comprehension, finding the best way to capture failure of the extruded profile in the stretch-bending rig. Explicit FE simulations were used as they are well suited for nonlinear quasi-static problems involving contact or material failure problems where small time increments are required. Each time increment is computationally inexpensive and equilibrium iterations are not necessary. The grip- and trigger section were the most emphasised factors, as these were evaluated to be critical in a safe test design. Care was taken to ensure that the test were within the acceptable region giving good resolution and high accuracy if the forces applied.

The material characteristics were implemented using the validated material models found in Appendix B. Due to symmetry, the cross-section dimensions of the double chambered cross-section was only extruded half the original length, 900 mm, and implemented as a deformable part with fully integrated shell elements with five integration points through the thickness, Figure 4.1. This was done to reduce artificial strain energy. The symmetry plane and horizontal actuator are identified with red markings. Additionally, appropriate boundary conditions were created.

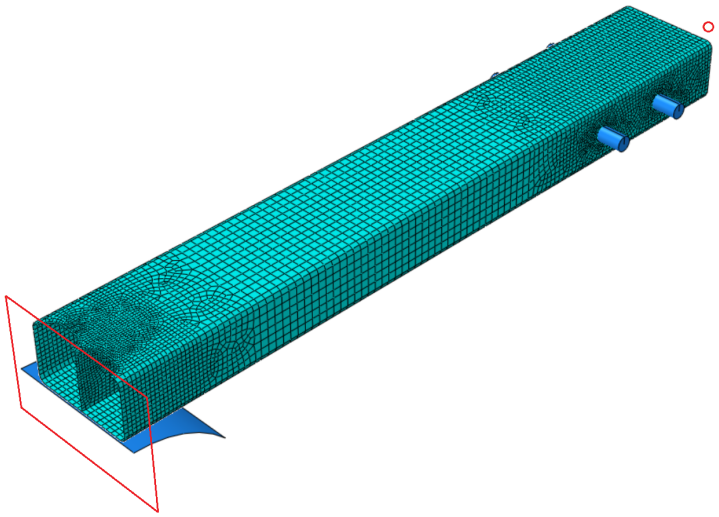

Figure 4.1: Preliminary numerical model

The critical damage factor, D_C, was calculated for each integration point, and an element was only removed when the damage factor was equal to unity in all five points. When employing shell elements, the loading was mainly carried by membrane actions, and the bending stresses were low, Figure 4.2 [4].

In Abaqus/Explicit only general-purpose shell elements can be used. The elements used were linear 4-node shell elements with enhanced hourglass control (S4R), as these elements were considered reliable and accurate for all loading conditions. These elements consider membrane strain as a default, and they do not suffer any transverse shear shock locking. The full profile was meshed with an approximate element size of 7.5 mm. A finer element size of 2 mm were applied where the fracture initiates as well as around the grip, giving a good length-to-thickness ratio. Using a coarser mesh on the sections not relevant to the failure reduced the computational time without influencing the result.

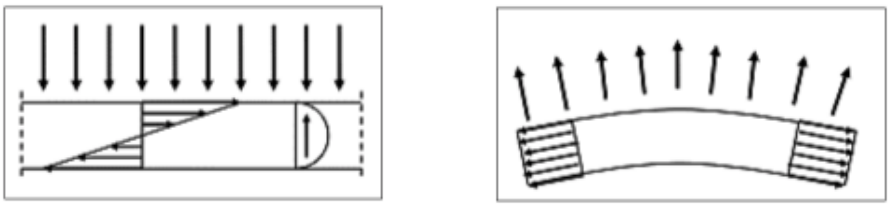

(a) Bending action (b) Membrane action

Figure 4.2: Load bearing in shell elements [4]

A transverse stiffness was implemented using equation 4.1, where G is the shear modulus, t is the thickness and 5/6 is the constant used for a homogeneous plate. The transverse stiffness of the outer- and middle wall was calculated to be 62579.6 MPa and 42593.1 MPa, respectively. The material was assumed to be homogeneous isotropic, and the shear modulus was calculated from equation 4.2.

$$K_{11} = K_{22} = \frac{5}{6}Gt, \quad K_{12} = 0 \tag{4.1}$$

$$G = \frac{E}{2(1+\nu)} \tag{4.2}$$

These equations were derived from plate theory, which states that a plate is categorised as thin if the thickness to length ratio is less than 1/10. For a plate with this ratio, it is assumed that the middle surface acts as a neutral plane, meaning that $\varepsilon_x = \varepsilon_y = \gamma_{xy} = 0$, and the normal strains in the thickness direction are zero, $\varepsilon_z = \frac{\partial w}{\partial z} = 0$ [34].

At the top of the profile at the symmetry plane, two holes working as triggers were added, thus inflicting failure at wanted area, Figure 4.3. A die was implemented as an analytic rigid body with radius of 150 mm.

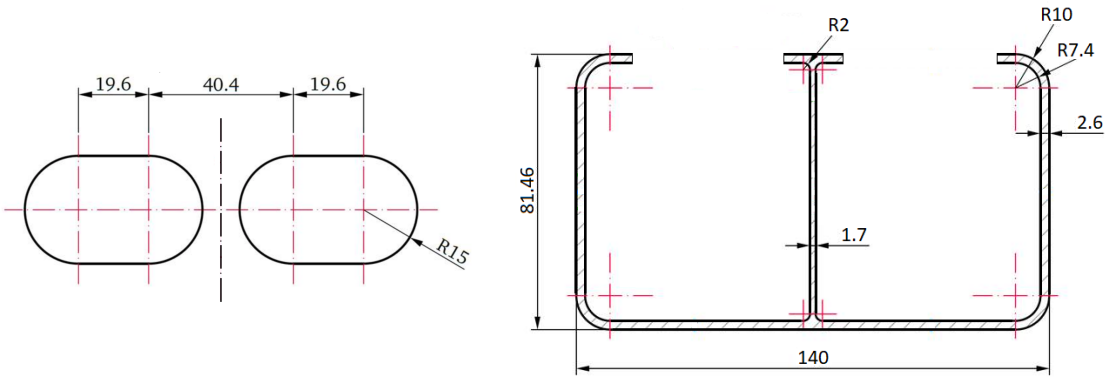

(a) Trigger dimensions

(b) Cross-section dimensions

Figure 4.3: Dimensions of trigger and cross-section at midpoint

Using Abaqus/Explicit, the contact constrains were enforced by the penalty method. This method keeps the number of unknown unchanged, but might produce an ill-conditioned set of equations. These constrains can be modelled using general contact or contact pairs algorithms. Although, due to the simplicity of the model, contact between the die and the profile were employed using the general contact algorithm. The general contact algorithm allowed for contact between regions of the model with a single interaction, and included interaction between all bodies with few limitations to the bodies surface [4].

Friction was minimised by employing a 2 mm thick sheet made of polytetrafluoreten (PTFE) between the die and the profile. In the numerical simulations, this sheet was not included, but a low friction coefficient of 0.2 was instead adopted.

The thickness of the walls were set to 2.56 mm and 1.75 mm on the outer- and middle wall. The loading conditions were created in two time steps. In the first time step, the horizontal actuator was given an initial load, and the velocity of the die was kept at zero, resulting in tensile forces. In the second time step, the die was given a velocity, inducing bending. This way, the magnitude of the tensile forces was controlled, while the die initiated failure. Attaining a stable solution in explicit FE simulations requires very small time steps. Running the simulations with a shorter time interval than the duration of the physical process enabled the possibility of reducing simulation time [26]. Hence, the loading of the horizontal actuator in the first time step was ramped over a time period of 0.3 seconds, and the velocity of the die was set to 18.5 mm/s over a time period of 2 seconds in the second time step. A second ramp function was defined and assigned to the die velocity to avoid introduction of stress waves caused by a sudden change in velocity. Thus, the velocity was applied over a time period corresponding to 10 % of the step time and was kept constant for the remaining time.

4.1.1 Grip Design

When the horizontal actuators move, tensile forces were introduced in the mounted profile. These actuators and the profile were joined together using four specially made 20 mm thick steel plates. The steel plates had two pre-made holes with a radii of 10 mm, compatible with M20 steel bolts, Figure 4.4. In the introductory model, the horizontal actuator was created utilising a reference point. And instead of implementing the grip plates in the preliminary numerical model, the analytic rigid bolts were constrained directly to the reference point, symbolising the grip section with a Multi-Point beam Constraint (MPC). The reference point was created to be a distance of 185 mm from the closest bolt, matching the grip sections dimensions. This generated the wanted behaviour and reduced the complexity of the contact definition.

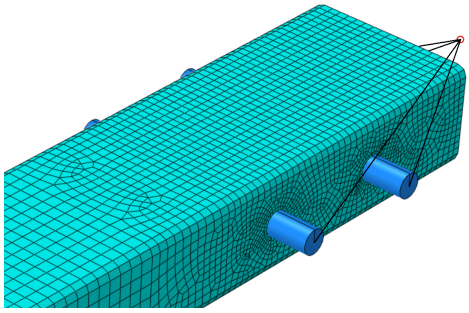

Figure 4.4: Initial bolt design with MPC constraints to the actuator rotation centre

Pure tensile forces were the critical loading condition and the profile needs withstand these forces without undesirable local failure at the grip section. The nominal capacity force required to initiate failure of the beam was calculated from equation 4.3:

$$\sigma_0 = \frac{F}{A_0} \tag{4.3}$$

where the cross-section area, A_0, was 957.4 mm^2 and the yield strength, σ_0, was 272.3 MPa, resulting in a required force of 260.7 kN. An investigation of the preliminary numerical model was conducted in Abaqus/Explicit. The bolts caused tearing of the profile at approximately 55 kN, implying that the initial grip section design was not sufficient. Local failure at the grip section on the profile was undesirable and pure tensile forces were clearly the critical loading condition.

4.1.1.1 Bolted Connection

Due to the local failure, an intricate examination of the grip design was executed. The local failure problem was approached by adding more bolts to the grip plates. The main advantages of this strategy were the simplicity in calculating the strength of both the bolts and the profile, as well as it is easily machined. Using Eurocode 9: Design of Aluminium structures, the grip section was designed according to European Standards [6]. The final bolted grip section design was found using trial and error, Figure 4.5. The calculations of shear-, $F_{v,Rd}$, bearing-, $F_{b,Rd}$ and tension resistance, $F_{t,Rd}$, can be found in Appendix D, while the main results are presented in Table 4.1.

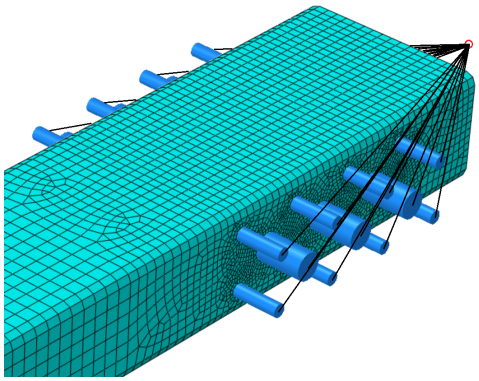

Figure 4.5: Final bolt design

Table 4.1: Results from analytical calculations

	Pre-made bolt design	Final bolt design
$F_{v,Rd}$	250.32 kN	625.80 kN
$F_{b,Rd}$	55.77 kN	109.08 kN
$F_{t,Rd}$	375.48 kN	938.70 kN

From the calculations, the bearing strength was found to be the critical factor. Even when excluding the safety factor, γ_{M_2}, the bearing resistance of the final bolt design could only withstand a tensile force of 136.31 kN. Running a preliminary simulation of the final bolted grip design in Abaqus/Explicit, the bearing failure at the grip section was investigated. The final bolt design started to experience yielding and excessive bearing deformations at approximately 125 kN, Figure 4.6.

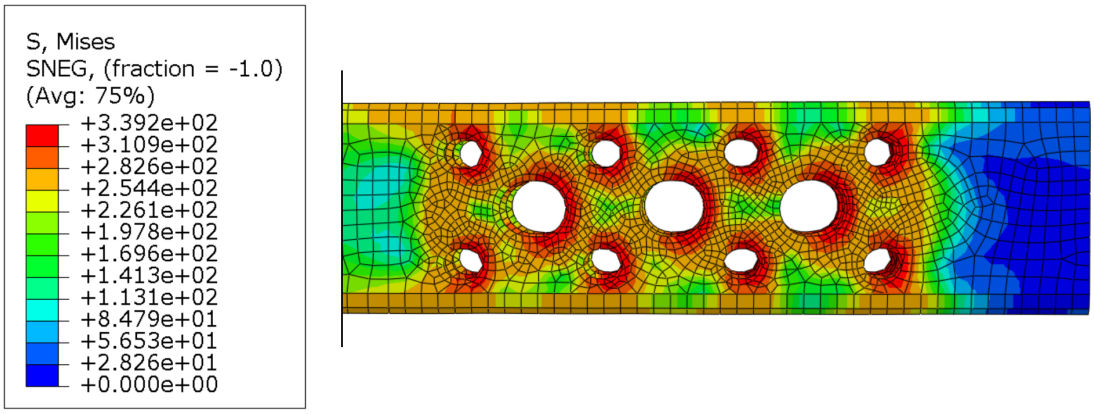

Figure 4.6: Yielding and bearing deformations on the profile

4.1.1.2 Clamped

The area exposed to tensile forces was increased by clamping high friction surfaces together to improve the bearing capacity of the profile. This distributed the forces over a larger area, reducing the local stress regions. Clausen et al. (2000) used the same set-up, clamping the surfaces with threaded bolts and tightening with a torque wrench. This approach was found to tolerate forces up to 200 kN, thus providing better suitability [13]. Partition faces were modelled on the side walls, constraining these to the rotation centre of the horizontal actuator with MPCs, Figure 4.7.

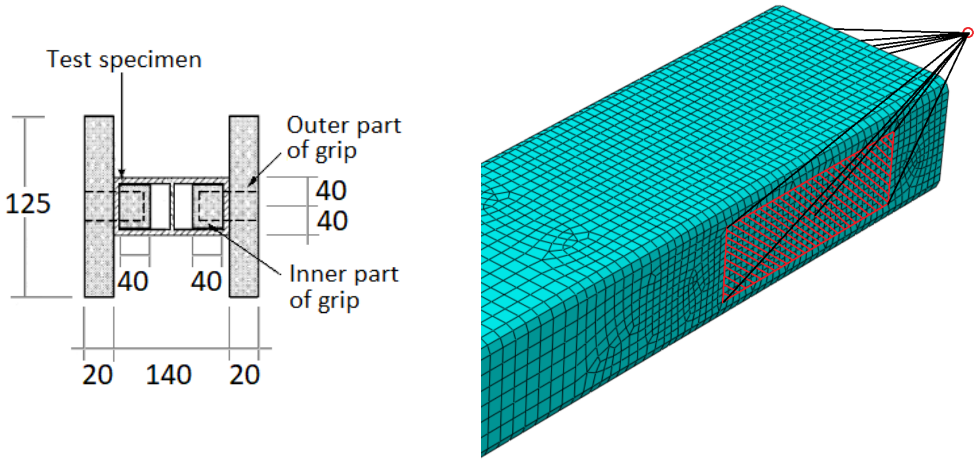

(a) Clamped design description (b) Numerical design

Figure 4.7: Description and numerical design of clamped grip

4.1.2 Trigger Design

The force required to initiate failure was reduced by adding an additional trigger in the middle section, decreasing the cross-sectional area. A hole with a radius of 12.5 mm was machined in the middle of the beam, reducing the cross-section area to 784.9 mm^2, Figure 4.8. Using equation 4.3, the maximum tensile force required to initiate failure was calculated to be 213.7 kN. Hence, reducing the force with 47.0 kN. The hole was placed 5 mm from the curved edge on the opposite side of the initial triggers, and simulations were executed in Abaqus/Explicit to ensure that the die would not crush the profile, creating unwanted buckling.

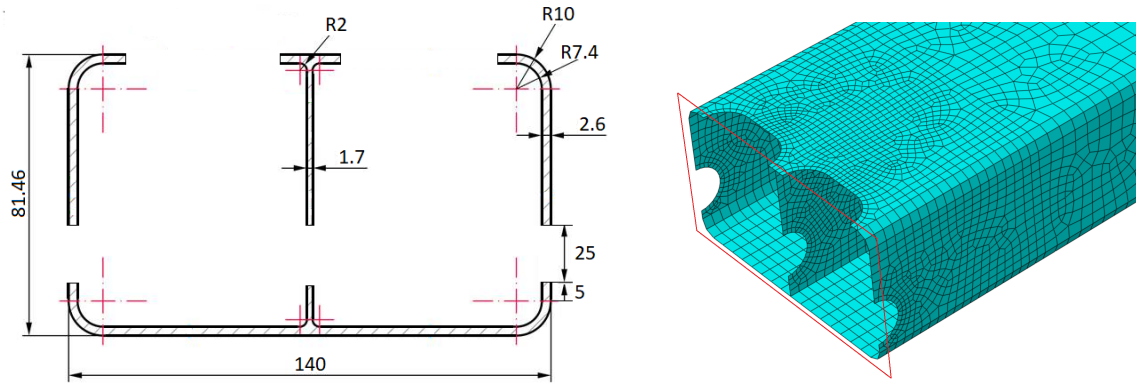

(a) Cross-section dimensions with new trigger (b) Numerical model

Figure 4.8: Dimensions of final cross-section and closeup of numerical model at midpoint

4.1.3 Preliminary Review

Running preliminary simulations of the stretch bending models in Abaqus/Explicit revealed an interesting trend. The element that failed first, the top element in the middle wall, failed in a pure tension state independently of a pure membrane- or pure bending load, Figure 4.9. From this finding, it was concluded that the same amount of information on the material model would be acquired for every loading combination, and thus the profile only needed to be tested for one loading combination. No occurrence of local deformation at the grip section was acquired by keeping the tensile forces at 50 kN throughout the simulation, while the die initiated the failure.

4.2 Numerical Results

The simulations of the numerical model were conducted with both the fibrous- and recrystallised material model, Figure 4.10. The fibrous model stood out from the

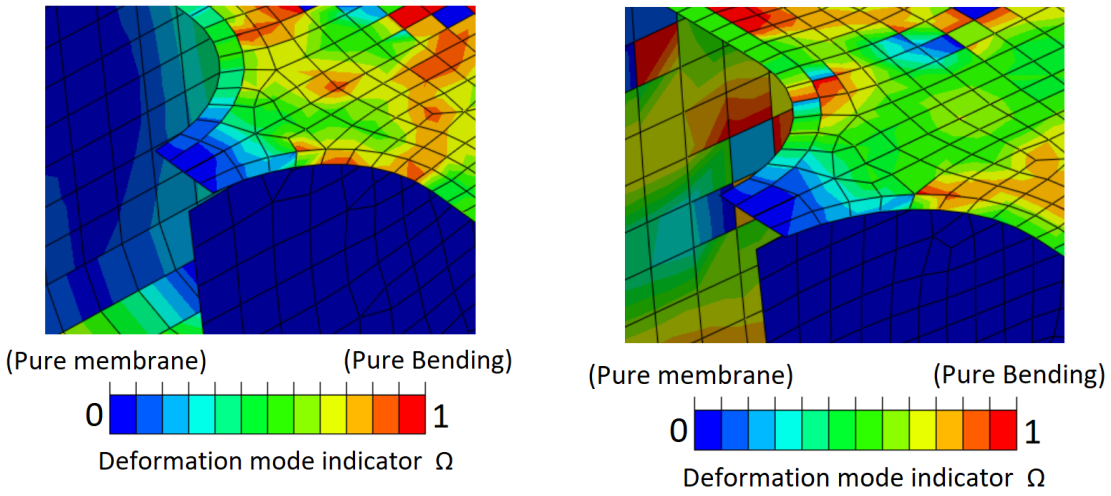

(a) Pure tensile loading

(b) Pure bending load

Figure 4.9: Element state at point of failure

recrystallised model by experiencing oscillation at the start of the model, and the slope of the force-displacement curve was steeper at the start before the magnitude descended. Failure occurred at a displacement of 28.49 mm for both models, but the die force of the fibrous model was 12.17 kN, and 12.33 kN for the recrystallised model at failure. The forces in the horizontal actuator behaved as expected and in similar fashion, only with minor oscillation in the fibrous material model.

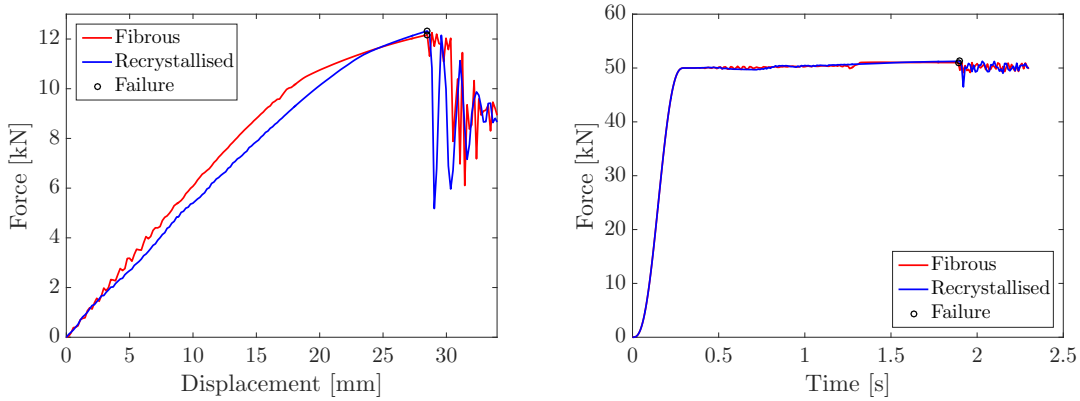

(a) Force-displacement (die)

(b) Force-time (horizontal actuator)

Figure 4.10: Numerical result of both material models

4.3 Parameter Sensitivity Evaluation

4.3.1 Fillets

In the introductory numerical model the fillets at the middle were disregarded. A study was conducted on the fillets to inspect how the model was influenced by the added bearing capacity. There were several ways to replicate the fillets with shell elements, but making the shell elements closest to the outer wall thicker and updating the transverse stiffness proved to be sufficient. Due to the dimensions of the fillets, the elements closest to the outer wall were modelled with an element thickness of 3.7 mm and a updated transverse stiffness of 90260.2 MPa. This model was compared to the introductory model, Figure 4.11, where a close-up of the fillet comparison can be seen in Figure 4.11a. Including the bearing capacity induced by the fillets increased the strength of the profile. This corresponded to an increase in strength of 5.39 % and 4.99 % respectively on the fibrous- and recrystallised material model.

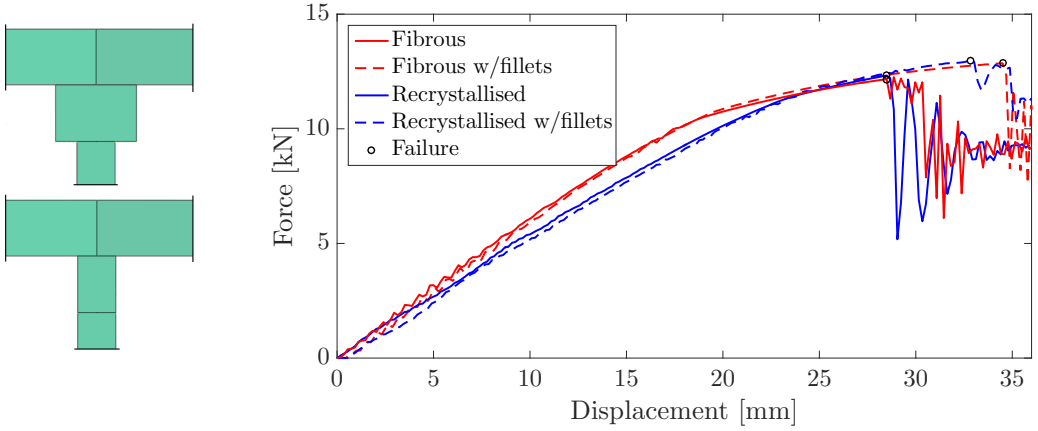

(a) Fillet size

(b) Force - displacement history

Figure 4.11: Fillet descriptions and results

4.3.2 Symmetry Plane

The effect of symmetry plane was studied, and a full scale model was created, Figure 4.12. The same loads, velocities and time scaling were applied to get an acceptable replication, Figure 4.13.

The full scale model required less force than the introductory model with symmetry planes to initiate fracture. This corresponded to a decrease of the strength of 3.42 % and 2.47 % on the fibrous- and recrystallised material model, respectively. The recrystallised material model also experienced a clearer force drop, with less oscillations after the failure. Due to increased complexity and adding of more elements to the model, the CPU-time increased with 55 %, which was not desirable.

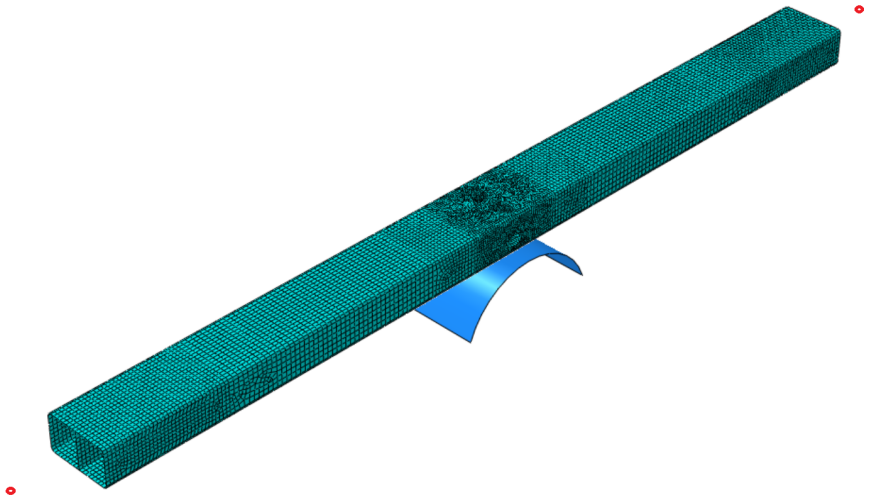

Figure 4.12: Full scale model

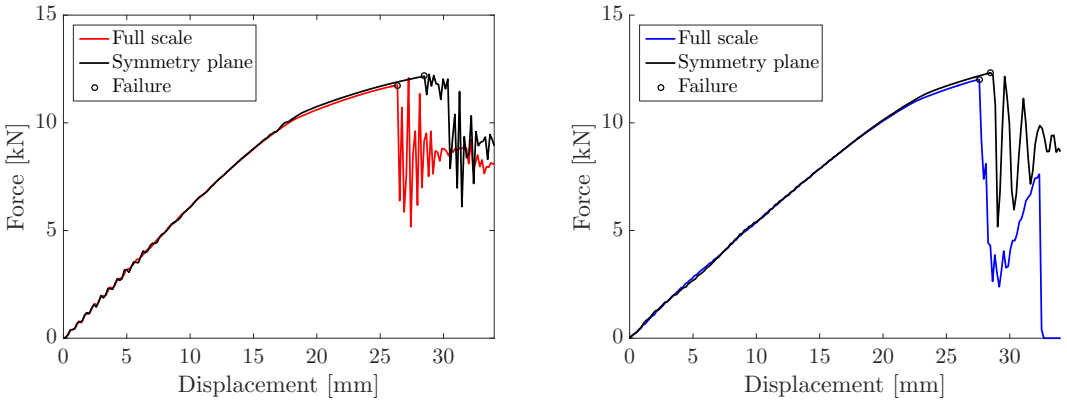

(a) Fibrous material model

(b) Recrystallised material model

Figure 4.13: Force - displacement history

A different failure mode were observed utilising the full scale model. After the failure of the middle wall, one of the side wall failed before the other, whereas both side walls failed simultaneously for the models utilising a symmetry plane, Figure 4.14. This behaviour were independent of material model.

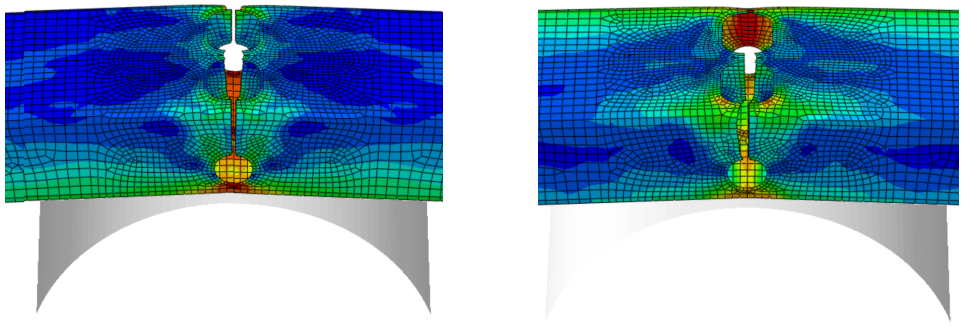

(a) With symmetry plane (b) Full scale model

Figure 4.14: Fracture behaviour comparison of model with symmetry plane and full scale model

4.3.3 Energy Study

Since time scaling increases the strain rate in the model, it can only be applied when rate-insensitive material models are employed. Excessive time scaling may cause spurious oscillations on the quasi-static solution. The ratio between the artificial strain energy, E_A, and internal energy, E_I were compared, validating that no significant dynamic effects were present in the simulation,. The assessment resulted in a ratio corresponding to 1.01 %, which was satisfactory. The kinetic energy, E_K, was negligible when compared to the internal energy and the external work, W_E. This equals the internal energy, giving a satisfactory energy history for a quasi-static analysis, Figure 4.15.

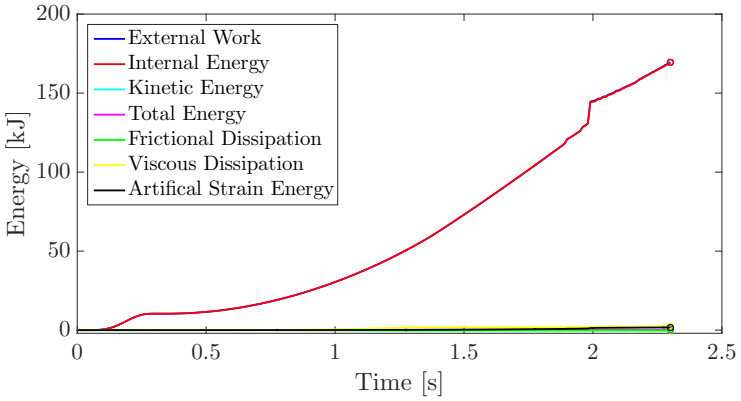

Figure 4.15: Energy history of the stretch bending simulation

4.4 Experimental Investigation

4.4.1 Test Rig and Setup

The test rig consisted of two horizontally mounted servo-hydraulic actuators and one vertically oriented servo-hydraulic actuator. A test may be performed in load- as well as displacement control. The horizontally mounted actuators were supported by 4 m tall steel columns made of cross-section HE 450B and a 6.4 m long horizontal beam of cross-section HE 240B, Figure 4.16. The length of the horizontally actuators were approximately 1.5 m, implying that the test specimen length could not exceed 2.0 m. The sizeable steel frame was employed ensuring that the stiffness requirements were met, avoiding deflections in the frame during testing [5].

The columns were bolted to steel plates on the laboratory floor, and the connection between the columns and top beam consisted of four bolts on each side. A die was mounted on the vertical actuator, which was located at the centre of the rig. The die lied on a spherical joint which stopped bending moments from transferring to the actuators piston. A more detailed overview of the actuators dimensions can be found in Appendix E.

4.4.2 Support Condition

An important aspect of the test setup was the profile connection with the grip sections to the horizontal actuators. The grip section had two pre-made holes compatible with M20 bolts, which was used to fix the grip section to the profile. The grip sections were connected with the hinged joint at the end of the horizontal actuators, hence the profile could rotate independently of the horizontal actuators position [5]. Or in static terms, the profile ends were simply supported, i.e. no bending moment. Further, the weight of the grip section introduced an undesirable local bending ef-

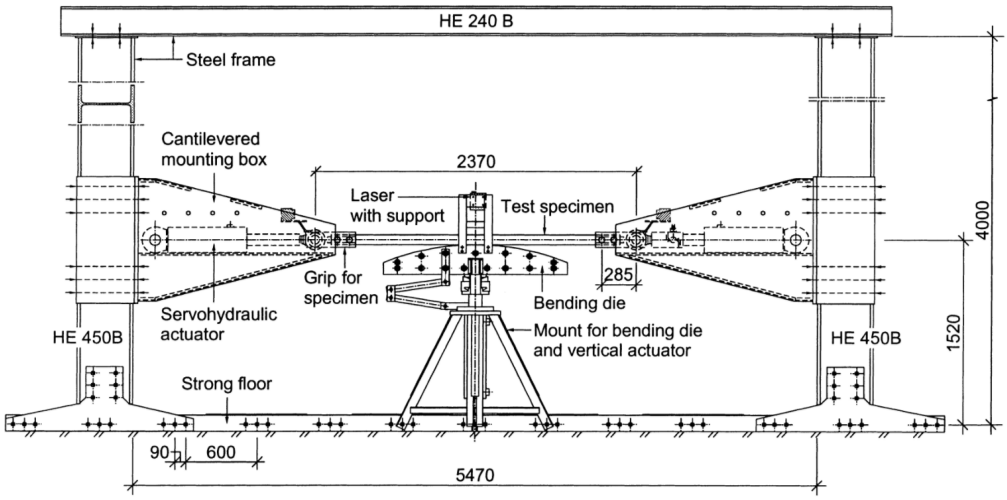

Figure 4.16: General overview of the test rig [5]

fect. This was annulled by adding a spring system, balancing out the moment about the axis through the hinge, Figure 4.17.

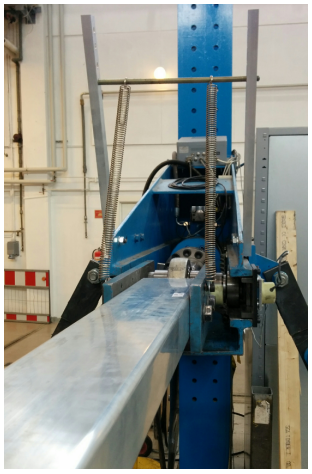

Figure 4.17: Grip section with spring system

4.4.3 Loading, Instrumentation and Measurements

The flexibility in the testing rig was provided by a specially designed process control system. The control system used information on the displacements and forces in the process and these quantities were measured during the whole test. In addition to the forces and displacements, the angles in the hinged supports were measured. In this experimental investigation three HD cameras were erected to capture the behaviour of the beam. Two cameras focused at the grip section, inspecting relative displacement and local deformations on the profile, and one camera tracked the failure of the middle section. Chessboard stickers were placed on the grip plates and

the profile, making it possible to analyse the relative displacement of the machine and profile. All three cameras operated with a frequency of 2 frames per second.

All three actuators had the same cylinder size and all were servohydraulicly controlled. They had a loading cell with a capacity of 330 kN, although the load cells were calibrated to a maximum force of 200 kN in order to obtain good resolution and high accuracy. The actuators were of type CA-VERKEN AB 180/90-300/85 SH-1524, and had a total stroke length of 300 mm.

The horizontal actuators were mounted in linear roller bearings and introduced the desired axial force in the test specimen. The vertical actuator guided the die, and was only subjected to compressive forces. Both the displacement, forces, angles and stretch zone sagging could be measured. In this Thesis, only the measurement of the forces and the displacement were of interest. Displacement was measured independently in the actuators by resistive displacement transducers with a resolution of 0.1 mm [5].

The force were measured by load cells produced by Dr. Brandt GmbH and were located on one of the horizontal actuators and the vertical actuator. The horizontal actuator without the load cell acted as a displacement controlled slave with regard to the master. Due to the symmetry of the test rig, the forces in the horizontal actuators were equal. The load cell on the horizontal actuator was of type KDZ-2, hence able to measure both tensile and compressive forces. In the vertical actuator, only measurement of compressive forces were needed, and the load cell was of type MKRL-100. The load cells were calibrated to an accuracy of 0.1 kN [5].

4.4.4 Process Control System

This test rig had a specially designed process control system, which consisted of three analogue controllers, a computer interface with a microprocessor and a PC programme, Figure 4.18. The desired load sequence was specified by the operator, i.e. either controlled movement by a load or by displacement of the actuators, in the PC programme. The frequency of logging was determined by the operator [5].

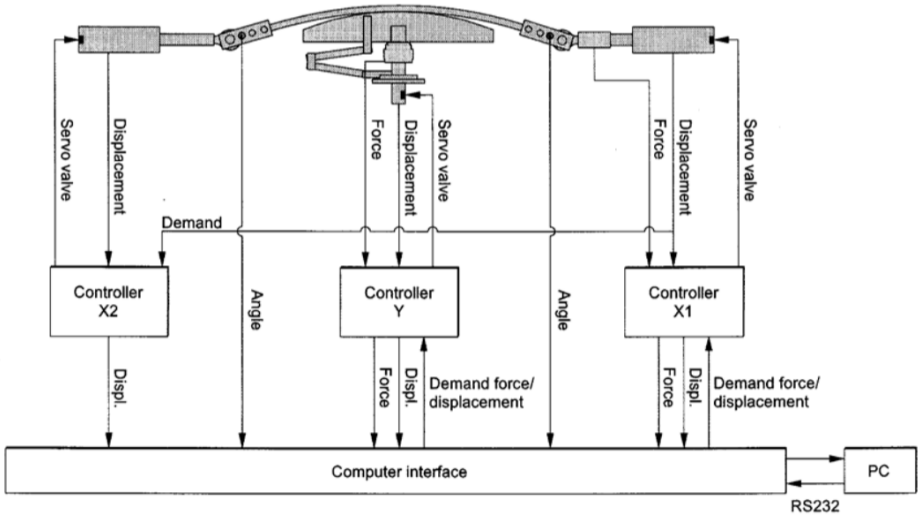

Figure 4.18: General overview of process control system of test rig [5]

4.4.5 Results

Three test of both the fibrous- and the recrystallised microstructure were conducted in the stretch bending rig with quasi-static loading. The profile was mounted to the grip sections in the testing rig, with the die fixed on the vertical actuator, and the profile mounted on the grip section fixed to the horizontal actuators, Figure 4.19a. The profiles were loaded 50 kN in tension before the die initiated failure, Figure 4.19b. The force-displacement curves of the die together with force-time curve of the horizontal actuators were established, Figure 4.20 and Figure 4.21.

(a) Final test set-up (b) Fractured profile

Figure 4.19: Test set-up and fracture of profile

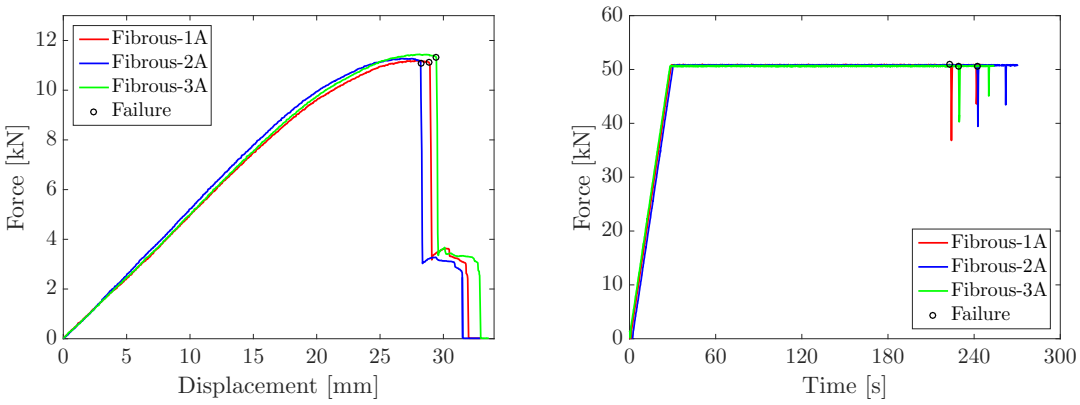

(a) Force-displacement (die) (b) Force-time (horizontal actuator)

Figure 4.20: Experimental result of extrusions with fibrous microstructure

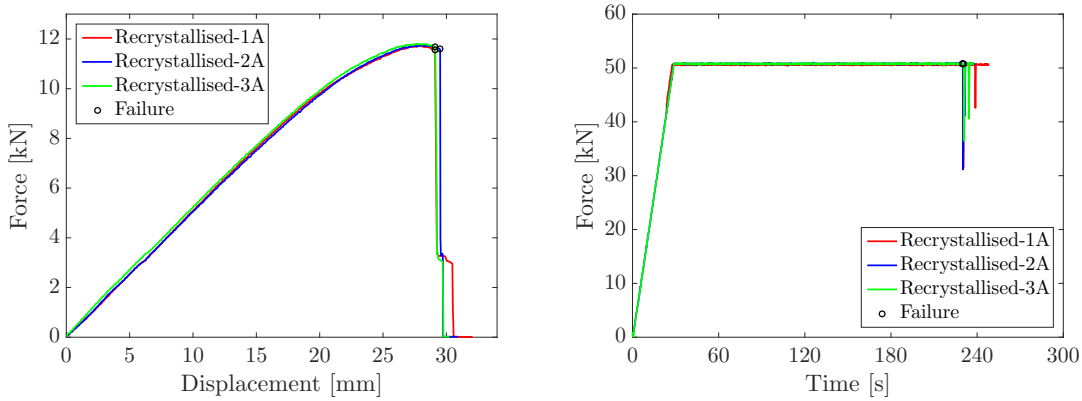

(a) Force-displacement (die)

(b) Force-time (horizontal actuator)

Figure 4.21: Experimental result of extrusions with recrystallised microstructure

Both the fibrous- and the recrystallised microstructure experienced good precision in the conducted tests. Before failure, a great extent of yielding were observed at the midpoint and at the sides of the top trigger, exemplified with the first fibrous test, Figure 4.22. Further, all the tests first failed at the middle wall, before failure occured on one of the side walls, depending on which side the middle wall buckled. The buckling of the middle wall created an unbalance in the force distribution at the midpoint of the extrusion, and this unbalance caused the failure of the first side wall. Shortly after tearing the first two walls, the last wall failed. This was seen as a small plateau after the first drop at approximately 30 mm of displacement on the force-displacement curve.

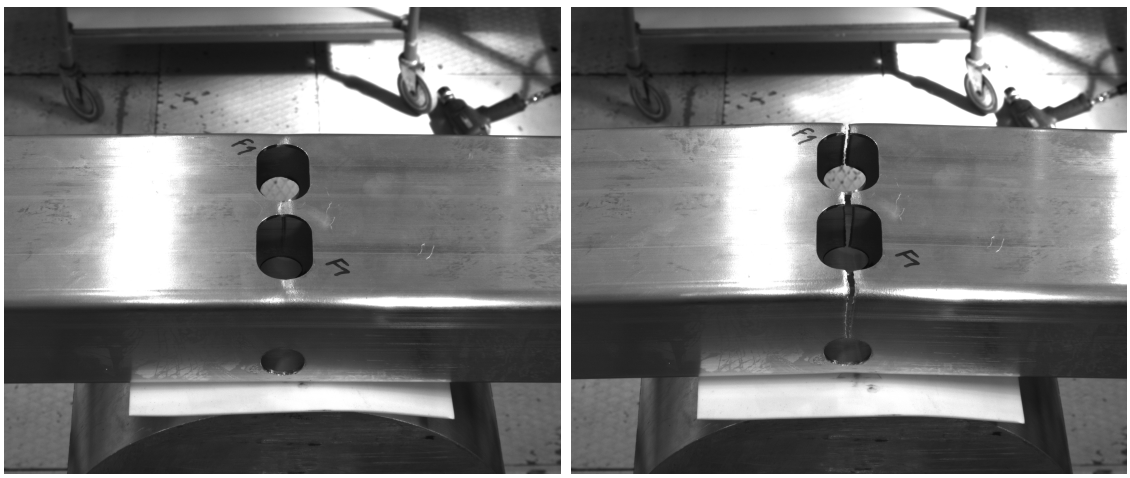

(a) Yielding at midpoint

(b) Total failure

Figure 4.22: Failure propagation in stretch bending rig

The fibrous microstructure exhibited respectively 1.95 % and 4.18 % variation of the die force and die displacement at failure. After the failure of the second wall, the force dropped between 7.5 and 8.1 kN, and the final wall endured roughly 3 mm of die displacement, postponing total failure. The recrystallised tests were nearly identical. The die force required to initiate failure only varied with 0.52 %, while the die displacement with 1.39 %. The third wall failed almost simultaneously as the first two, dissimilar to the fibrous microstructure. A summary of the die force and displacement at failure of the middle wall was established to get a full overview over the results, Table 4.2.

Table 4.2: Die force and displacement at failure

	Fibrous		Recrystallised	
	Force [kN]	Displacement [mm]	Force [kN]	Displacement [mm]
Test 1A	11.12	28.87	11.52	29.10
Test 2A	11.09	28.21	11.58	29.51
Test 3A	11.31	29.44	11.68	29.13

5 Axial Crushing

Quasi-static axial crushing tests were performed to validate the material models ability to replicate more complex deformation with complex stress states and severe bending. A nonlinear numerical model was investigated in Abaqus/Explicit, and a parameter sensitivity evaluation was performed. Further, experimental test have been performed to validate the results. The laboratory setup for the experimental tests, and the results for both the fibrous- and recrystallised material has been assessed.

5.1 Numerical Model

The axial crushing test was introduced using the same cross-section, material characteristics and numerical theory as the stretch bending model. The entire 3D model with length of 400 mm was designed without use of symmetry planes, Figure 5.1. The top 11 mm was shaped as a pyramid, acting as a trigger, creating the wanted folding pattern. The load was applied as a prescribed velocity at the top of a 3D analytically rigid plate which crushed the component. A friction coefficient of 0.3 was assumed between the rigid plate and the component, corresponding to literature [35]. The contact algorithm accounted for the shell thickness and considered the self-contact between the folds during folding. Further, the lower 80 mm of the model was fixed against translation and rotation in all directions, ensuring the wanted folding mode.

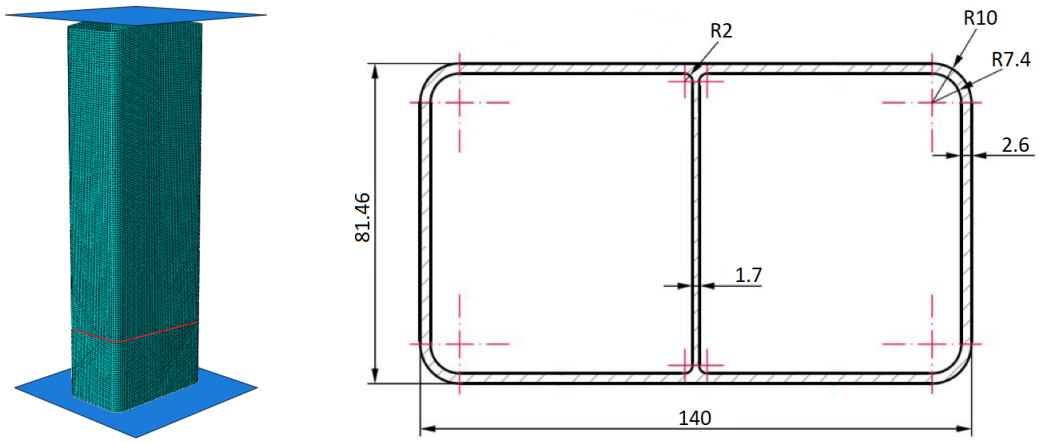

(a) Numerical 3D model (b) Cross-section

Figure 5.1: Test setup and numerical model

The model was further meshed using linear 4-node shell elements with enhanced

hourglass control (S4R). The element size was set to 2.56 mm giving a length-to-thickness ratio of 1 for the outer walls and 1.46 for the inner wall. Fully integrated elements were utilised with five integration points through the thickness to reduce the artificial strain energy.

5.2 Numerical Experiments and Results

Explicit FE simulations are well-suited for highly nonlinear quasi-static problems where the the component are exposed to strain localisation and severe bending. Simulations of the model were conducted in Abaqus/Explicit with a time scaling factor of 4300. The model was simulated with a velocity of 850 mm/s over a time period of 0.3 seconds, immensely reducing the run time. A smooth ramp function corresponding to 10 % of the total time period was defined to ensure quasi-static conditions and to avoid introduction of inertial effects such as stress waves. The results were evaluated after 250 mm of deformation and the corresponding force-displacement curve for both fibrous- and recrystallised material were established, Figure 5.2. Each peak on the force-displacement curve corresponds to the completion of one fold. Signs of fracture were detected at the corners, and at the connection of the inner- and outer walls.

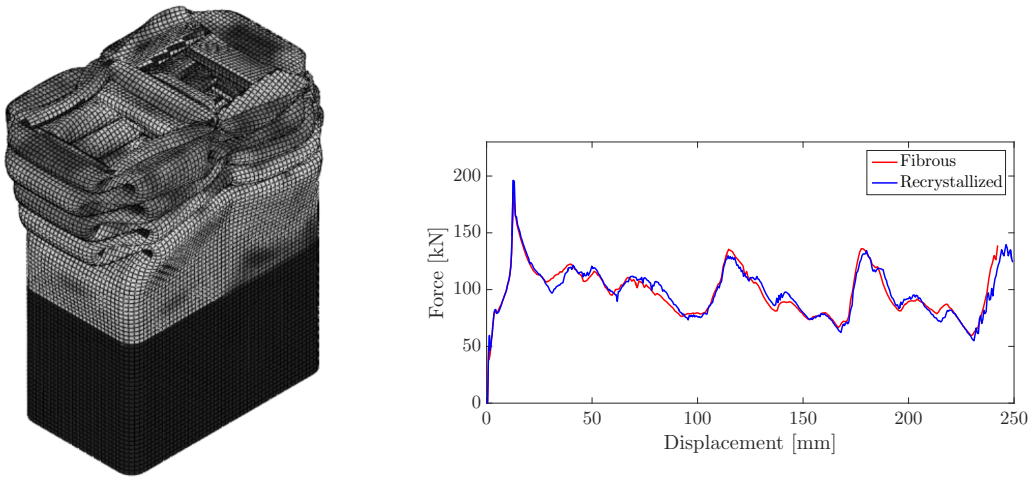

(a) Deformed component (b) Force-deformation history

Figure 5.2: Deformed component and force-displacement curve from the numerical model after 250 mm of deformation

5.3 Parameter Sensitivity Evaluation

5.3.1 Fillets

In the same manner as the stretch bending model, the introductory numerical model disregarded the fillets connecting the middle- and outer walls. A study directed at the fillets was done, and after a high level assessment, the thickness of the shell elements closest to the outer wall were set to 3.7 mm, and their transverse stiffness was updated to 90260.2 MPa. This method has shown to replicate fillet behaviour in a good manner [23]. The force-displacement curve can be seen in Figure 5.3b. A close-up of the fillet comparison can be seen in Figure 5.3a, where the lower picture is the introductory model.

Increasing the thickness of the elements closest to outer wall did not influence the force-displacement curve in a prominent fashion, and the model experienced the same symmetric folding. However, the force-displacement curve shifted to the right, and the peak forces are higher.

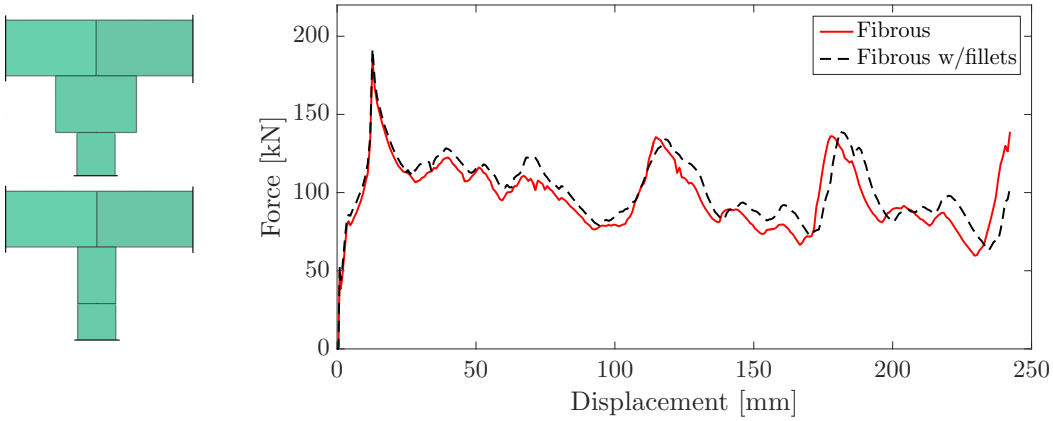

(a) Fillet size

(b) Force - displacement history

Figure 5.3: Close up of updated fillet and corresponding force-displacement history curve

5.3.2 Energy Study

An energy balance check was performed to predict possible numerical instabilities and to confirm that spurious artificially introduced energy was avoided. The ratio between the artificial strain energy, E_A, which includes energy stored in hourglass resistance and transverse shear in the flexural shell elements, and the internal energy, E_I, were assessed. The result from this assessment was 7.47 %, which was sufficient, Figure 5.4. The kinetic energy, E_K, was negligible when compared to the

internal energy and the external work, E_E. This equals the internal energy, giving a satisfactory energy history for a quasi-static analysis.

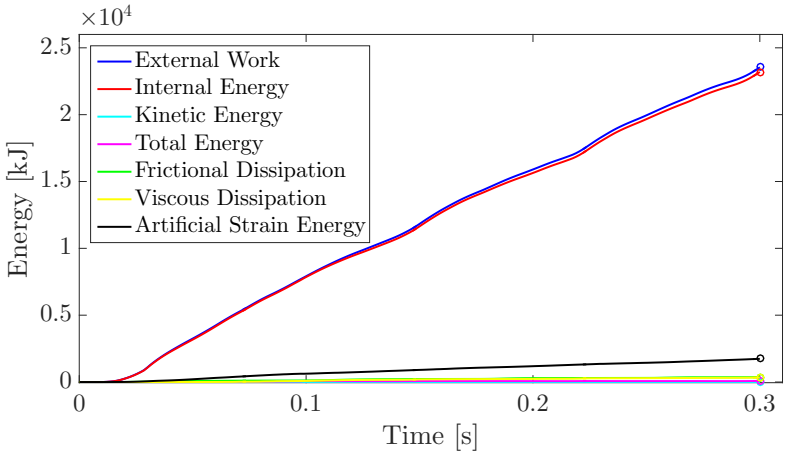

Figure 5.4: Energy history of the axial crushing simulation

5.3.3 Mesh Study

The elements are fundamental in FE formulation. The ductility under membrane loading is directly linked to the mesh-size, and larger elements develop lower strains, thus have a lower Cockroft-Latham parameter, W_C. A study of element size was performed to examine this effect. The component was discretized using element sizes of 2.0, 2.6, 3.0 and 5.0 mm. This assessment found that small changes in element size has a minor effect on the force-displacement curve, and that larger element sizes results in a greater energy absorption capacity, Figure 5.5.

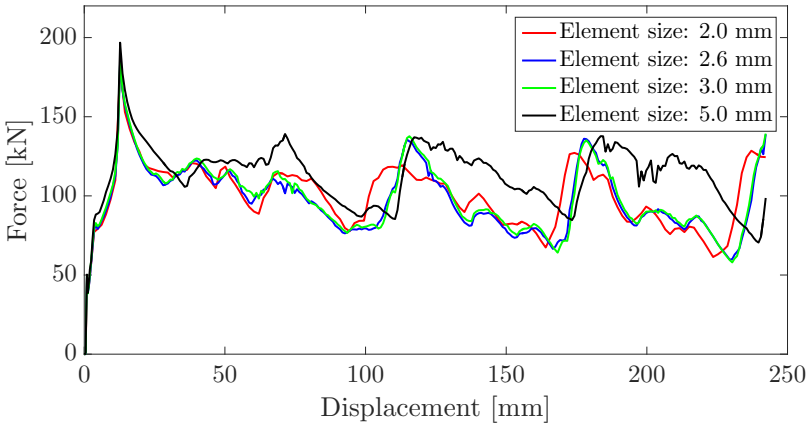

Figure 5.5: Force - displacement history

When the element size was expanded from 2.6 mm to 5.0 mm it resulted in the same folding pattern with similar transition from asymmetric to symmetric folding. Larger folds were also observed, Figure 5.6. Decreasing the element size to 2.0 mm resulted in a shift in the force-displacement curve to the left, and a similar energy absorption capacity were registered. The shift might be explained by violations of the shell elements formulation due to a decreased slenderness. Both material models experienced the same behaviour.

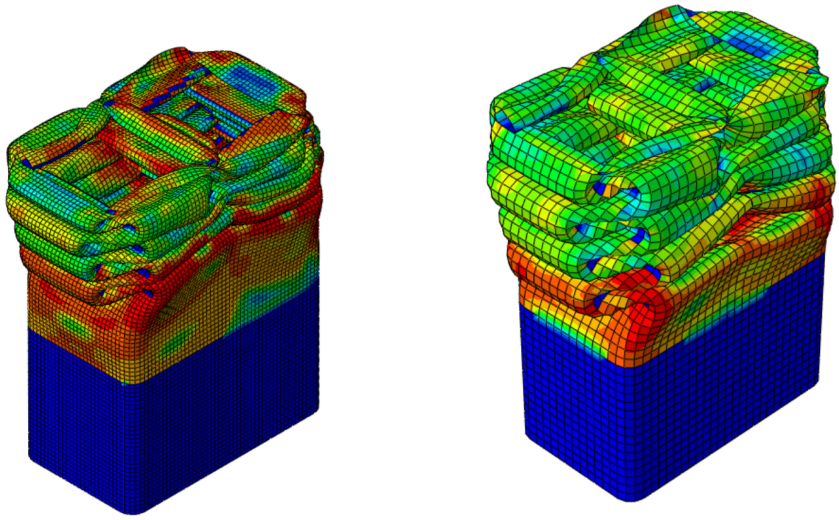

(a) Mesh size of 2.6 mm (b) Mesh size of 5.0 mm

Figure 5.6: Difference in fold volume when utilising different mesh sizes

Additional important features that depends on element size are the computational cost and artificial energy created during simulation. In explicit FE simulation, numerical instabilities are associated with artificially introduced energy, which are directly linked to element size. Reducing element size exponentially increased CPU-time, while the ratio between artificial strain- and total internal energy decreased, Table 5.1.

Table 5.1: CPU-time and relative amount of artificial energy for different mesh sizes

Element size [mm]	Number of elements	CPU-time [s]	$max(E_A/E_I)$ [%]
2.0	53535	425661	7.22
2.6	31540	139999	7.47
3.0	24048	57029	8.92
5.0	8686	8136	12.12

5.4 Experimental Investigation

5.4.1 Test Rig and Setup

The components were investigated experimentally in room temperature with an Instron 5982 test machine with a 250 kN load cell, Figure 5.7. The test components utilised in the quasi-static axial crushing have a total length of 400 mm and the same cross-section as the profiles tested in the stretch bending rig. The thickness in the middle wall and outer walls was measured to be 1.746 mm and 2.565 mm respectively. The top 11 mm was machined into a pyramid-shape to trigger a repeatable folding pattern. The components were clamped at the lower 80 mm between two high-strength steel plates, and two wood blocks were inserted at the clamped end to act as inner clamps. A constant cross-head speed of 10 mm/min was used for a total displacement of 250 mm, ensuring quasi-static conditions. During the test, both the displacement and force at the cross-head were measured at a sampling rate of 10 Hz. The deformed shape of the component was captured by a camera with a frequency of 2 frames per second, i.e. 4 Hz.

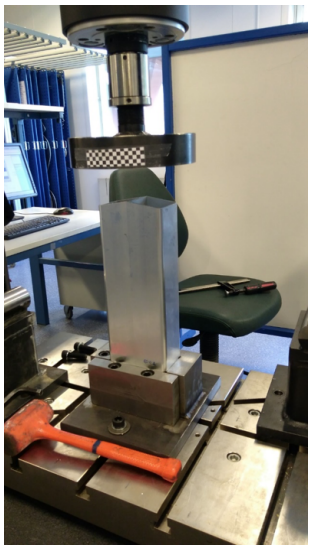

Figure 5.7: Axial crushing test setup

5.4.2 Results

Three quasi-static axial crushing tests of the fibrous microstructure, and five tests of the recrystallised microstructure were conducted, and the force-displacement curves for the fibrous- and recrystallised components were established, Figure 5.8 and Figure 5.9, respectively.

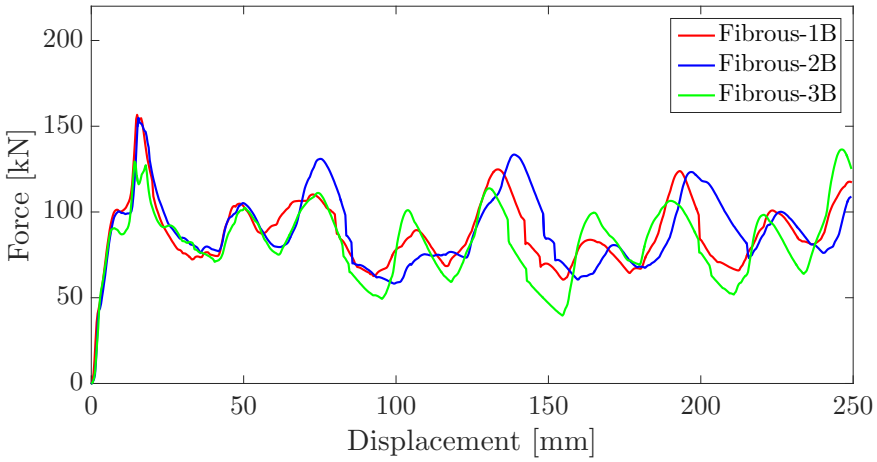

Figure 5.8: Force - displacement history of the fibrous material

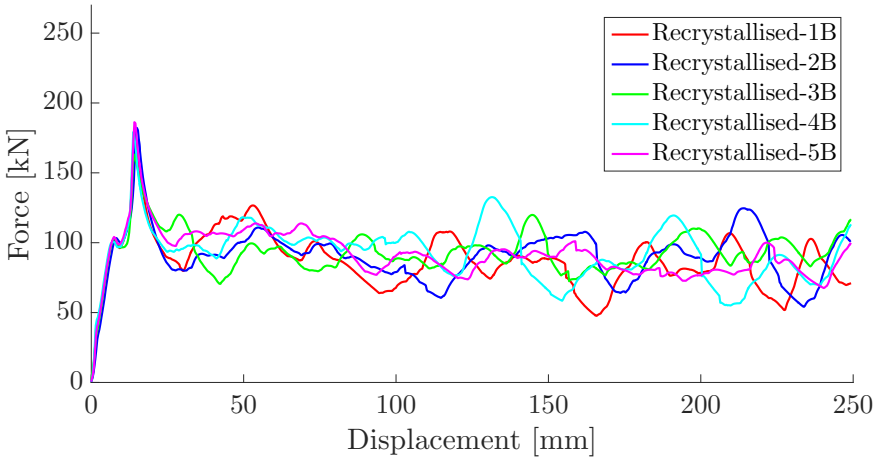

Figure 5.9: Force - displacement history of the recrystallised material

The pyramid shaped trigger created the wanted folding pattern, and each peak on the force-deformation curve corresponds to the completion of a fold, summing up to a total of nine folds. This behaviour was more definite in the fibrous material, where the force-displacement curve displayed a distinct oscillation. Both a symmetric and an asymmetric folding mode were observed. The main difference in the folding modes was caused by the extent of fracture at the inner wall. If it teared from the

outer wall on both sides, a symmetric pattern in the specimen was created, while an asymmetric pattern were observed if only one or none of the sides experienced tearing. The different folding modes were transitional.

For the fibrous material, both test 1B and test 2B started in an asymmetric folding pattern, evolving into a symmetric folding pattern in the second fold, while test 3B experienced only symmetric folding. Test 1B evolved back into an asymmetric folding pattern in the last fold. The different folding modes were observed in test 1B of the fibrous material, together with the middle wall tearing in test 3B of the fibrous material, Figure 5.10. There were fracture observed at the corners in all tests, and test 1B and test 2B experienced fracture through the outer wall at the middle walls location.

For the recrystallised material, all tests started in an asymmetric- before evolving into a symmetric folding pattern. Four of the tests transitioned into a symmetric folding pattern in fold number three, and the components showed less sings of fracture than the fibrous material.

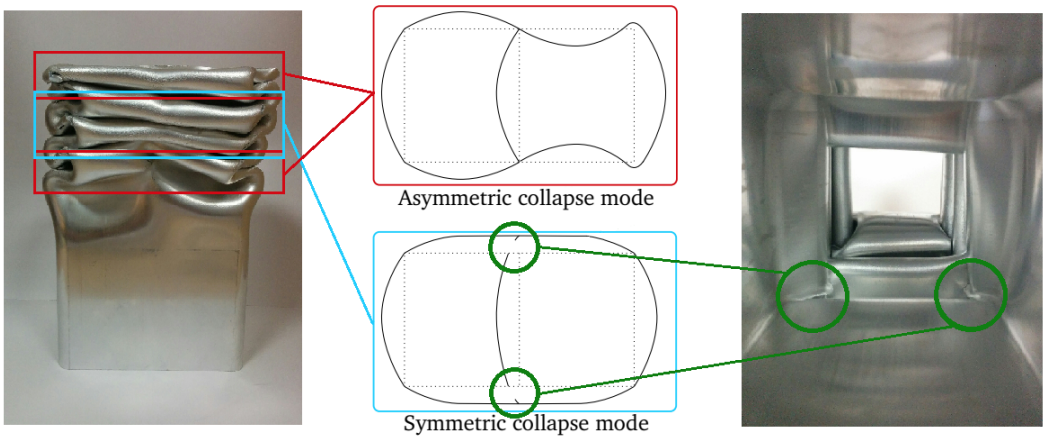

Figure 5.10: Collapse modes in test 1B and tearing of middle wall in test 3B

6 Discussion of Results

The experimental- and numerical results for the quasi-static stretch bending and axial crushing are separately discussed and compared. The numerical models validity and ability to replicate the physical experiments will be reviewed and how different features effects the results considered.

6.1 Stretch Bending

To test the material models ability to replicate failure, three extrusions of an AA6005A-T6 alloy with both a fibrous- and a recrystallised microstructure were performed. The test specimens were loaded 50 kN in tension before the die initiated failure. Examination of the extrusions after testing revealed that all tests experienced the same kind of failure, and the location of failure was corresponding to the intended design. No difference were observed when comparing the fibrous- and recrystallised fractured surface.

6.1.1 Fibrous Microstructure

The FE model was simulated and validated against the experimental tests and a good replication was obtained. The force required to initiate failure in the numerical model was 12.17 kN, which were 1.05, 1.08 and 0.86 kN higher for test 1A, test 2A and test 3A, respectively. Further, the numerical model overestimated the force throughout the simulation. The numerical model experienced some oscillation in the start of the model, which was undesirable and could be a potential error source, Figure 6.1.

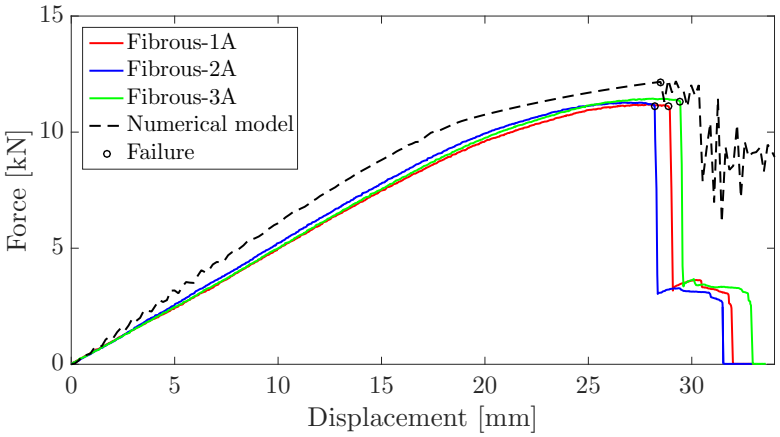

Figure 6.1: Comparison of force-displacement history curves

The numerical model with symmetry plane did not replicate the behaviour of the failure after it first initiated. In the experimental tests, rapid failure of the middle wall was shortly followed by failure in one of the side walls. The side wall experiencing failure fist depended on which way the middle wall buckled. In the numerical model, the pace of failure was gradual, and both the side walls failed simultaneously after the middle wall. This discrepancy after failure is easily seen in the force-displacement curves, and the numerical model did not predict total failure in a sufficient manner. However, when utilising a full scale model, the experimental behaviour was reproduced, Figure 6.2. The crack propagation were also replicated, with a vertical movement towards the trigger. In the numerical model, this was caused by the geometry of the mesh which guides the propagation.

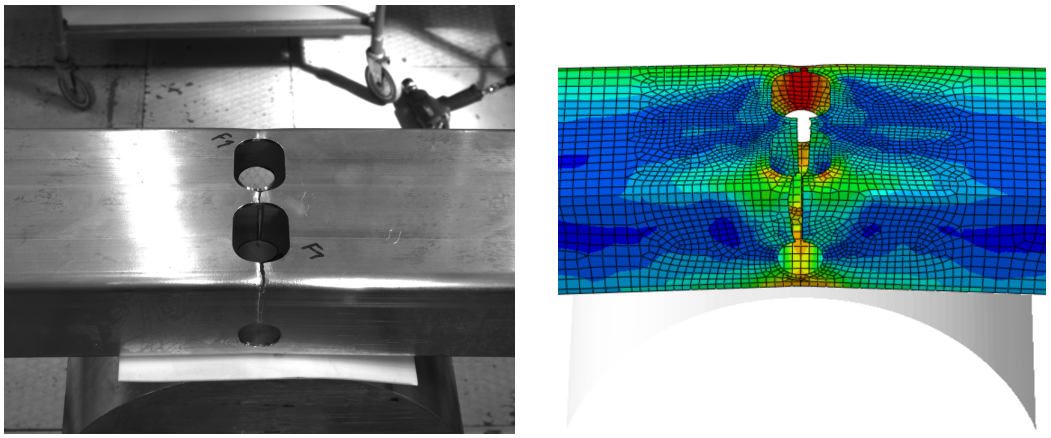

(a) Experiment (Test 1A, fibrous) (b) Full scale model

Figure 6.2: Experimental and full scale model failure similarity

6.1.2 Recrystallised Microstructure

Three experimental tests of the AA6005A-T6 extrusions with recrystallised microstructure were performed and differentiated against the FE model. An accurate representation was achieved, and the force required to initiate failure in the numerical model at 12.32 kN were 0.80, 0.74 and 0.64 kN higher for respectively test 1A, 2A and 3A. The numerical model did not capture the behaviour after failure of the middle wall, and the force-displacement curve oscillated after the failure initiated, Figure 6.1. The recrystallised material model also failed to predict total failure of the profile.

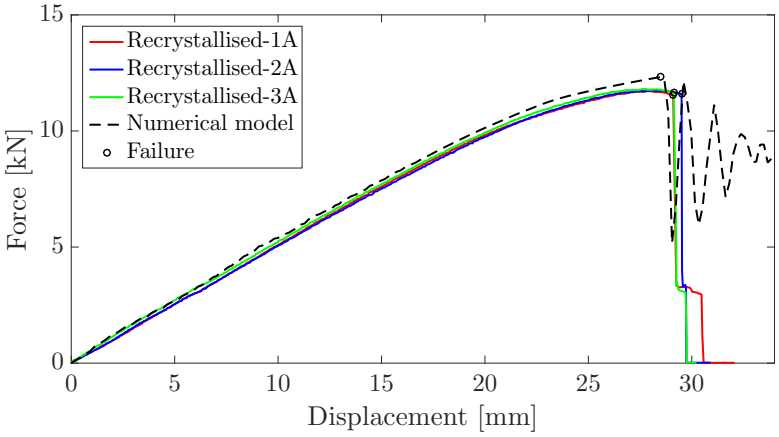

Figure 6.3: Comparison of force-displacement history curves

6.1.3 Comparison

Up to and including the point of failure, a qualitative agreement was achieved by both numerical models, replicating the experimental results in a good fashion, though both models were conservative, Table 6.1. The recrystallised material model replicated the experimental results in both force path and failure value more precisely than the fibrous material model, Figure 6.4. In the component tests, the recrystallised material experienced an average of 3.62 % higher forces than the fibrous material. These results were expected, due to grain strength provided in the recrystallised material. This was also consistent to research done by Si et al. (2005) on material texture [10].

Table 6.1: Die force at failure

	Fibrous	Recrystallised
	Force [kN]	Force [kN]
Test 1A	11.12	11.52
Test 2A	11.09	11.58
Test 3A	11.31	11.68
Numerical	12.17	12.32

None of the material models replicated the force-deformation curve after the failure of the middle wall, neither the fibrous- nor the recrystallised with and without symmetry planes or fillets. A full scale simulation of the recrystallised material model proved to replicate the experimental tests best, as this model experienced the least amount of oscillation. These oscillations were caused by stress wave propagation speed in elements induced by damage, and were expected in the explicit simulations. This could be solved by filtering out the high frequencies, using filters such

as Butterworth. This was however not within the scope of this Thesis, and have therefore not been emphasised.

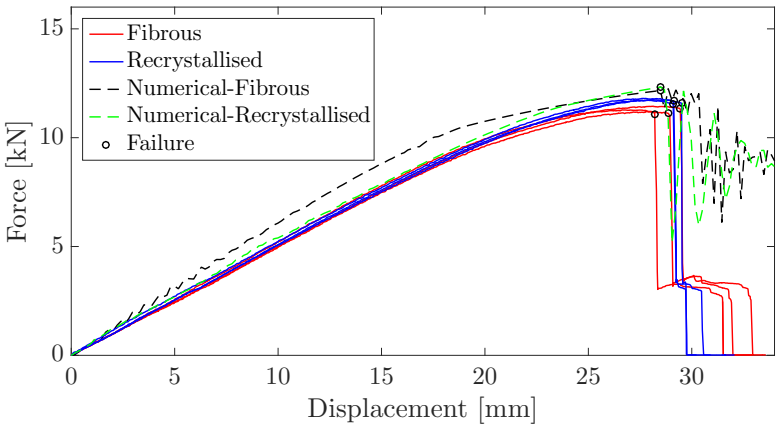

Figure 6.4: Comparison of force-displacement history curves

The use of symmetry planes, and how this effected the result was examined. By simulating the whole extruded profile, the force required to initiate failure decreased when compared to a model with symmetry plane. This reduction may be caused by the definition of the damage criterion. The damage factor needs to equal unity in all five integration points to erode an element. However, the symmetry plane is created where failure is expected, and to remove the element closest to the plane, an imaginary element on the opposite side of the plane needs to erode too, thus the model needs to erode two elements to initiate failure. Disregarding the symmetry plane corresponded to a strength decrease of 3.42 % and 2.47 % on respectively the fibrous- and recrystallised material model, achieving a better replication of the experimental tests.

Further, a study of the fillets effect on bearing capacity of the model was executed. The neglecting of the fillets in the introductory model resulted in a loss of bearing capacity of the middle wall, and thus the failure occurred at lower force. Hence, the compliance of the numerical model and experimental tests should differ to a greater extent. Using a fillet size of 3.7 mm, the strength of the model increased as much as 5.4 % and 5.0 % for the fibrous- and the recrystallised material model, respectively.

Discrepancies in the force-deformation curves could be explained by several effects. First, the material characteristics were extruded from tensile tests of the top outer wall, while the middle wall experienced failure first. The material experienced anisotropy, although the model was assumed to be isotropic. In addition, simulations are often stiffer than the experiments, as the material contains impurities which are not included in the numerical model. Fracture is defined by when an

element is eroded in the numerical model, and a small error could be caused by the number of time steps. Lastly, the stretch bending machine was measured to be $2-3$ cm irregular, and the profiled were therefore mounted with a slight angle. However, this irregularity were not large enough to affect the impact area of the die.

6.1.4 DIC analysis

Large inconsistencies were found between the numerical model and the experimental tests with regard to displacement in the horizontal actuators, Table 6.2. This inconsistency were inspected employing a DIC analysis in the software eCorr on the chessboard stickers that were applied on the profile at the grip section, Figure 6.5. Only test 1A for both microstructures were analysed, as no noticeable bearing deformations were observed in the grip area of the tests.

(a) Left side (b) Right side

Figure 6.5: Chessboard stickers at profile and grip section

There were many parts involved in the test rig, which can have relative displacements to each other. The DIC analysis found the total horizontal displacement of test 1A to be 1.68 and 1.74 mm, which was 0.79 and 1.03 mm more than the numerical model for respectively the fibrous- and recrystallised microstructure, Table 6.2. Still, this infringement was not considered important, as the error is small and horizontal forces were replicated.

Table 6.2: Total horizontal displacement before failure

	Fibrous	Recrystallised
Test-1A	6.77 mm	7.53 mm
Test-2A	7.45 mm	5.48 mm
Test-3A	4.89 mm	5.55 mm
Numerical	0.89 mm	0.71 mm
DIC (Test-1A)	1.68 mm	1.74 mm

6.2 Axial Crushing Test

Quasi-static axial crushing tests were investigated to check the material models ability to replicate severe deformation and complex stress states. The crushing test resulted in a progressive folding pattern, consistent with previous work done by Langseth and Hopperstad (1997) on thin-walled aluminium extrusions [36]. The pyramid- shaped machined component created prior to testing, created the wanted local buckling pattern initiated at the top of the component. Further displacement led to change in the folding mechanism, and both symmetric and asymmetric folding were observed. Examination of the component after testing revealed clear signs of fracture along the edges of the specimen. The location of the fractures were consistent with research done by Gu et al. (2012). Their research also stated that the fractures was caused by high stress triaxiality and plastic straining [37].

6.2.1 Fibrous Microstructure

The FE model was validated against the quasi-static experimental tests and an adequate agreement was acquired. For the fibrous material the initial peak of the numerical model was found to be 185.6 kN, which was 28.9 kN higher than test 1B and 30.7 kN higher for test 2B. Both these tests experienced asymmetric folding and severe fracture in the first fold. In test 3B, the initial peak of the numerical model was 56.2 kN higher due to symmetrical folding from the start. The numerical model captured fracture accurately, with cracks at the corners, and fracture along both sides of the middle wall. However, it did not recreate the oscillating force amplitude, but the same number of peaks were replicated, Figure 6.6.

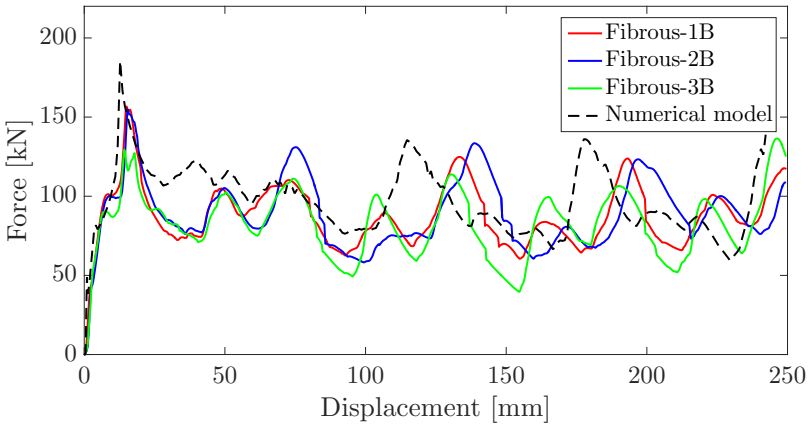

Figure 6.6: Comparison of force-displacement history curves

The folding pattern evolved from an asymmetric- to a symmetric pattern in the numerical model similar to experimental results. In Figure 6.7, three steps of the deformation at 10 mm, 125 mm and 250 mm displacement is shown, both for the physical crushing test and the numerical simulation, while Figure 6.7d shows the inconsistency in the asymmetric fold, located in the top left corner. This transition happened in fold three in the numerical simulation, and not in fold one, as test 1B and test 2B. This discrepancy is caused by the material model not describing the tearing of middle wall at the start of the crushing in a satisfactory way.

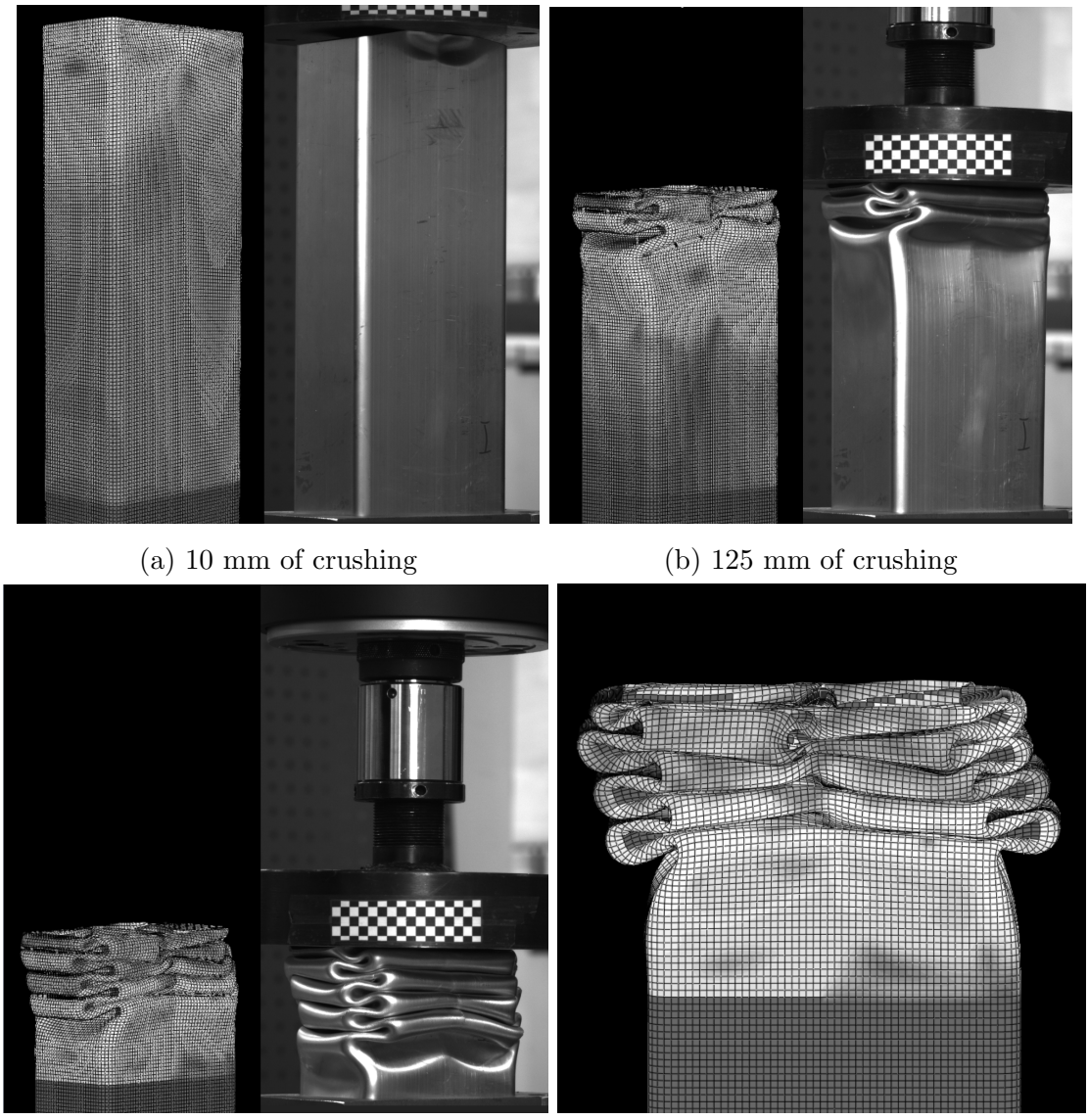

(a) 10 mm of crushing

(b) 125 mm of crushing

(c) 250 mm of crushing

(d) Folding pattern

Figure 6.7: Side-by-side crush test, Abaqus simulation, and final folding pattern

The average crushing force, F_{avg}, was investigated using equation 6.1 to attain greater perception of the tests, i.e. the force was found by integrating the force-

displacement over the crushing length before dividing by the current displacement, δ. Due to the transitional behaviour of the folding, together with different sections experiencing fracture, an average crushing force gave a more comprehensible picture of the numerical models ability to replicate the physical experiments.

$$F_{avg}(\delta) = \frac{\int_0^\delta F(\delta)d\delta}{\delta} \tag{6.1}$$

The current mean crushing force for the three tests and the simulated numerical model was plotted as a function of crushing length, Figure 6.8. The numerical model overestimated the force from the start to the end of the simulation, indicating that the numerical model was stiffer than the experimental tests. After the initial peak, the numerical model had an error between 10- and 25 kN throughout the simulation. Another aspect illuminated from Figure 6.8 is the fact that symmetric folding has a lower energy absorption per unit length. This was studied further with use of equation 6.2:

$$E_a = \int_0^{\delta_f} F d\delta \tag{6.2}$$

were E_a is the absorbed energy, δ is displacement, δ_f is the final displacement and F is the applied force. The mean crushing force and absorbed energy after 250 mm of displacement can be seen in Table 6.3. This shows that test 3B, which only experiences symmetric folding has a significantly lower mean crushing force and absorbs 6.3% and 7.7% less energy than respectively test 1B and test 2B, and as much as 16.4% less than the numerical model.

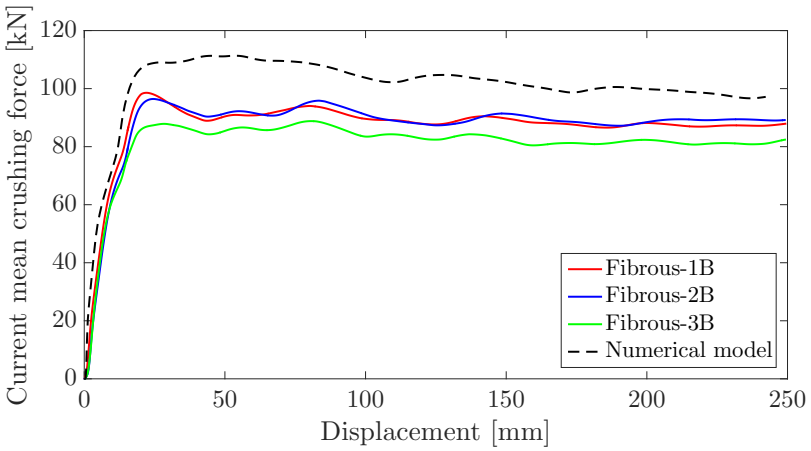

Figure 6.8: Current mean crushing force - displacement history

Table 6.3: Current mean crushing force and absorbed energy after 250 mm of crushing

Test	F_{avg} [kN]	E_a [kJ]
1B	87.93	21.77
2B	89.19	22.09
3B	82.47	20.39
Numerical	97.16	23.53

An in-depth inspection of the numerical model was done to inspect that fracture were described correctly in the complex stress state the crushing induces, and to check what condition the elements experiencing failure were subjected to. Contour plots of the deformation mode indicator, Ω, and damage variable, D were established, Figure 6.9. The folds high degree of bending, as well as the more complicated state in the corners are illustrated in, Figure 6.9a. The contour plot of the damage variable showed that the numerical model experienced some degree of fracture at the corners and tearing at the middle wall, replicating the physical tests, Figure 6.9b.

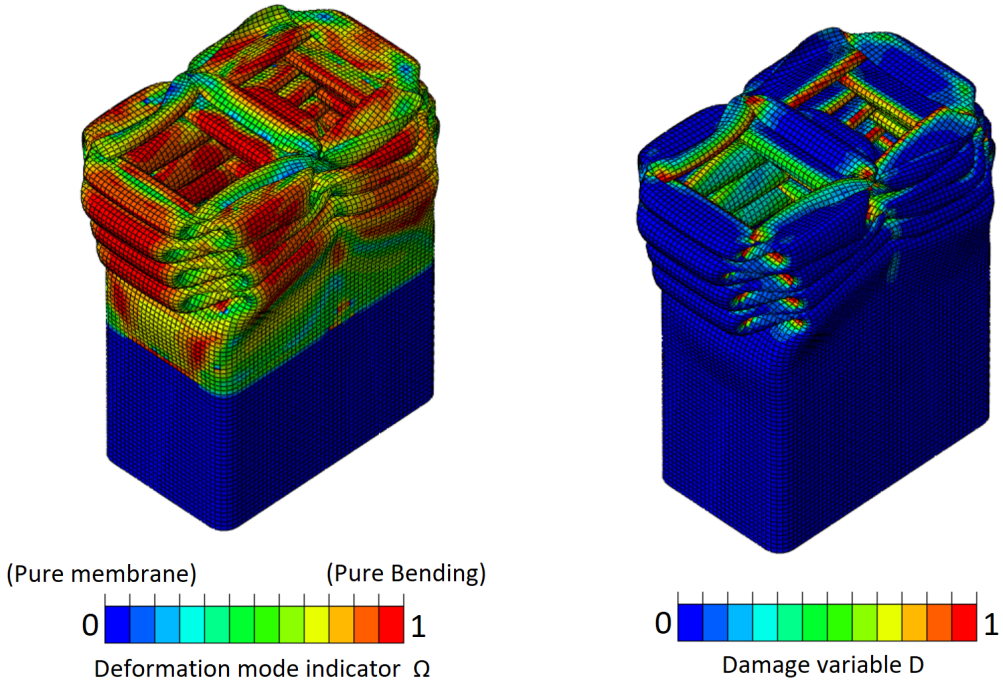

(a) Deformation mode indicator

(b) Damage variable

Figure 6.9: Contour plots of deformation mode indicator and damage variable of the numerical model

6.2.2 Recrystallised Microstructure

Five experimental tests of the recrystallised alloy were performed and differentiated against the FE model with the recrystallised material model. A good agreement was achieved, and the numerical model replicated the experimental tests. The capture of the initial peak were also acceptable, where four of the five tests were within a range of 17.0 kN from the numerical value of 196.2 kN. Test 3B had an initial peak of 163.1 kN, experiencing a symmetric folding pattern at the initial fold. Fracture was captured with cracks at corners and continuous tearing of the middle wall. The force-displacement curve, Figure 6.10 was also reproduced in a favourable manner with good replication of the oscillating force amplitudes. The folding pattern transitioned from an asymmetric to a symmetric folding pattern, where four of the five tests and the numerical model experienced this alteration in fold number three.

The average crushing force and absorbed energy were calculated using equation 6.1 and equation 6.2. The current mean crushing force for the five experimental tests and simulated numerical model can be seen in Figure 6.11. After the initial peak, the numerical value was estimated to be between 5 and 15 kN to high throughout the simulation. The absorbed energy of the numerical model differed between 10.73 % from the experimental test 1B to 4.75 % from experimental test 3B.

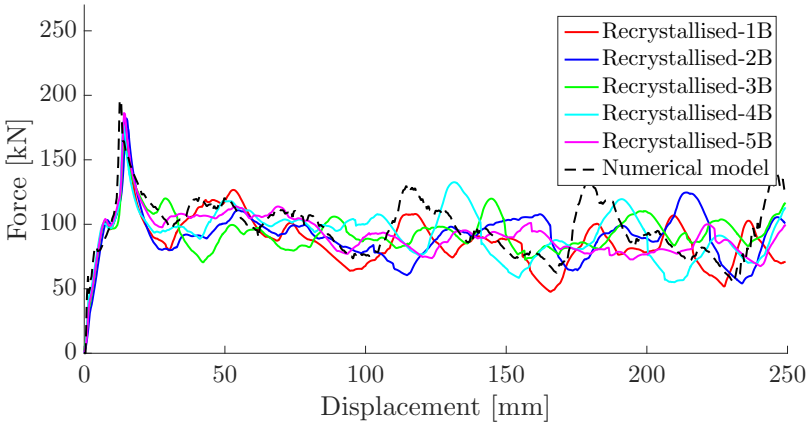

Figure 6.10: Comparison of force-displacement history curves

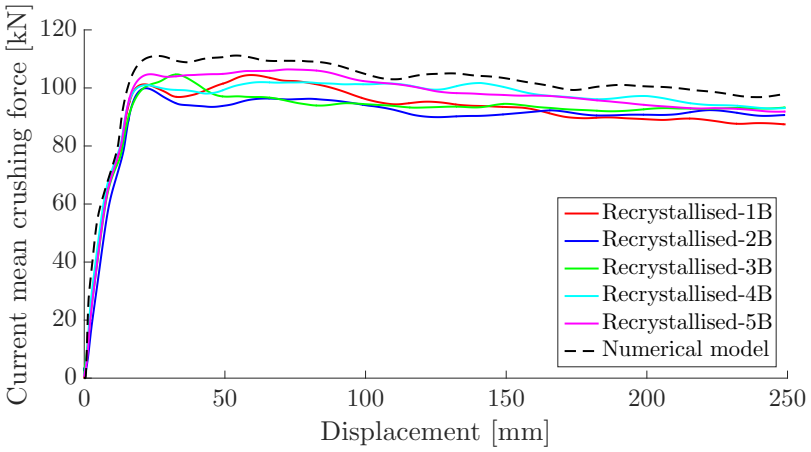

Figure 6.11: Comparison of fibrous- and recrystallised microstructure

A comparison between the mean force and absorbed energy for the two individual microstructures after 250 mm of displacement was assessed, Table 6.4. The recrystallised microstructure required on average 4.74 kN more force and absorbed 1.34 kJ more energy when deforming in a folding pattern.

Table 6.4: Comparison of mean force and absorbed energy after 250 mm of displacement

Test	F_{avg} [kN]	E_a [kJ]
1B	87.44	21.80
2B	90.67	22.59
3B	93.28	23.26
4B	93.10	23.21
5B	91.86	22.90
Numerical	97.92	24.42

6.2.3 Comparison

When comparing the fibrous- and recrystallised material model with regard to the axial crushing test, both the force displacement curve, Figure 6.12a and the current mean crushing force- displacement curve, Figure 6.12 were assessed. The number of peaks were identical to the fibrous alloy, and the components experienced both symmetric- and asymmetric buckling patterns. a smaller extent of fractures were identified at the corners on the recrystallised, and the numerical model of the recrystallised alloy recreated the experimental tests more precisely than the fibrous

alloy. It was concluded from the tests that the recrystallised alloy buckled in the same manner as the alloy with fibrous microstructure. The material model for the recrystallised microstructure gave a better agreement in the current mean crushing force - displacement curve.

The force - displacement curve are shown in Figure 6.12a and current mean crushing force- displacement curves are illustrated in Figure 6.12a. A summary of the current mean crushing force and absorbed energy after 250 mm of deformation was established to get a full overview over the results, Table 6.5.

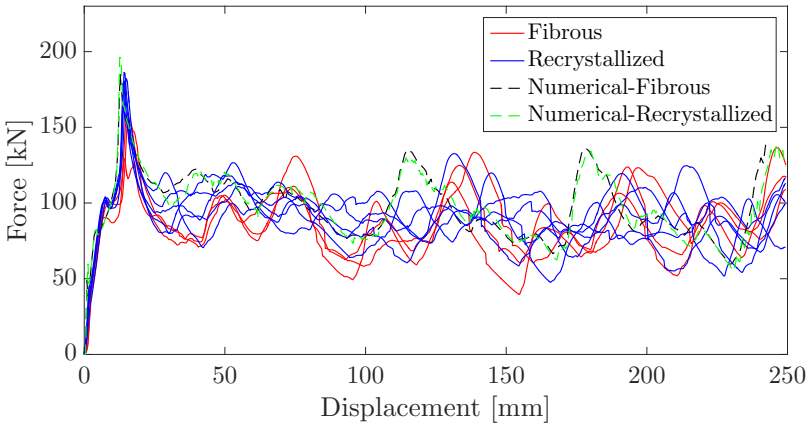

(a) Force - displacement curves

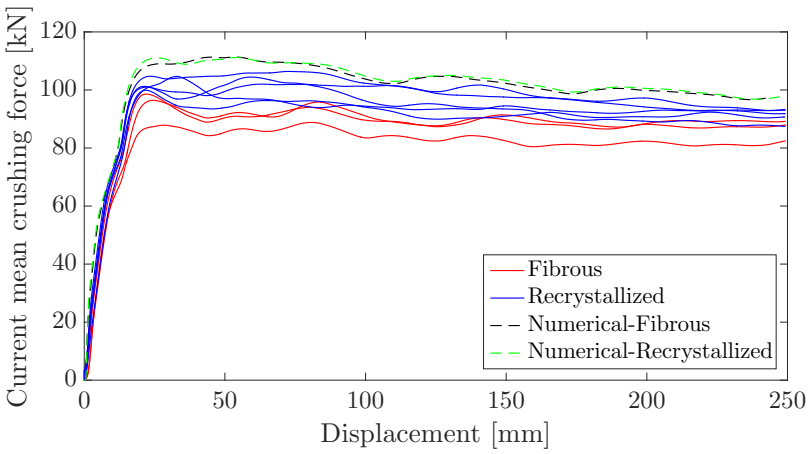

(b) Current mean crushing force - displacement curves

Figure 6.12: Comparison of fibrous- and recrystallised microstructure

Table 6.5: Comparison of mean force and absorbed energy after 250 mm of deformation

	Fibrous		Recrystallised	
Test	F_{avg} [kN]	E_a [kJ]	F_{avg} [kN]	E_a [kJ]
1B	87.93	21.77	87.44	21.80
2B	89.19	22.09	90.67	22.59
3B	82.47	20.39	93.28	23.26
4B			93.10	23.21
5B			91.86	22.90
Numerical	100.86	24.91	97.92	24.42

7 Conclusions and Proposals for Future Work

The failure of AA6005A-T6 aluminium extrusions with both a fibrous- and a recrystallised microstructure were evaluated and validated using a regularisation strategy for shell elements where the ductility was determined by the bending-to-membrane load ratio in Abaqus/Explicit. Both stretch bending- and axial crushing tests were conducted in order to assess the models compatibility under different sets of loading. Triggers were designed at the middle of the extrusions in order to obtain the wanted failure in the stretch bending laboratory experiments. Further, the top of the specimens subjected to axial crushing were machined into a pyramid shape, initiating the wanted progressive folding.

7.1 Conclusions

- From the material tests it were discovered that the material investigated, aluminium alloy AA6005A with temper T6, have a greater degree of anisotropy than anticipated. The alloy with the recrystallised microstructure exhibited the most.
- Small discrepancies were detected for the material properties in the top-, side- and middle wall for both microstructures.
- The constitutive model was easily implemented in a FE model, utilising only standard tensile tests and a DIC software.
- The regularisation scheme accurately predicted failure in the stretch bending test, proving thinning strain rate as a sufficient way to assess the deformation mode of shell elements in numerical simulations. The force required to initiate fracture in the stretch bending experiment was overestimated with an average error of 8.2 % and 5.9 % on the fibrous- and recrystallised alloy, respectively.
- The constitutive model reliably replicated the axial crushing test behaviour, validating the regularisation scheme for a complex loading involving strain localisation and considerably bending. The mean crushing force in the axial crushing experiment was overestimated with an average error of 14.2 % and 6.8 % on the fibrous- and recrystallised alloy, respectively.
- Including the fillet connecting the outer- and middle wall increased the bearing capacity of the numerical model.
- Using symmetry plane increased the force required to initiate failure.

7.2 Future Work

In this master Thesis, an isotropic Hershey-Hosford yield criterion was utilised when approaching the material model. In the material testing it was detected that the material exhibited some degree of anisotropy, therefore applying an anisotropic yield criterion, such as Hills- or Barlats yield criterion could improve results. A more advanced fracture criterion could be employed in the numerical model to improve the fracture initiation. The material model was based on one representative test for both the fibrous- and the recrystallised material. This could cause discrepancies with the experimental results, as the material had different characteristics in the outer- and middle wall.

The material behaviour and underlying causes could be further investigated with more experiments to study replication patterns and exceptions, thus finding the reason why the recrystallised material replicates the experiments in a more desirable manner. A more advanced parameter study could be performed, gaining a better insight in how the model was affected by altering different features. A study on fracture in larger structures and with greater strain rate could be conducted, evaluating the damage regularisation models ability to predict failure in e.g. boat crash on a bridge.

Design of safe and lightweight structures with aluminium alloys will give great strength-to-weight ratio benefits. Establishing industry standards including design requirements and guidelines for numerical modelling and analyses of crash deformation modes is recommended. This will reduce development time and thus design cost.

References

[1] Odd Sture Hopperstad Tore Børvik. *Lecture Notes, Material Mechanics, Part 1.* Structural Impact Laboratory, 2017.

[2] T. L. Anderson. *Fracture Mechanics: Fundamentals and Applications*, volume 3. Taylor & Francis Group, 2005.

[3] J.D. Embury M.F. Ashby D. Tierlinck, F. Zok. *Fracture mechanism maps in stress space*, volume 36. Acta Metallurgica, 1988.

[4] K.M. Mathisen. Lecture notes - finite element methods in strength analysis. Draft, Version 2015a.

[5] Odd S. Hopperstad Arild H. Clausen and Magnus Langseth. Stretch bending rig. experimental set-up. Technical report, NTNU, 1999.

[6] Eurocode 9: Design of aluminium structures, 1999.

[7] Understanding the alloys of aluminum. http://www.alcotec.com/us/en/education/knowledge.cfm Accessed: 2018-02-27.

[8] N. Hansen and B. Bay. Initial stages of recrystallization in aluminium containing both large and small particles. Technical report, Danish Academy of Mechanical Engineering, 1980.

[9] Rajat K. Roy. Recrystallization behavior of commercial purity aluminium alloys. Technical report, Indian Institute of Technology, 2014.

[10] O. Engler S. Li and P. V. Houtte. Plastic anisotropy and texture evolution during tensile testing of extruded aluminium profiles. Technical report, 2005.

[11] K. Ueno and M. Ueda. Buckling behaviour in stretch bending of channels. Technical report, University of Birmingham, 1985.

[12] T. Welo F. Paulsen. Application of numerical simulations in the bending of aluminium-alloy profiles. Technical report, NTNU, 1996.

[13] O.S. Hopperstad A.H. Clausen and M. Langseth. Sensitivity of model parameters in stretch bending of aluminium extrusions. Technical report, NTNU, 2000.

[14] O.S. Hopperstad A.H. Clausen and M. Langseth. Stretch bending of aluminium extrusions: Effect of tensile sequence. Technical report, NTNU, 1999.

[15] L. Yhang M. Scharrer and E.D. Egge. Collision calculation in naval design systems. Technical report, Germanischer Lloyd, Hamburg, 2002.

[16] H. Endo Y. Yamada and P. Terndrup-Pedersen. *Numerical study on the effect of buffer bow structure in ship-ship collision.* International Society of Offshore and Polar Engineers, 2005.

[17] H. Remes M. Körgesaar and J. Romanoff. Size dependent responce of large shell elements under in-plane tensile loading. Technical report, Aalto University, Finland, 2014.

[18] A. Haufe F.X.C. Andrade, M. Feucht and F. Neukamm. An incremental stress state dependent damage model for ductile failure prediction. Technical report, Dynamore GmbH, Stuttgart, 2016.

[19] T.B. Stoughton and J.W. Yoon. A new approach for failure criterion for sheet metals. Technical report, Swinburne University of Technology, 2011.

[20] K. Pack and D. Mohr. *Engineering Fracture Mechanics.* Elsevier, 2017.

[21] How and why alloying elements are added to aluminum. http://www.alcotec.com/us/en/education/knowledge/techknowledge/understanding-the-alloys-of-aluminum.cfm. Accessed: 2018-02-21.

[22] Aging - metallurgical processes. https://www.azom.com/article.aspx?ArticleID=9547. Accessed: 2018-03-10.

[23] Abaqus/cae user's guide. http://abaqus.software.polimi.it/v6.14/books/usi/default.htm. Accessed: 2018-06-06.

[24] O. S. Hopperstad Y. Chen, A. H. Clausen and M. Langseth. Stress–strain behaviour of aluminium alloys at a wide range of strain rates. Technical report, NTNU, 2009.

[25] O.S. Hopperstad O.-G. Lademo and M. Langseth. An evaluation of yield criteria and flow rules for aluminium alloys. Technical report, NTNU, 1998.

[26] Odd Sture Hopperstad and Tore Børvik. Lecture notes - modelling of plasticity and failure with explicit finite element methods. Draft, Version 2017.

[27] Wilbur R. Varney Donald S. Clark. *Physical Metallurgy for Engineers.* Pitman Publishing Corp, 1962.

[28] J.W. Yoon M.E. Karabin J.C. Brem F. Barlat, H. Aretz and R.E. Dick. Linear transfomation-based anisotropic yield functions. *International Journal of Plasticity*, 21:1009 – 1039, 2005.

[29] William D. Callister jr and David G. Rethwisch. *Material Science and Engineering.* Wiley, 2015.

[30] Egil Fagerholt. Lecture notes - digital image correlation, September 2017.

[31] J.W. Ringsberg P. Högström and E. Johnson. An experimental and numerical study of the effects of length scale and strain state on the necking and fracture behaviours in sheet metals. Technical report, Technical Research Institute of Sweden, 2009.

[32] O.S. Hopperstad D. Morin, B.L. Kaarstad. B. Skajaa and M. Langseth. Testing and modelling of stiffened aluminium panels subjected to quasi-static and low-velocity impact loading. Technical report, NTNU, 2017.

[33] A. Benallal M. Fourmeau, T. Børvik and O.S. Hopperstad. Anisotropic failure modes of high-strengt aluminium alloy under various stress states. Technical report, NTNU, 2013.

[34] M.E. Plesha R.D. Cook, D.S. Malkus and R.J. Witt. *Concepts and Application of Finite Element Analysis*. University of Wisconsin - Madison, 4th edition, 2002.

[35] Friction and friction coefficients. http://structx.com/Material_Properties_005a.html. Accessed: 03-03-18.

[36] Hopperstad O.S. Langseth M. Local buckling of square thin-walled aluminium extrusions. *Thin-walled structures*, 27(1):117–126, 1997.

[37] Zhou Q. Gu G., Xia Y. On the fracture possibility of thin-walled tubes under axial crushing. *Thin-Walled Strucutres*, 55:85–95, 2012.

A Appendix - Exact Measurements

In this Appendix the pre- and post-mortem measurements of the tensile tests are presented. The thickness and the width of the tests were measured five separate places, and an average of this was used when calculating the R-values. For the post-mortem measurements, only places not affected by the neck was used.

A.1 Recrystallised

Table A.1: Description of abbreviations and associated tests

Specimen name	Location	Angle
RT90	Top	90
RT00	Top	0
RS00	Side	0
RS90	Side	90
RM00	Middle	0
RM90	Middle	90
RTC90	Top	90
RTC45	Top	45
RTC00	Top	0
RMC00	Middle	0
RMC45	Middle	45
RMC90	Middle	90

Table A.2: Pre-mortem measurements of tensile test of the recrystallised AA6005-T6 alloy

Specimen	ta	tb	tc	td	te	T	wa	wb	wc	wd	we	W
RT90-1	2.589	2.588	2.592	2.596	2.590	**2.591**	2.997	2.987	2.989	2.988	2.988	**2.990**
RT90-2	2.588	2.586	2.586	2.587	2.585	**2.586**	2.9945	2.988	2.998	2.989	2.993	**2.992**
RT90-3	2.591	2.587	2.584	2.585	2.587	**2.587**	2.992	2.996	2.992	2.995	2.993	**2.994**
RT00-1	2.588	2.590	2.591	2.591	2.591	**2.590**	2.999	3.000	3.000	2.995	2.994	**2.998**
RT00-2	2.592	2.589	2.589	2.591	2.593	**2.591**	2.988	2.996	2.996	2.988	2.999	**2.993**
RT00-3	2.586	2.587	2.592	2.594	2.590	**2.590**	2.988	2.989	2.990	2.986	2.987	**2.988**
RS00-1	2.537	2.541	2.541	2.549	2.538	**2.541**	2.992	2.997	2.995	2.995	2.997	**2.995**
RS00-2	2.538	2.538	2.538	2.540	2.539	**2.539**	2.996	2.999	2.987	2.997	2.998	**2.995**
RS00-3	2.541	2.546	2.548	2.543	2.542	**2.544**	2.995	2.998	2.998	3.000	2.992	**2.997**
RS90-1	2.546	2.546	2.540	2.541	2.542	**2.543**	2.997	2.998	2.995	2.997	3.000	**2.997**
RS90-2	2.541	2.542	2.542	2.546	2.548	**2.544**	2.982	2.981	2.977	2.982	2.988	**2.997**
RS90-3	2.550	2.551	2.548	2.548	2.548	**2.549**	2.997	3.000	3.000	2.999	2.998	**2.999**
RM00-1	1.714	1.710	1.711	1.711	1.712	**1.712**	2.982	2.981	2.977	2.982	2.988	**2.987**
RM00-2	1.712	1.711	1.712	1.711	1.711	**1.711**	2.989	2.987	2.983	2.983	2.991	**2.987**
RM00-3	1.716	1.717	1.715	1.714	1.709	**1.714**	2.987	2.978	2.981	2.984	2.982	**2.982**
RM90-1	1.705	1.700	1.711	1.709	1.711	**1.707**	2.976	2.981	2.983	2.984	2.977	**2.980**
RM90-2	1.703	1.702	1.711	1.709	1.712	**1.707**	2.968	2.975	2.974	2.975	2.972	**2.973**
RM90-3	1.705	1.700	1.714	1.709	1.712	**1.708**	2.976	2.979	2.971	2.978	2.977	**2.976**
RTC90-1	2.570	2.571	2.573	2.581	2.581	**2.575**	2.998	2.996	2.995	2.996	2.995	**2.996**
RTC90-2	2.568	2.569	2.574	2.583	2.581	**2.575**	2.994	2.999	2.995	2.990	2.999	**2.995**
RTC90-3	2.569	2.569	2.574	2.579	2.586	**2.575**	2.997	2.994	2.996	2.991	2.998	**2.995**
RTC45-1	2.574	2.570	2.576	2.579	2.581	**2.576**	2.997	2.996	2.997	2.997	2.996	**2.997**
RTC45-2	2.579	2.573	2.576	2.580	2.580	**2.578**	2.998	2.998	3.001	2.999	3.006	**3.000**
RTC45-3	2.568	2.572	2.575	2.584	2.583	**2.576**	2.998	2.992	2.994	2.994	2.996	**2.995**
RTC00-1	2.585	2.582	2.579	2.581	2.584	**2.582**	2.994	2.993	2.995	2.997	2.996	**2.995**
RTC00-2	2.574	2.576	2.576	2.574	2.575	**2.575**	2.991	2.989	2.989	2.995	2.986	**2.990**
RTC00-3	2.580	2.574	2.574	2.578	2.578	**2.577**	2.986	2.994	2.993	2.996	2.998	**2.993**
RMC00-1	1.753	1.752	1.753	1.752	1.757	**1.753**	2.989	2.994	2.997	2.990	2.995	**2.993**
RMC00-2	1.758	1.755	1.752	1.758	1.759	**1.756**	2.998	2.995	2.997	2.997	2.998	**2.997**
RMC00-3	1.751	1.751	1.750	1.751	1.751	**1.751**	2.992	2.996	2.990	2.989	2.991	**2.992**
RMC45-1	1.744	1.745	1.751	1.755	1.744	**1.748**	2.987	2.997	2.991	2.990	2.995	**2.992**
RMC45-2	1.752	1.743	1.749	1.752	1.745	**1.748**	2.992	2.995	2.991	2.990	2.993	**2.992**
RMC45-3	1.745	1.745	1.746	1.746	1.744	**1.745**	2.996	2.995	2.995	2.989	2.995	**2.994**
RMC90-1	1.727	1.737	1.744	1.744	1.743	**1.739**	2.993	2.985	2.994	2.994	2.989	**2.991**
RMC90-2	1.733	1.741	1.747	1.749	1.746	**1.743**	2.993	2.991	2.993	2.987	2.991	**2.991**
RMC90-3	1.733	1.743	1.750	1.747	1.745	**1.744**	2.987	2.987	2.984	2.981	2.987	**2.985**

Table A.3: Post-mortem measurements of tensile test of the recrystallised AA6005-T6 alloy

Specimen	ta	tb	tc	td	te	T	wa	wb	wc	wd	we	W
RT90-1	2.563	2.523	2.559	–	–	**2.548**	2.880	2.776	2.889	–	–	**2.848**
RT90-2	2.529	2.520	2.552	–	–	**2.534**	2.824	2.988	2.879	–	–	**2.831**
RT90-3	2.530	2.509	2.560	–	–	**2.533**	2.793	2.777	2.892	–	–	**2.821**
RT00-1	2.494	–	–	2.443	2.470	**2.469**	2.950	–	–	2.899	2.935	**2.928**
RT00-2	2.483	–	–	–	2.465	**2.474**	2.943	–	–	–	2.929	**2.936**
RT00-3	2.483	–	–	2.436	2.483	**2.467**	2.938	–	–	2.898	2.933	**2.923**
RS00-1	2.444	2.406	–	–	–	**2.425**	2.961	2.924	–	–	–	**2.943**
RS00-2	2.457	–	–	–	2.436	**2.447**	2.949	–	–	–	2.930	**2.940**
RS00-3	2.433	2.408	–	–	2.433	**2.425**	2.946	2.918	–	–	2.937	**2.934**
RS90-1	2.505	2.496	2.510	–	–	**2.504**	2.887	2.851	2.900	–	–	**2.879**
RS90-2	2.502	2.502	2.508	–	–	**2.504**	2.864	2.867	2.879	–	–	**2.870**
RS90-3	2.512	2.503	2.513	–	–	**2.509**	2.888	2.854	2.900	–	–	**2.881**
RM00-1	1.635	–	–	1.622	1.627	**1.628**	2.938	–	–	2.893	2.920	**2.917**
RM00-2	1.634	1.625	1.628	–	–	**1.629**	2.929	2.913	2.923	–	–	**2.922**
RM00-3	1.643	1.628	1.624	–	–	**1.632**	2.911	2.888	2.888	–	–	**2.896**
RM90-1	–	–	1.702	1.689	1.699	**1.697**	–	–	2.917	2.851	2.869	**2.879**
RM90-2	–	–	1.709	1.695	1.682	**1.695**	–	–	2.923	2.883	2.833	**2.880**
RM90-3	–	–	1.706	1.694	1.682	**1.694**	–	–	2.920	2.888	2.880	**2.896**
RTC90-1	2.532	–	–	–	2.551	**2.542**	2.915	–	–	–	2.901	**2.908**
RTC90-2	2.534	–	–	–	2.558	**2.546**	2.906	–	–	–	2.912	**2.909**
RTC90-3	–	–	–	2.531	2.549	**2.540**	–	–	–	2.841	2.900	**2.871**
RTC45-1	–	–	–	2.454	2.493	**2.474**	–	–	–	2.978	2.983	**2.981**
RTC45-2	–	–	–	2.463	2.501	**2.482**	–	–	–	2.977	2.982	**2.980**
RTC45-3	–	–	–	2.449	2.495	**2.472**	–	–	–	2.978	2.984	**2.981**
RTC00-1	2.474	–	–	–	2.469	**2.472**	2.941	–	–	–	2.906	**2.924**
RTC00-2	2.477	2.441	–	–	2.476	**2.465**	2.932	2.893	–	–	2.915	**2.913**
RTC00-3	2.472	–	–	–	2.466	**2.469**	2.927	–	–	–	2.903	**2.915**
RMC00-1	1.667	1.664	–	–	1.669	**1.667**	2.928	2.905	–	–	2.918	**2.917**
RMC00-2	1.672	1.664	–	–	1.676	**1.671**	2.921	2.901	–	–	2.909	**2.910**
RMC00-3	1.658	–	–	1.664	1.655	**1.659**	2.923	–	–	2.898	2.901	**2.900**
RMC45-1	1.642	–	–	1.591	1.615	**1.616**	2.977	–	–	2.962	2.958	**2.966**
RMC45-2	–	–	1.600	1.612	1.633	**1.615**	–	–	2.971	2.965	2.976	**2.971**
RMC45-3	1.656	–	–	1.625	1.634	**1.638**	2.977	–	–	2.966	2.974	**2.972**
RMC90-1	1.696	–	–	1.701	1.705	**1.701**	2.902	–	–	2.813	2.948	**2.954**
RMC90-2	1.694	–	–	1.695	1.702	**1.697**	2.868	–	–	2.801	2.863	**2.841**
RMC90-3	–	–	1.697	1.705	1.712	**1.705**	–	–	2.803	2.827	2.847	**2.826**

A.2 Fibrous

Table A.4: Description of abbreviations and associated tests for the fibrous material

Specimen name	Location	Angle
FTC00	Top	0
FTC45	Top	45
FTC90	Top	90
FMC00	Middle	0
FMC45	Middle	45
FMC90	Middle	90

Table A.5: Pre-mortem measurments of tensile test of the fibrous AA6005A-T6 alloy

Specimen	**ta**	**tb**	**tc**	**td**	**te**	**T**	**wa**	**wb**	**wc**	**wd**	**we**	**W**
FTC00-1	2.572	2.572	2.579	2.577	2.578	**2.576**	3.031	3.038	3.035	3.038	3.037	**3.036**
FTC00-2	2.588	2.587	2.586	2.584	2.586	**2.586**	3.045	3.054	3.044	3.048	3.048	**3.048**
FTC00-3	2.550	2.548	2.549	2.542	2.545	**2.547**	3.036	3.036	3.037	3.039	3.038	**3.037**
FTC45-1	2.525	2.533	2.532	2.537	2.541	**2.534**	3.038	3.035	3.038	3.036	3.034	**3.036**
FTC45-2	2.573	2.570	2.564	2.561	2.546	**2.565**	3.034	3.035	3.035	3.032	3.035	**3.034**
FTC45-3	2.570	2.568	2.570	2.572	2.575	**2.571**	3.042	3.042	3.037	3.036	3.037	**3.039**
FTC90-1	2.571	2.576	2.578	2.578	2.580	**2.577**	3.034	3.036	3.041	3.038	3.042	**3.038**
FTC90-2	2.576	2.577	2.577	2.578	2.585	**2.579**	3.029	3.040	3.040	3.038	3.038	**3.037**
FTC90-3	2.542	2.554	2.559	2.558	2.559	**2.554**	3.034	3.042	3.047	3.040	3.043	**3.041**
FMC00-1	1.770	1.770	1.769	1.768	1.766	**1.769**	3.033	3.036	3.037	3.036	3.036	**3.036**
FMC00-2	1.749	1.752	1.752	1.751	1.752	**1.751**	3.040	3.043	3.037	3.038	3.042	**3.041**
FMC00-3	1.767	1.768	1.767	1.771	1.770	**1.769**	3.028	3.039	3.037	3.039	3.037	**3.036**
FMC45-1	1.734	1.732	1.720	1.714	1.704	**1.721**	3.044	3.043	3.049	3.043	3.042	**3.044**
FMC45-2	1.734	1.731	1.723	1.715	1.701	**1.721**	3.043	3.045	3.037	3.043	3.036	**3.041**
FMC45-3	1.715	1.726	1.741	1.753	1.756	**1.738**	3.048	3.045	3.041	3.038	3.045	**3.043**
FMC90-1	1.755	1.755	1.757	1.741	1.723	**1.746**	3.049	3.050	3.051	3.050	3.051	**3.050**
FMC90-2	1.765	1.758	1.757	1.738	1.726	**1.749**	3.047	3.044	3.052	3.052	3.049	**3.049**
FMC90-3	1.759	1.756	1.757	1.745	1.725	**1.748**	3.046	3.041	3.045	3.050	3.044	**3.045**

Table A.6: Post-mortem measurments of tensile test of the fibrous AA6005A-T6 alloy

Specimen	**ta**	**tb**	**tc**	**td**	**te**	**T**	**wa**	**wb**	**wc**	**wd**	**we**	**W**
FTC00-1	2.490	2.468	-	-	-	**2.479**	2.993	2.987	-	-	-	**2.990**
FTC00-2	2.446	2.428	-	-	-	**2.447**	2.981	2.959	-	-	-	**2.965**
FTC00-3	-	-	-	2.434	2.442	**2.438**	-	-	-	2.975	2.973	**2.974**
FTC45-1	-	-	-	2.435	2.456	**2.446**	-	-	-	2.969	2.980	**2.975**
FTC45-2	-	-	-	2.415	2.459	**2.437**	-	-	-	2.917	2.936	**2.927**
FTC45-3	-	-	-	2.453	2.495	**2.474**	-	-	-	2.949	2.967	**2.958**
FTC90-1	2.518	2.503	-	-	-	**2.511**	2.955	2.932	-	-	-	**2.944**
FTC90-2	2.513	2.503	-	-	-	**2.508**	2.928	2.907	-	-	-	**2.918**
FTC90-3	-	-	-	2.470	2.491	**2.481**	-	-	-	2.883	2.924	**2.904**
FMC00-1	1.703	1.726	1.708	-	-	**1.712**	3.003	2.986	2.997	-	-	**2.995**
FMC00-2	1.685	1.694	1.681	-	-	**1.687**	2.997	2.996	2.991	-	-	**2.995**
FMC00-3	-	-	1.689	1.700	1.694	**1.694**	-	-	2.988	2.981	2.972	**2.980**
FMC45-1	1.710	1.698	1.668	-	-	**1.692**	3.036	3.038	3.034	-	-	**3.036**
FMC45-2	1.709	1.690	1.693	-	-	**1.697**	3.045	3.042	3.045	-	-	**3.044**
FMC45-3	1.640	-	-	1.682	1.714	**1.679**	3.031	-	-	3.037	3.034	**3.034**
FMC90-1	1.731	1.718	1.720	-	-	**1.723**	2.988	2.975	2.977	-	-	**2.980**
FMC90-2	1.743	1.732	1.730	-	-	**1.735**	2.989	2.973	2.965	-	-	**2.976**
FMC90-3	1.733	1.721	1.711	-	-	**1.728**	2.991	2.968	2.957	-	-	**2.972**

B Appendix - Stress - Strain Curves

In Appendix B, the engineering stress-strain curves of both the alloy with recrystallised- and fibrous microstructure are presented.

B.1 Recrystallised

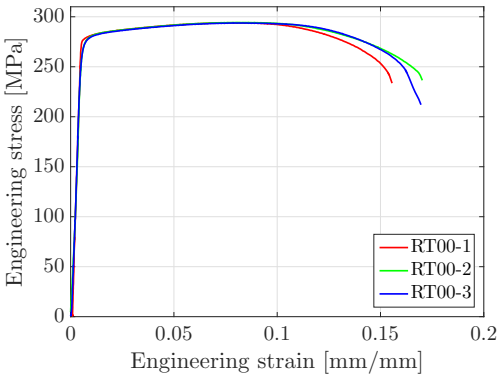

(a) Top wall, base, at 0°

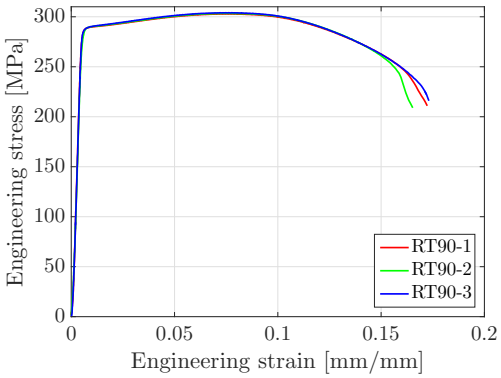

(b) Top wall, base, at 90°

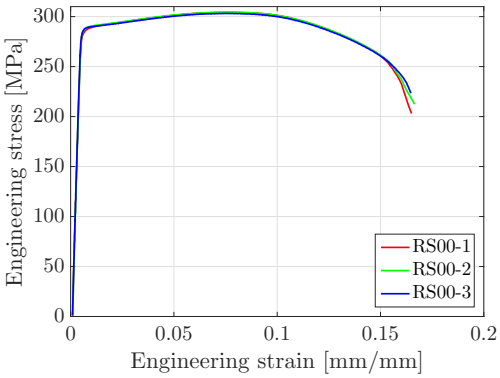

(c) Side wall, base, at 0°

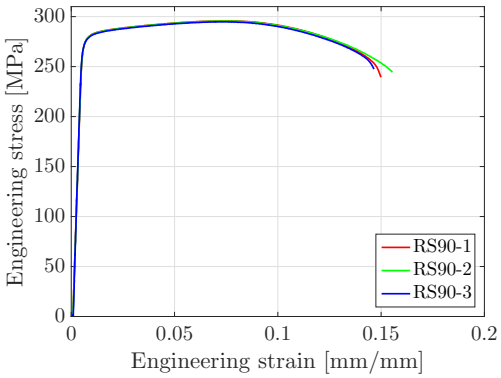

(d) Side wall, base, at 90°

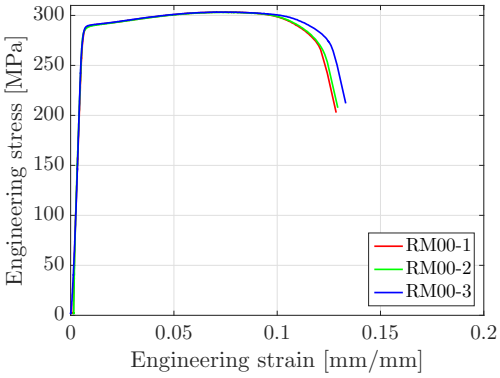

(e) Middle wall, base, at 0°

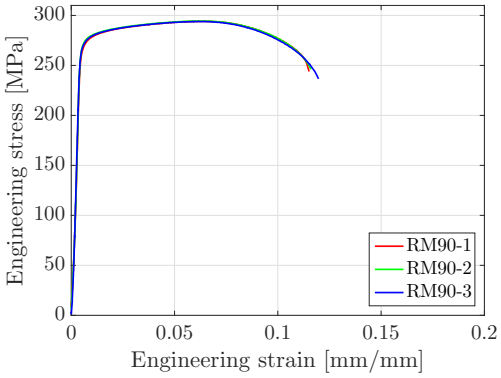

(f) Middle wall, base, at 90°

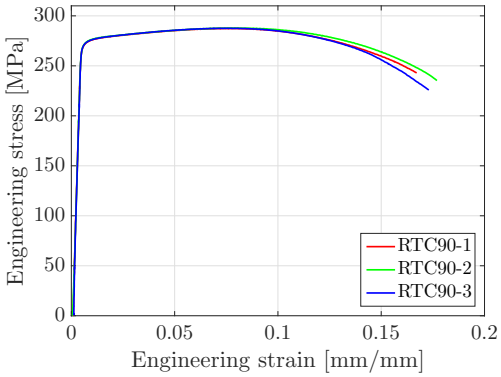

(g) Top wall, near centre, at 90°

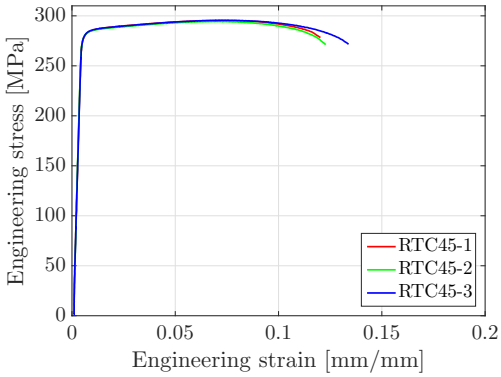

(h) Top wall, near centre, at 45°

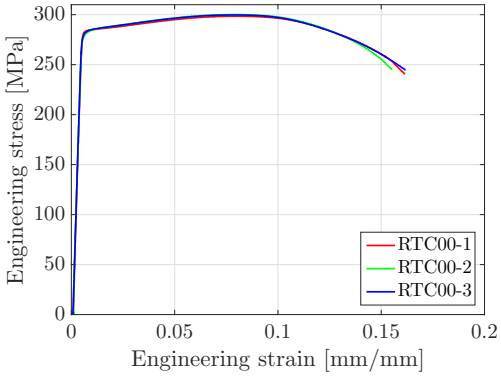

(i) Top wall, near centre, at 0°

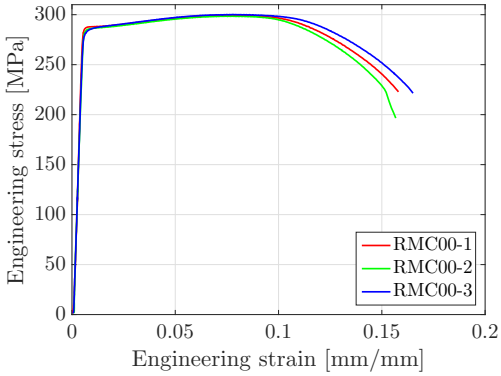

(j) Middle wall, near centre, at 0°

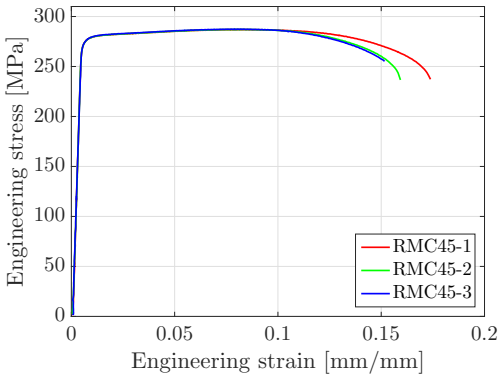

(k) Middle wall, near centre, at 45°

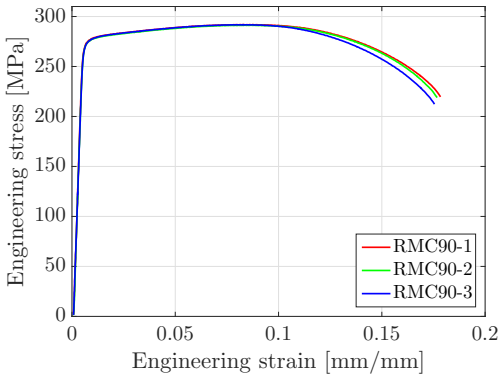

(l) Middle wall, near centre, at 90°

B.2 Fibrous

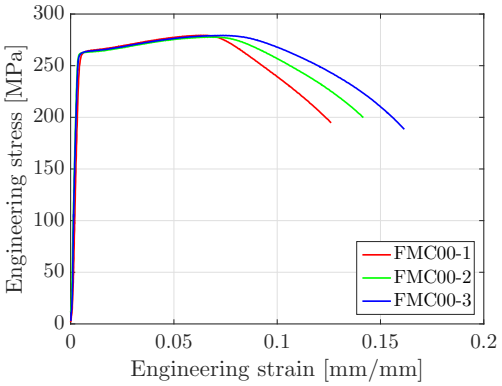

(a) Middle wall at 0°

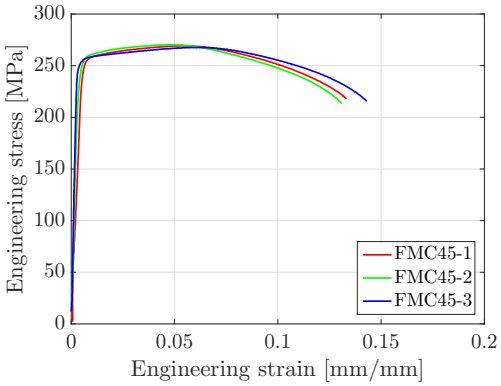

(b) Middle wall at 45°

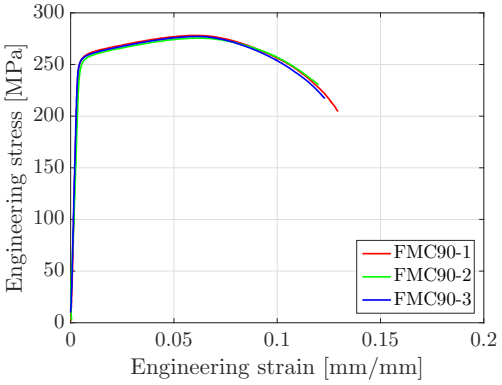

(c) Middle wall at 90°

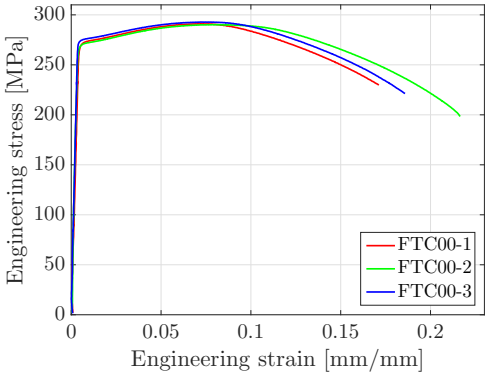

(d) Outer wall at 0°

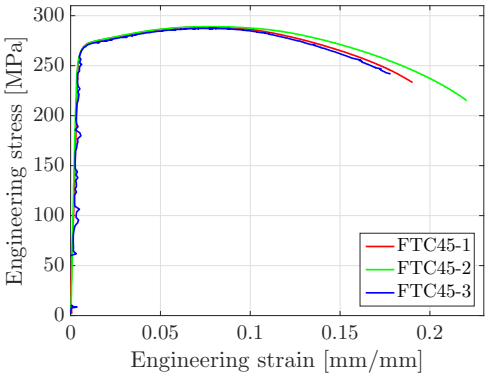

(e) Outer wall at 45°

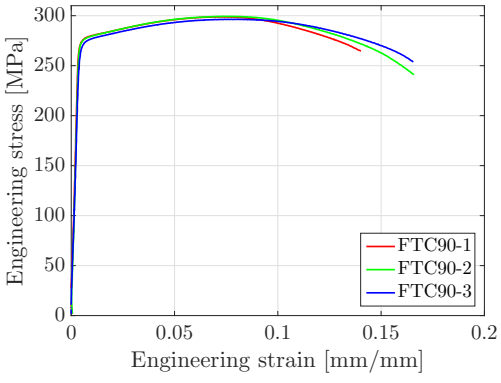

(f) Outer wall at 90°

B.3 R-value

Table B.1: R-values for recrystallised alloy of middle- and top wall

Middle wall			Outer wall		
0°	45°	90°	0°	45°	90°
0.554	0.111	2.134	0.578	0.159	2.386

Table B.2: R-values for fibrous alloy of middle- and top wall

Middle wall			Outer wall		
0°	45°	90°	0°	45°	90°
0.422	0.058	2.130	0.465	0.667	1.406

C Appendix - Material Card

C.1 Recrystallized Microstructure

```
*Material, Name = SMM_AA6005T6_OUTER
*Include, input = DEPVAR_SMM.inc
*Density
2.71e-09,
*User material, Constants = 30
**       EFLAG,          YFLAG,          RMAPFLAG,       HFLAG,          VFLAG,
             1,              3,              5,              1,              0,
**       TFLAG,          DFLAG,          SFFLAG          STFLAG,         E0,
             0,              4,              0,              0           6.48842e+04,
**       NU,             SIGMA0,         A,              KSI,            THETA0R1,
          0.33,          2.75681e+02,    8.00000e+00,    1.00000e-01,    7095.1
**       Q0R1            THETA0R2,       Q0R2,           THETA0R3,       Q0R3,
       8.61260e+00       702.334,        48.4693,        166.246,        12.1634
**       THETAMIN,       DINIT,          DCRIT,          WCB             WCS,
       0.00000e+00,    0.00000e+00,    1.0,            170.50          69.1112,
**       WCL,            c,              PHI,            GAMMA,          THICK,
          3.6388,         0.2188,         1.0,            1.0,            2.5653
*Material, Name = SMM_AA6005T6_INNER
*Include, input = DEPVAR_SMM.inc
*Density
2.71e-09,
*User material, Constants = 30
**       EFLAG,          YFLAG,          RMAPFLAG,       HFLAG,          VFLAG,
             1,              3,              5,              1,              0,
**       TFLAG,          DFLAG,          SFFLAG          STFLAG,         E0,
             0,              4,              0,              0           6.48842e+04,
**       NU,             SIGMA0,         A,              KSI,            THETA0R1,
          0.33,          2.75681e+02,    8.00000e+00,    1.00000e-01,    7095.1
**       Q0R1            THETA0R2,       Q0R2,           THETA0R3,       Q0R3,
       8.61260e+00       702.334,        48.4693,        166.246,        12.1634
**       THETAMIN,       DINIT,          DCRIT,          WCB             WCS,
       0.00000e+00,    0.00000e+00,    1.0,            170.50          69.1112,
**       WCL,            c,              PHI,            GAMMA,          THICK,
          3.6388,         0.2188,         1.0,            1.0,            1.7460
```

C.2 Fibrous Microstructure

*Material, Name = SMM_AA6005T6_OUTER
*Include, input = DEPVAR_SMM.inc
*Density
2.71e-09,
*User material, Constants = 30

**	EFLAG,	YFLAG,	RMAPFLAG,	HFLAG,	VFLAG,
	1,	3,	5,	1,	0,
**	TFLAG,	DFLAG,	SFFLAG	STFLAG,	E0,
	0,	4,	0,	0	77867.71,
**	NU,	SIGMA0,	A,	KSI,	THETA0R1,
	0.33,	272.3,	8.00000e+00,	1.00000e-02,	5823.9
**	Q0R1	THETA0R2,	Q0R2,	THETA0R3,	Q0R3,
	2.2	596.4,	34.22,	281.7,	30.67
**	THETAMIN,	DINIT,	DCRIT,	WCB	WCS,
	0.00000e+00,	0.00000e+00,	1.0,	168.67	121.124,
**	WCL,	c,	PHI,	GAMMA,	THICK,
	44.7038,	0.8599,	1.0,	1.0,	2.5653

*Material, Name = SMM_AA6005T6_INNER
*Include, input = DEPVAR_SMM.inc
*Density
2.71e-09,
*User material, Constants = 30

**	EFLAG,	YFLAG,	RMAPFLAG,	HFLAG,	VFLAG,
	1,	3,	5,	1,	0,
**	TFLAG,	DFLAG,	SFFLAG	STFLAG,	E0,
	0,	4,	0,	0	77867.71,
**	NU,	SIGMA0,	A,	KSI,	THETA0R1,
	0.33,	272.3,	8.00000e+00,	1.00000e-02,	5823.9
**	Q0R1	THETA0R2,	Q0R2,	THETA0R3,	Q0R3,
	2.2	596.4,	34.22,	281.7,	30.67
**	THETAMIN,	DINIT,	DCRIT,	WCB	WCS,
	0.00000e+00,	0.00000e+00,	1.0,	168.67	121.124,
**	WCL,	c,	PHI,	GAMMA,	THICK,
	44.7038,	0.8599,	1.0,	1.0,	1.7460

D Appendix - Bolt Design Calculations

In this appendix the calculation of the strength of the bolts and the profile with regard to designing the specimen is done.

D.1 Only Pre-made Holes

Firstly the capacity of the grip section with only the pre-made holes was calculated.

D.1.1 Shear Resistance per Shear Plane

$$F_{v,Rd} = \frac{\alpha_v f_{ub} A}{\gamma_{M2}} \tag{D.1}$$

$\alpha_v = 0.6$

$f_{ub} = 830MPa$: ultimate strength of the bolts material

$A = \frac{\pi 20^2}{4} = 314.16mm^2$: tensile stress area of the bolt

$\gamma_{M2} = 1.25$: safety factor regard to resistance of cross-sections in tension to fracture

$$F_{v,Rd} = \frac{0.6 * 830 * \frac{\pi 20^2}{4}}{1.25} = 125.16kN \tag{D.2}$$

Two bolts:

$$F_{v,Rd} = 125.16kN * 2 = 250.32kN \tag{D.3}$$

D.1.2 Bearing Resistance

$$F_{b,Rd} = \frac{\alpha_b k_1 dt f_u}{\gamma_{M2}} \tag{D.4}$$

α_b is the smallest of α_d, $\frac{f_{ub}}{f_u}$ or 1

α_d are $\frac{e_1}{3d_0}$ for edge holes and $\frac{p_1}{3d_0} - \frac{1}{4}$ for inner bolts in the loading direction, see Figure D.1

k_1 is the smallest of $2.8\frac{e_2}{d_0} - 1.7$ or 2.5 for edge holes and $1.4\frac{p_2}{d_0} - 1.7$ or 2.5 perpendicular to the loading direction, see Figure D.1

$f_u = 273.3MPa$: ultimate strength of the profiles material

$f_{ub} = 830MPa$: ultimate strength of the bolts material

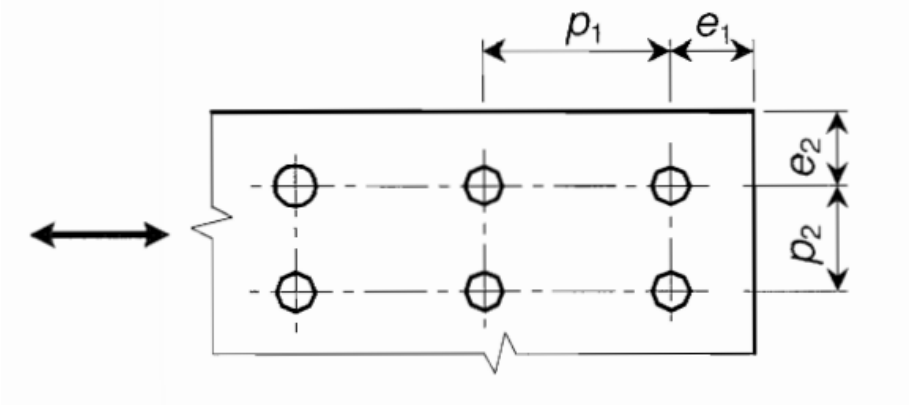

Figure D.1: Definition of edge and pitch distance [6]

$d = 20mm$: bolt diameter

$d_0 = 22mm$: hole diameter

$t = 2.56mm$: profile thickness

$e_1 = 75mm, e_2 = 70mm, p_1 = 100mm, p_2 = 0$, see Figure D.1

$\gamma_{M2} = 1.25$: safety factor regard to resistance of cross-sections in tension to fracture

$$\alpha_d = \frac{830}{272.3} = 3.05 \vee 1 \vee \frac{75}{3 * 22} = 1.14 \vee \frac{100}{3 * 22} - \frac{1}{4} = 1.26 \tag{D.5}$$

$$\alpha_d = 1 \tag{D.6}$$

$$k_1 = 2.8 * \frac{70}{22} - 1.7 = 7.20 \vee 2.5 \tag{D.7}$$

$$k_1 = 2.5 \tag{D.8}$$

$$F_{b,Rd} = \frac{2.5 * 1 * 20 * 2.56 * 272.3}{1.25} = 27.88kN \tag{D.9}$$

Two bolts:

$$F_{v,Rd} = 27.88kN * 2 = 55.77kN \tag{D.10}$$

D.1.3 Tension Resistance

$$F_{t,Rd} = \frac{k_2 f_{ub} A}{\gamma_{M2}} \tag{D.11}$$

$k_2 = 0.9$: for steel bolts

$f_{ub} = 830MPa$: ultimate strength of the bolts material

$A = \frac{\pi 20^2}{4} = 314.16mm^2$: tensile stress area of the bolt

$\gamma_{M2} = 1.25$: safety factor regard to resistance of cross-sections in tension to fracture

$$F_{t,Rd} = \frac{0.9 * 830 * \frac{\pi 20^2}{4}}{1.25} = 187.74kN \tag{D.12}$$

Two bolts:

$$F_{t,Rd} = 187.74kN * 2 = 375.48kN \tag{D.13}$$

D.2 Final Bolt Design

The capacity of the grip section with the final bolt design was then calculated. The design consists of two different bolt sizes, hence the contribution from both is calculated and then added.

D.2.1 Shear Resistance per Shear Plane

Strength from the M20 bolts:

$$F_{v,Rd} = \frac{\alpha_v f_{ub} A}{\gamma_{M2}} \tag{D.14}$$

$$F_{v,Rd} = \frac{0.6 * 830 * \frac{\pi 20^2}{4}}{1.25} = 125.16kN \tag{D.15}$$

Three M20 bolts:

$$F_{v,Rd} = 125.16kN * 3 = 375.48kN \tag{D.16}$$

Strength from the M10 bolts:

$$F_{v,Rd} = \frac{\alpha_v f_{ub} A}{\gamma_{M2}} \tag{D.17}$$

$$F_{v,Rd} = \frac{0.6 * 830 * \frac{\pi 10^2}{4}}{1.25} = 31.29kN \tag{D.18}$$

Eight M10 bolts:

$$F_{v,Rd} = 31.29kN * 8 = 250.32kN \tag{D.19}$$

Sum shear resistance: 375.48kN + 250.32kN = 625.80kN

D.2.2 Bearing Resistance

$$F_{b,Rd} = \frac{\alpha_b k_1 dt f_u}{\gamma_{M2}} \tag{D.20}$$

α_b and k_1 is defined as in the previous calculation.

Strength from the M20 bolts:

$d = 20mm$: bolt diameter

$d_0 = 22mm$: hole diameter

$e_1 = 75mm, e_2 = 70mm, p_1 = 50mm, p_2 = 32mm$

$$\alpha_d = \frac{830}{272.3} = 3.05 \vee 1 \vee \frac{75}{3 * 22} = 1.14 \vee \frac{50}{3 * 22} - \frac{1}{4} = 0.51 \tag{D.21}$$

$$\alpha_d = 0.51 \tag{D.22}$$

$$k_1 = 2.8 * \frac{70}{22} - 1.7 = 7.20 \vee 2.5 \vee 1.4\frac{32}{22} - 1.7 = 0.34 \tag{D.23}$$

$$k_1 = 0.34 \tag{D.24}$$

$$F_{b,Rd} = \frac{0.34 * 0.51 * 20 * 2.56 * 272.3}{1.25} = 1.93kN \tag{D.25}$$

Three bolts:

$$F_{b,Rd} = 27.88kN * 2 = 5.80kN \tag{D.26}$$

Strength from the M10 bolts:

$d = 10mm$: bolt diameter

$d_0 = 12mm$: hole diameter

$e_1 = 50mm, e_2 = 50mm, p_1 = 50mm, p_2 = 32mm$

$$\alpha_d = \frac{830}{272.3} = 3.05 \vee 1 \vee \frac{50}{3 * 12} = 1.38 \vee \frac{50}{3 * 12} - \frac{1}{4} = 1.14 \tag{D.27}$$

$$\alpha_d = 1.14 \tag{D.28}$$

$$k_1 = 2.8 * \frac{50}{12} - 1.7 = 6.63 \vee 2.5 \vee 1.4\frac{32}{12} - 1.7 = 2.03 \tag{D.29}$$

$$k_1 = 2.03 \tag{D.30}$$

$$F_{b,Rd} = \frac{2.03 * 1.14 * 10 * 2.56 * 272.3}{1.25} = 12.91kN \tag{D.31}$$

Eight bolts:

$$F_{b,Rd} = 12.91kN * 8 = 103.28kN \tag{D.32}$$

Sum bearing resistance: 5.80kN + 103.28kN = 109.08kN

D.2.3 Tension Resistance

$$F_{t,Rd} = \frac{k_2 f_{ub} A}{\gamma_{M2}} \tag{D.33}$$

Strength from M20 bolts:

$$F_{t,Rd} = \frac{0.9 * 830 * \frac{\pi 20^2}{4}}{1.25} = 187.74kN \tag{D.34}$$

Three bolts:

$$F_{t,Rd} = 187.74kN * 3 = 563.22kN \tag{D.35}$$

Strength from M10 bolts:

$$F_{t,Rd} = \frac{0.9 * 830 * \frac{\pi 10^2}{4}}{1.25} = 46.94kN \tag{D.36}$$

Eigth bolts:

$$F_{t,Rd} = 187.74kN * 8 = 375.48kN \tag{D.37}$$

Sum tension resistance: 563.22kN + 375.48kN = 938.70kN

E Appendix - Stretch Bending Rig

This appendix provide some detailed dimensions of the stretch bending rig.

E.1 Horizontal Actuator

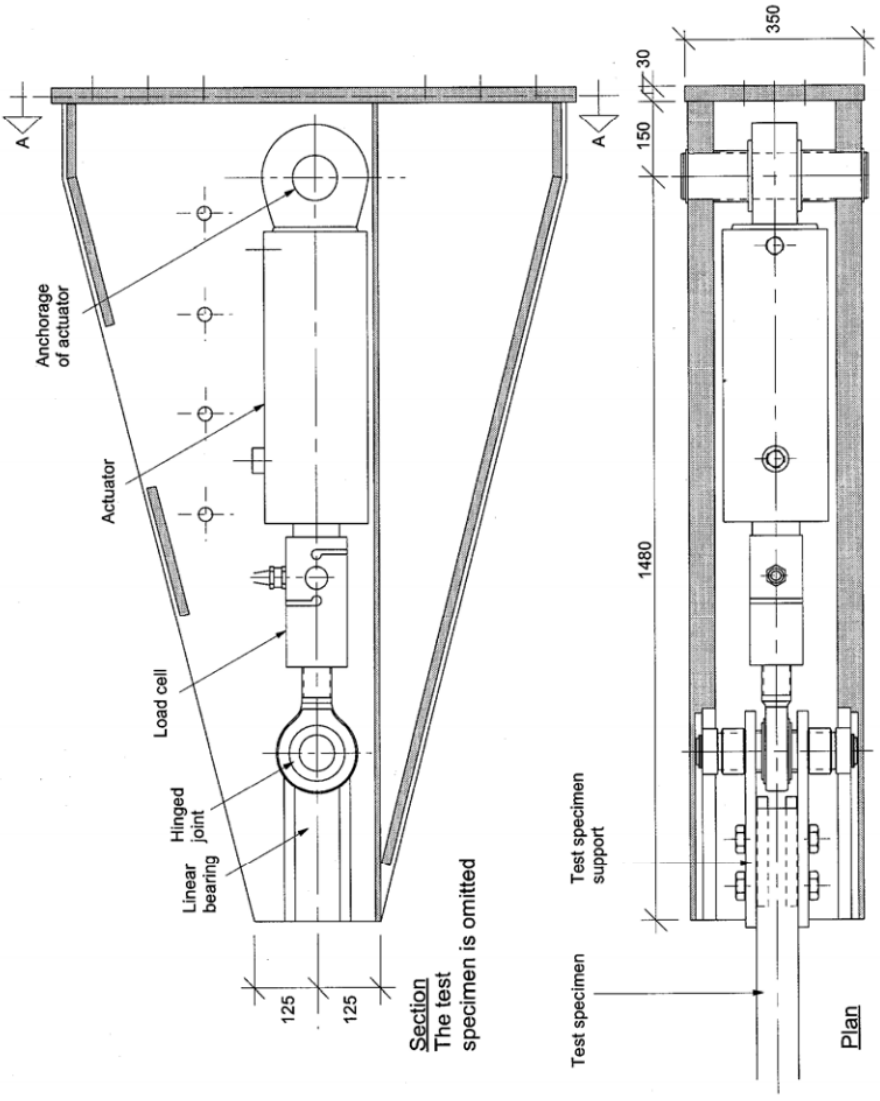

Figure E.1: Horizontal actuator mount [5]

E.2 Vertical Actuator

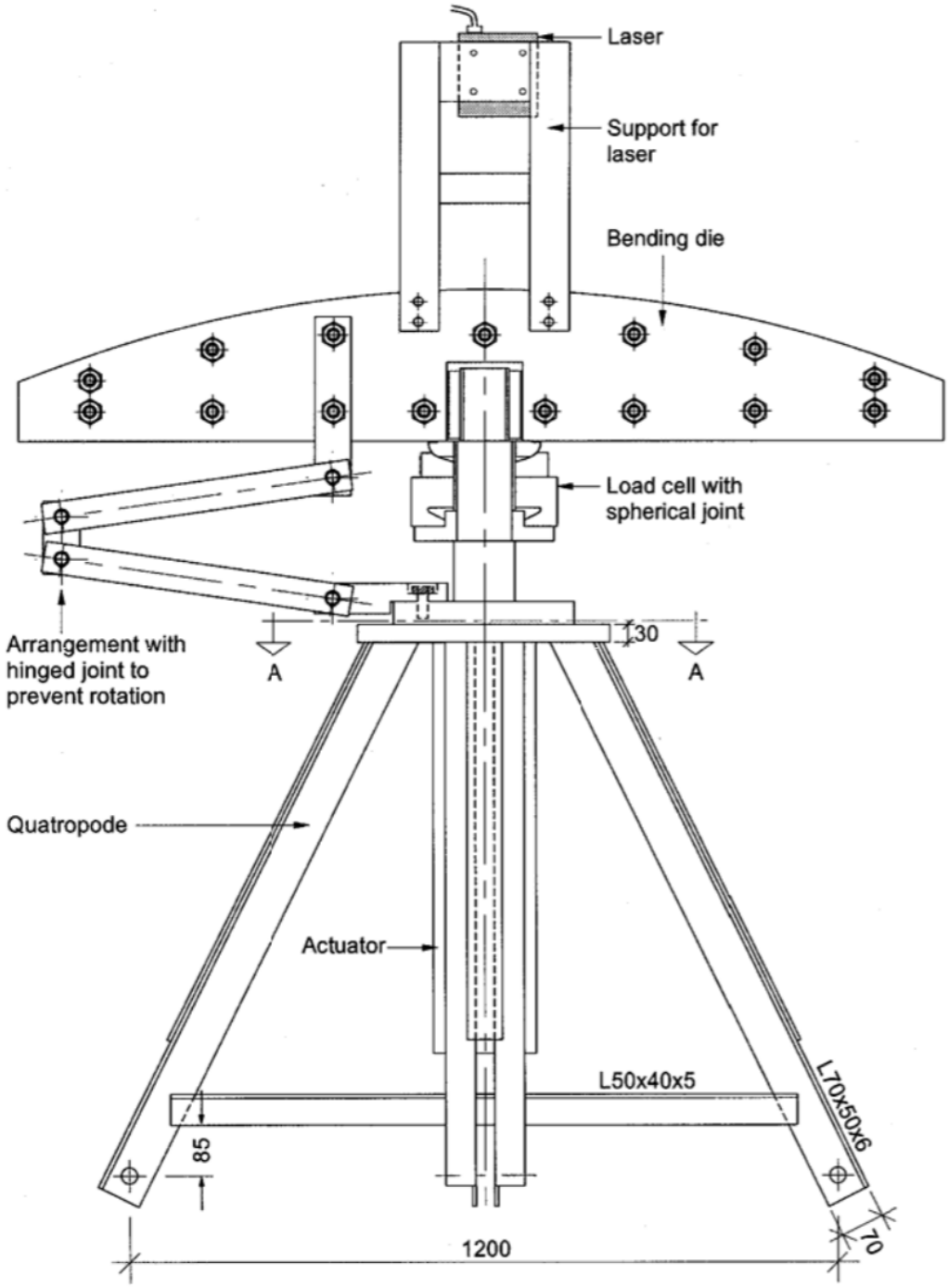

Figure E.2: Vertical actuator die mount [5]